Distribution Agreement

In presenting this thesis or dissertation as a partial fulfillment of the requirements for an advanced degree from Emory University, I hereby grant to Emory University and its agents the non-exclusive license to archive, make accessible, and display my thesis or dissertation in whole or in part in all forms of media, now or hereafter known, including display on the world wide web. I understand that I may select some access restrictions as part of the online submission of this thesis or dissertation. I retain all ownership rights to the copyright of the thesis or dissertation. I also retain the right to use in future works (such as articles or books) all or part of this thesis or dissertation.

Signature:

_____ _____

Dandan Chen Date

Investigation of Shear Induced Relaxation in Soft Materials

By

Dandan Chen

Doctor of Philosophy in Physics

Signature_____
Advisor: Eric R. Weeks

Signature_____
Committee Member: Kurt Warncke

Signature_____
Committee Member: Stefan Boettcher

Signature_____
Committee Member: Connie Roth

Signature_____
Committee Member: Shun Yan Cheung

Signature_____
Committee Member: Andrew Lyon

Accepted:

_____
Lisa A. Tedesco, Ph.D.
Dean of the James T. Laney School of Graduate Studies

_____
Date

Investigation of Shear Induced Relaxation in Soft Materials

By

Dandan Chen
B.Sc., Nanjing University, Nanjing, China, 2003

Advisor: Eric R. Weeks, Ph.D.

An abstract of
A dissertation submitted to the Faulty of the
James T. Laney School of Graduate Studies of Emory University
in partial fulfillment of the requirements for the degrees of
Doctor of Philosophy
in Physics

Fall, 2010

Abstract

Investigation of Shear Induced Relaxation in Soft Materials
By Dandan Chen

The study of how soft materials response to shear is important for food industry and drug delivery. However, the basic questions are still unsolved, due to the difficulty of seeing inside samples as they are sheared. Here we study plastic changes of soft materials by using advanced microscopes and particle-tracking techniques. From the simple systems like colloids (solid particles in a liquid) and emulsions (oil droplets in water), we try to understand the two primary phenomena of shear-induced "plasticity" in soft materials: micro-dynamics and stress fluctuations.

In my colloidal experiment, I focus on the micro-dynamics of colloidal particles under large shear strain. By using fast confocal microscopy, we can observe and track colloids in a 3D movie. From their trajectories we quantify the plastic rearrangements of the particles in several ways. Each of these measures of plasticity reveals spatially heterogeneous dynamics, with localized regions where many particles are strongly rearranging by these measures. We examine the shapes of these regions and find them to be essentially isotropic, with no alignment in any particular direction. Furthermore, individual particles are equally likely to move in any direction, other than the overall bias imposed by the strain.

In my emulsion experiment, I go further to study the connection between macroscopic stresses and microscopic dynamics. We use the 2D emulsion disks to study the plastic changes of dense materials passing through a hopper channel. We find that under different flux rates, the flow profiles in the hopper are very similar. To quantify the plastic rearrangements, we focus on specific neighbor rearrangements called "T1 events". In addition, from the deformed shapes of droplets, we quantify the interactions between droplets. We find large temporal fluctuation of stresses in a large scale. From the micro-dynamics, we find the temporal changes of stresses are directly related to the T1 rearrangements. Our analysis of this emulsion system shows a direct and local relationship between rearrangements and stress fluctuations.

Investigation of Shear Induced Relaxation in Soft Materials

By

Dandan Chen
B.Sc., Nanjing University, Nanjing, China, 2003

Advisor: Eric R. Weeks, Ph.D.

A dissertation submitted to the Faulty of the
James T. Laney School of Graduate Studies of Emory University
in partial fulfillment of the requirements for the degrees of
Doctor of Philosophy
in Physics

Fall, 2010

Acknowledgments

"I was determined to study when I was 15; *I became independent in the world by 30*; by 40 I kept a clear mind in various situations; by 50 I understood what fate is; by 60 I could listen to various opinions; by 70 I could follow the desire of my heart without wrong doing."
---- Confucius

First and foremost, I wish to thank **Prof. Eric R. Weeks**, my Ph.D. adviser for guiding me in the research over the past years. He also encourages me to go out of lab to speak out my work, either during the APS March meeting in US or during the CPS autumn meeting in China. And he has been very supportive since I decided to pursue my academic career back in China. I would also like to thank my dissertation committee: **Prof. Kurt Warncke**, **Prof. Connie Roth**, **Prof. Stefan Boettcher**, **Prof. Shun Yan Cheung**, **and Prof. Andrew Lyon**. The annual meetings always make sure I am in the right track to the graduation. And their questions urge me to give a deeper thought on my projects from different perspectives.

And I would also like to take a chance to thank **Prof. Fereydoon Family** and **Prof. George Hentschel** for letting me join in their physics of cancer research. It is a very good opportunity for me to enter the interdisciplinary area between biology and soft materials. In both of my projects, I have got technique supports from Georgia Tech. I would like to thank **Prof. Victor Breedveld**, and his student **Jun Sato** for shear cell. Thank **Prof. Alberto Fernandez-Nieves** for the co-flowing emulsion technique. Thank **Prof. Hang Lu** and her student **Jan Krajniak** for the help on microchips.

I would like to give thanks to all the members in Weeks' lab: **Gianguido Cianci, Joaquim Clara-Rahola, Ken Desmond, Kazem Edmond, Gary Hunter, Kelsey Hattam, Xia Hong, Rei Kurita, David Kilgore, Paul Martin, Vikram Prasad, Daniel Real, Denis Semwogerere, Nabiha Saklayen, James Sebel, Gopal Subedi, Pearl Young**. I would also like to thank all the YEPs here, young Emory physicists for many parties, barbecues, and football games. And to the **Department of Physics at Emory**, I really appreciate its great environment and all the supports on learning and research over the past years.

Last but not least, I would like to thank my family for all their love which is the source of my energy. Dad and Mom, as your only child, your healthy is the best blessing to me. And Yongkang, my love and soulmate, no more word need here. Thanks for all the love, patient, and understanding.

Contents

List of Figures

Chapter 1

Introduction

1.1 Soft material

Soft materials, or soft condensed matter, is a general term for the materials which are neither simply liquid nor crystalline solid [1]. Such materials are common in daily life, including colloids, emulsions, foams, gels, and grains. Colloids are microscopic solid particles in a liquid, such as toothpaste, paint, and ink. Due to the small size, Brownian motion or thermal fluctuation is one of the characteristics of colloidal suspension. Emulsions are liquid droplets dispersed in another immiscible liquid, such as milk and mayonnaise. Foams are air bubbles in a liquid, such as shaving cream. Gels, such as gelatin, are solid-like materials but with low concentration of particles. Due to the strong attraction, particles are able to bond with each other and build up a macroscopic network. Grains, or granular materials, are solid particles in air with size larger than millimeter. Due to the large size, thermal fluctuation is neglected. Plus, friction is another important character for granular systems.

1.2 Jamming

One common feature to all soft materials is they have liquid-like disordered micro structure but can maintain their shapes acting like solids. And the transition from a random liquid state to a random solid jammed state is called jamming transition. For example, when a hot liquid glass is cooled, it becomes more and more viscous and finally become a strong solid, maintaining the disordered micro structure. This jamming process is also named as glass transition. The idea that a common jamming transition may happen in different soft materials leads to a deeper understanding, even if many details remain quite different [2]. For example, in granular materials it is believed that friction is critically important for jamming. But in recent experiments, it is found that jamming could also happen in smooth grains with little friction [3]. Besides, jamming also exists in densely packed soft droplets without static friction (emulsion) [4]. Therefore, many experiments are designed to investigate those common properties of jamming by comparing different soft materials.

Fig. 1.1 shows an phase diagram of jammimg, covering different soft materials like glass, bubbles, droplets, and grains. By controlling the parameters like temperature, concentration, and stress, we can control the state of those materials from solid-like jamming to liquid-like unjamming, or other way around. For example, hot silicon glass in forge is like a liquid without a fixed shape. By cooling down it would be more and more viscous and finally become a solid with a fixed shape. The temperature here can be used as a more general concept "kinetic energy", rather than just thermal energy. For granular materials, the kinetic energy could be induced by vibration [5], although thermal fluctuation is trivial. And people are trying to generate the effective "temperature" from this driven system [6], and unify the jamming concept. Besides temperature, increasing concentration or pressure can also lower kinetic energy of particles by increasing the chance of collision between neighbors. In colloidal suspension (Section 2.1), concentration is an important control parameter which determines

the material's states (Section 2.1.2).

In addition, stress is also an important factor. This relates to an important characteristic of soft materials, called viscoplastic. The material behaves as a rigid (jammed) solid under small stress or strain, but start to flow as a viscous (unjammed) liquid under large stress or strain. A common example is toothpaste, which is a kind of colloid. When we squeeze the tube, large shear strain and stress is applied, and toothpaste is forced to flow out. But once out the tube, the toothpaste is no longer under shear, and then keeps a solid plug shape. The micro mechanic reason for this viscoplastic property is that particles are densely packed in the jammed material, and their motions are confined by close neighbors around. This packing structure could resist small strain or stress, and the small deformation is reversible if strain is reversed. But under large stress or strain, particles are forced to move over long distances. And they have to collide with their neighbors, which leads to plastic rearrangement [7, 8, 9]. This deformation is irreversible even if the strain is applied backward, and this is called plastic deformation in the yield flow. People found in macro scale, the yield flow has nonlinear mechanic behavior. Due to the limit of microscopic technique, one is not sure how the plastic deformation happening in the micro scale. So we use simple geometries to study the microscopic structure changes under shear, which is what my projects focus on.

The meaning of this phase diagram is suggesting a way to investigate jamming. For different systems, control parameters of jamming are usually different. For example, temperature is neglect-able to large-size grains, but important for small size colloids with Brownian motion. Sometime, without changing temperature, people could increase the concentration of dense liquid to prohibit the thermal fluctuation, by increasing the collision chance between neighbors. And in this way, one could mimic the low temperature behavior of glassy liquid with slower Brownian motion at room temperature. Therefore, by comparing different jammed systems or different

control parameters, people could a deeper understanding of jamming. For instance, what is the similarity or difference between the thermal origin jamming (silicon glass), entropic origin jamming (colloids), and kinetic origin jamming (athermal systems like grain, emulsion, and foam) ? Or how does the temperature of glass transition changes under different stresses? Or how does the vibration affect the yield stress in jammed granular materials ? Or how important friction is in jamming by comparing frictional granular systems with frictionless ones (foam or emulsion) ? Although some of the questions still require further investigation, the benefit of this diagram suggests future experiments for better understanding of jammed materials [10].

1.3 Spatially heterogeneous dynamics

Spatially heterogeneous dynamics is an important feature of materials during jamming transition [10]. During the transition, the micro structure of soft materials remains liquid-like disorder, but particle dynamics inside decrease dramatically, leading to a rapid increase of viscosity. To understand this phenomena, many theories try to give a picture of microscopic mechanics. And Adam and Gibbs [11] are among the first theorists who propose the concept of "cooperative dynamics". It suggests that in dense liquid particles have limit free space to move around, caged by neighbors in most of the time. To diffuse in a longer distance, a particle has to wait for neighbors moving first and sparing more space around. In this way, neighboring particles would like to move together or cooperatively. And the relaxation time depends on the "waiting time" for this cooperation. For denser suspension with less free space, more particles are needed for the cooperation, and longer "waiting time" would be. Therefore, viscosity of dense liquid is quite sensitive even to a slight change in the concentration.

The cooperative dynamics are first seen in computer simulations [12], and later found in colloidal experiments [13, 14]. In Fig. 1.2, some particles are moving very

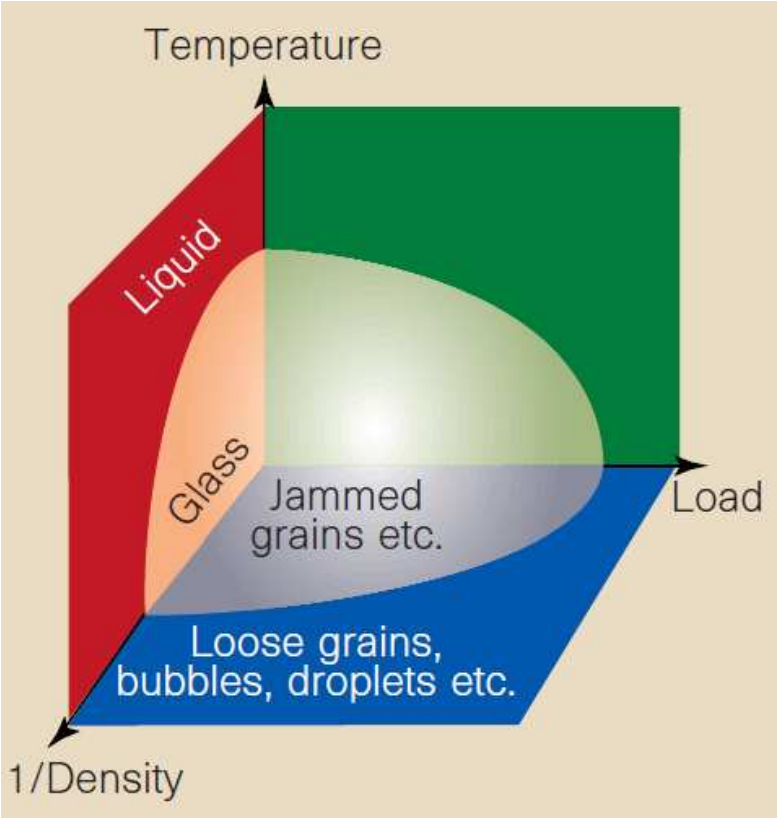

Figure 1.1: (Color online) Jamming phase diagram from [2]. The three axes are temperature, density, and load. It shows that the jamming could be reached by lowering temperature (slowing down Brownian motion), increasing density, and decreasing forces. For example, by decreasing temperature, silicon glass would be more and more viscous and finally become a jammed solid. And by increasing concentration of colloidal suspensions, particles' Brownian motion would be prohibited by their neighbors crowding around, then are caged or jammed in local regions. The boundary of the phase diagram indicates the transition from jam to unjam states, or other way around. For instance, by applying stress over a yielding point, the original structure could no longer maintain the shape, and the material starts to flow.

fast (drawn in a larger size), while others are only moving in a short distance during the same time (drawn smaller). And these mobile ones are close to each other forming rearranging clusters or regions (colored in blue and red in the graph). As the graph shows, the micro dynamics are not uniformly distributed, but concentrate in some small regions. This dynamic distribution is an typical example for spatially heterogeneous dynamics in jammed materials. Besides colloidal system, there are a large amount of recent evidences for spatially heterogeneous motions in molecular materials near the glass transition [15].

In my colloid experiment, I also observed the cooperative rearrangements during the shear driven relaxation (Chapter 4). Additionally, cooperative rearrangements are also found in other jammed materials, although the dynamic details might appear different. In sheared foam and emulsion, a typical form of rearrangements is called T1 event [16, 17] , which involves four particles exchanging positions: two move apart, two move together [18]. In my emulsion experiment (Chapter 7), I study how those micro T1 rearrangements lead to the stress relaxation of dense flow in a macro scale.

1.4 Force chains in jammed systems

Since the jammed material can support small stress or shear, it is believed that the stress on a surface could propagate through the bulk to another side of the material. The propagation of force is investigated in granular materials. One can see stress distribution by using 2 dimensional photoelastic disks [19], as shown in Fig. 1.3(a). The photoelastic disk can change polarization under stress, and polarized light passing through would be rotated. Thus stresses can be visualized by placing the disks between two crossed circular polarizers. From the stress pattern of bright and dark bands on each disk, Behringer lab developed a technique measuring both normal contact forces and tangential friction [19]. The brightness in the graph shows anisotropy

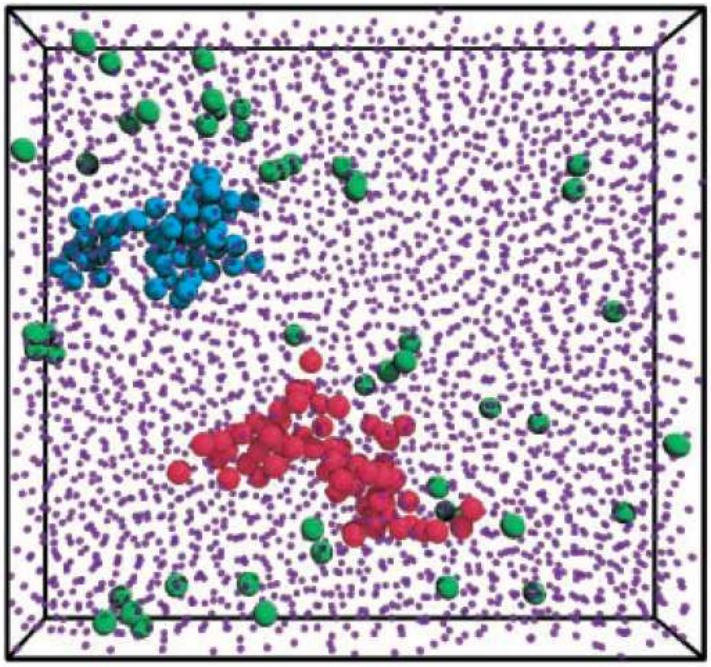

Figure 1.2: (Color online) Fast moving particles cluster together in a dense colloidal suspension from [13]. In this graph, all particles have same physical sizes (1.18 μm in radius). But for clarity, only those fast moving particles are drawn with the real size, and the others are drawn smaller. The volume fraction of the colloidal suspension is ϕ=0.56 (see Section 2.1.2). And the particles' moving distances are measured over Δt=1000s. The blue and the red colors label two large mobile clusters, containing 50 and 69 mobile particles. These large clusters of dynamic particles [13] confirm Adam&Gibbs theory, which predicts cooperative motions in dense liquid near jamming.

in the large stress distribution. Only small proportion of disks carry large forces, and they tend to align up in chains. This suggests the strong spatial correlation between these large forces in the direction of force chains. And the probability distribution of the normal forces and tangential friction is plotted in Fig. 1.3(b). The normal force has a peak around the mean, and has a exponential decay for more than the mean. And the tangential friction force also has a exponential decay. It is believed that those exponential tails for large forces are directly related to the force chains in Fig. 1.3(a). Therefore, the probability of force distribution is a simple but useful statistics for force networks in jammed materials.

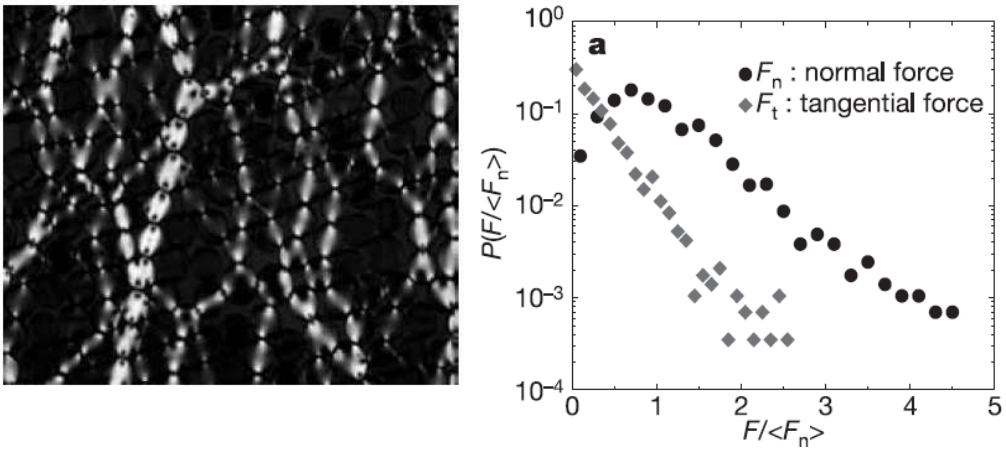

Figure 1.3: (a) Force chains of 2 dimensional photoelastic disks under shear from [19]. The photoelastic disk can change its polarization under stress. Due to the birefringence, forces can be observed by placing disks between two perpendicular polarizers. Therefore the bright area in the image is where the birefringence changes most, which corresponds to the large stress. The force distribution is heterogeneous, with small amount of grains carrying most of the large stresses. Besides, the large forces (brightness) tend to align up in chains. This suggests a spatial correlation between large stresses in this random structure. The particle used in the experiment are either 0.8 cm or 0.9 cm in diameter and 0.6 cm in height, with a friction coefficient of 0.8. To prevent any crystallines in the dense packing, the number ratio of same to large disks is 4 1. (b) Probability distributions of the normal contacts F_n and tangential friction F_t in (a) from [19]. Both forces are normalized by the mean normal force. The normal force has a peak around the mean, and has a exponential decay for more than the mean. It is believed that this exponential tail for large forces is directly related to the chain-like stress distribution in (a).

This exponential tail of force distribution is not only found in 2 dimensional gran-

ular disks but also in 3 dimensional grains. Because it is hard to see force distribution in a 3D bulk, people measure the stresses on surfaces as shown in Fig. 1.4. By plotting the probability distribution of forces, the exponential decay are also found in 3D grains, like that in 2D disks. The similar shape of force distribution suggests that in the 3D bulk force chains may also exist in grains [20]. Therefore, 2D system is a useful tool for investigating the properties of 3D materials.

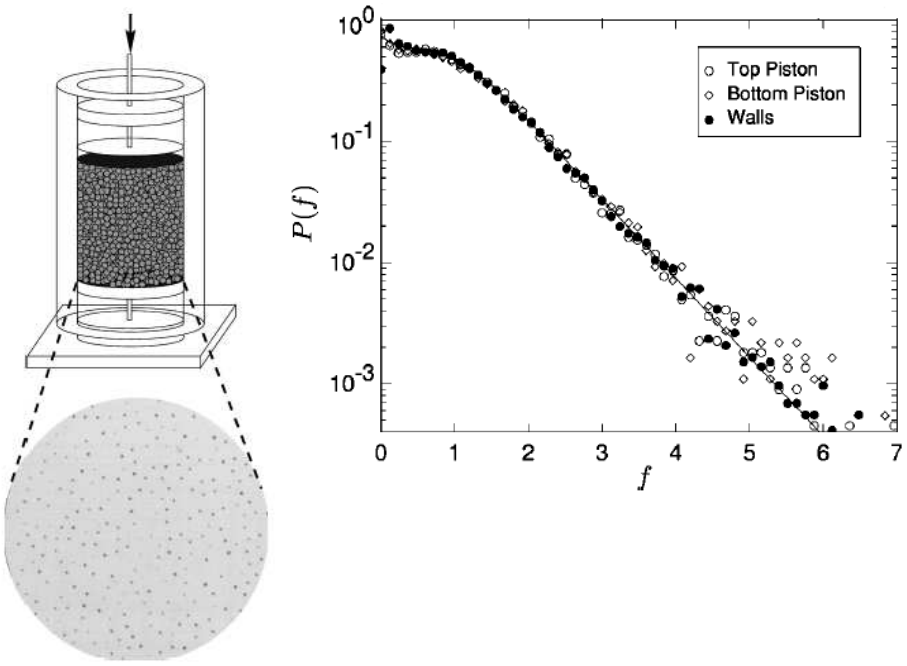

Figure 1.4: (a) The sketch of the apparatus used for experiments with "floating walls" from [21]. Grains are soda lime glass beads with diameter 3.5±0.2 mm. Beads are confined in an acrylic cylinder of 140 mm inner diameter. This is the cylinder wall that supports the beads by friction. A load is applied to the upper piston, and beads press the carbon paper into white paper. The view of the carbon paper is 76 mm across. The forces are determined based on the area and darkness of the dots. (b) The distribution $P(f)$ of normalized forces f against the top piston (open circles), the bottom piston (diamonds), and the walls (solid circles). The fitting curve is $P(f) = a(1 - b\exp(-f^2))\exp(-\beta f)$.

Since only small fraction of total grains carry most of large stresses, this force chain structure is fragile if under larger strain. It is found that under slow deformation, changes of stress chains cause strong temporal fluctuations on the wall [22]. As shown in Fig. 1.5, under slow shearing of jammed material with packing fraction > 0.777,

big fluctuations are detected in the company of force chain breakdown and buildup. During the big fluctuations, usually called "avalanche" events, big stress or energy is released. One common example for this "avalanche" is earthquakes, where huge energy is released during a short time scale. The force fluctuation is also found in dense granular flow of other geometries. For example, stress fluctuation on the side wall is detected, when densely packed grains flow through a hopper [23], as shown in Fig. 1.6. Due to the friction between grains and wall, the flux rate in this experiment is constant, independent of the height. Therefore, the stress fluctuation on the wall should come from the change of force chains inside the granular flow.

Simulation found that in absence of tangential friction, the spatial correlation between large stresses would persist to a longer length scale, and the heterogeneity of stress distribution would be stronger [24]. Due to the development of microscope technique, two groups recently [25, 4] calculate the interaction forces from the images of deformed droplets. They found long force chains in frictionless emulsion, confirming previous simulations. Besides, in the probability distribution of forces, Fig. 1.7, the exponential tails of large stresses are found in both polydisperse and monodisperse droplets. Besides, under large compression, the tail shape does not change too much. Therefore, frictionless emulsion is an important model for understanding the force correlation or force chains in jammed materials.

Limited by the imaging speed of microscope technique in 3D emulsion, one of the unsolved questions is how droplets rearrangements in the driven flow during "avalanche" events. And this is the issue my emulsion experiment addresses on (Chapter 7). Similar to the idea of 2D photoelastic disks, I use 2D emulsion disks to probe the jamming properties in 3D frictionless materials (see Chapter 7). One advantage is the image taking is easy and fast, comparing to the 3D microscope technique [25, 4]. Therefore, I can study both the droplet dynamics and their interactions at the same experiment. In this way, I can investigate the relation between rearrangements in mi-

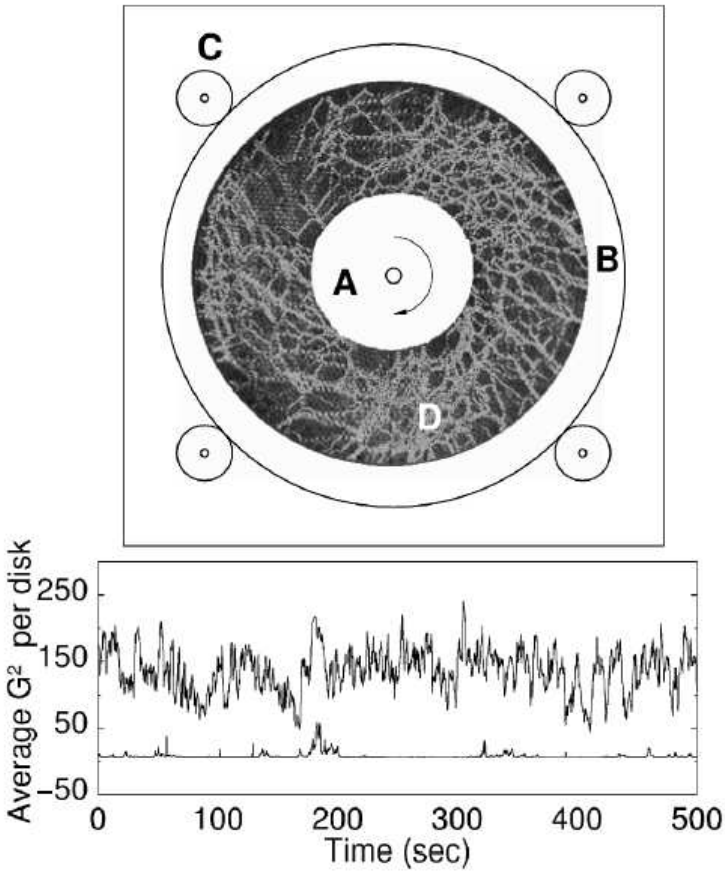

Figure 1.5: (a) Force chains of 2D photoelastic disks in a Couette shear experiment from [22]. Inner wheel (A) (radius 10.34 cm) rotates creating shearing on disks (D). Outer ring (B) (inner radius 19.14 cm) is confined by planetary gear (C). To avoid crystallines, binary disks are used ($\sim 400d = 0.9$cm and $\sim 2500d = 0.74$cm) with 6 mm thickness. To enhance shearing, the inner surfaces of the Couette shear cell is coated by plastic "teeth" spaced 0.7 cm apart and 0.2 cm deep. (b) Representative time series for stress fluctuation integrated over $\sim$1/10 of the disks. The stresses are calculated from the bright bands on photoelastic disks under shear [19], where $G^2 = |\nabla I|^2$. The lower tracer is just above critical packing fraction 0.777, and the upper trace has the packing fraction 0.803.

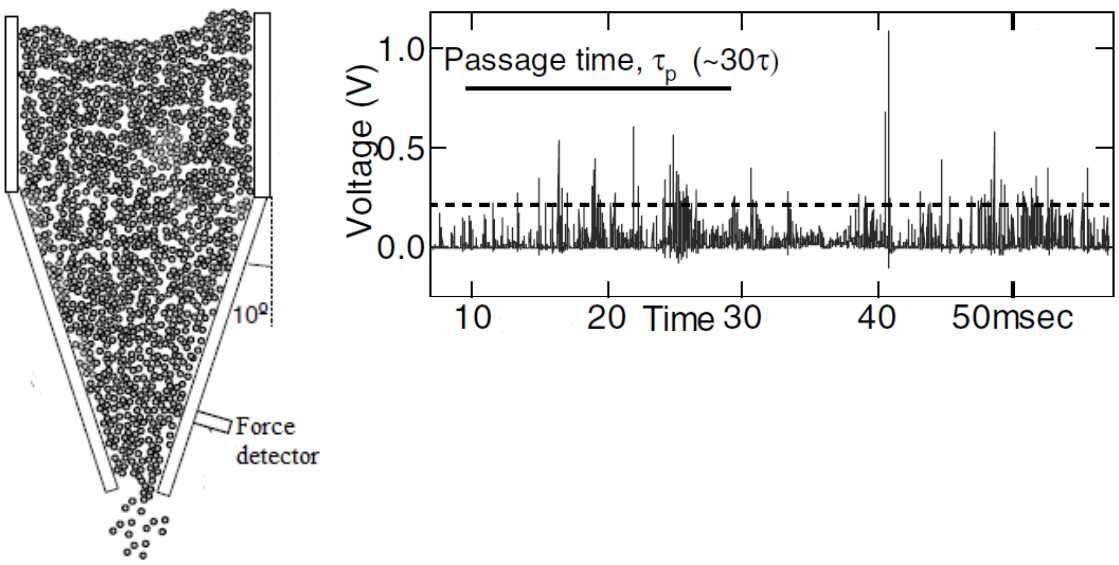

Figure 1.6: (a) Sketch of the experimental setup from [23]. Densely packed steel balls flow through a hopper under gravity. The ball has a size of 3.125 mm in diameter. A force detector is on the side wall of the hopper, and the voltage signal from the detector is recorded. (b) A section of the voltage (force) trace as a function of time during a drain. The horizontal dashed line shows an time averaged voltage (force).

cro scale and the "avalanche" events in macro scale. Besides, it is always interesting to compare 2D frictionless disks with the 2D granular ones, since friction may affect the force chains in jammed materials [24].

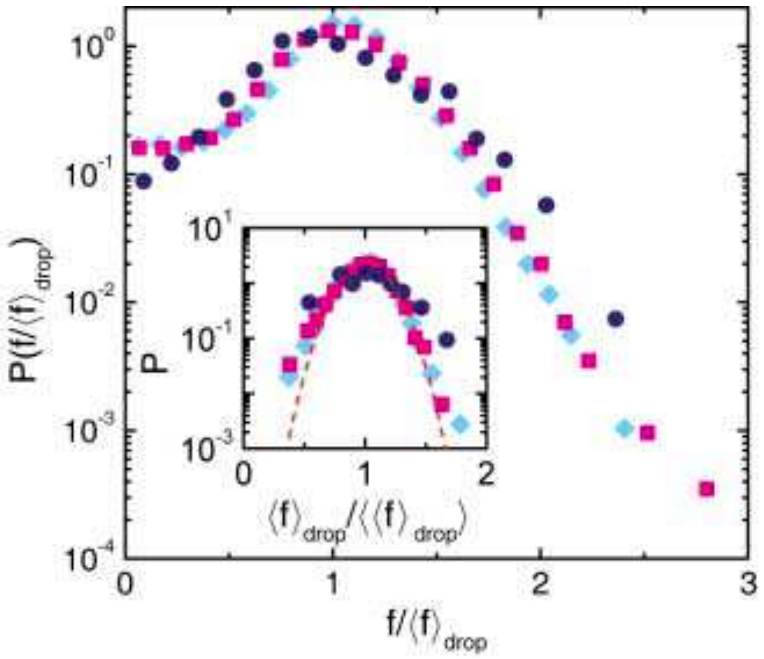

Figure 1.7: Probability distribution of contact forces in 3D dense emulsion without static friction from [4]. The force on each droplet is normalized by the mean force on the droplet $\langle f\rangle_{drop}$. The mean droplet size is $\sim 30\mu$m. Three symbols represent three droplet samples: diamond for polydisperse, squares for polydisperse too but under extra compression, and circle for monodisperse. The inset is the distribution of $\langle f\rangle_{drop}$, normalized by the sample mean, $\langle\langle f\rangle_{drop}\rangle$. The dashed curve is a Gaussian fit to the polydisperse sample.

Chapter 2

Experimental techniques on colloids

2.1 Colloid

2.1.1 What is a colloid

Colloids are microscopic solid particles in a liquid, such as toothpaste, paint, and ink. The sizes of colloidal particles typically range from 1 μm to 1 mm, and Brownian motion from thermal fluctuation is important. This is in contrast with large grains or emulsion droplets, for which thermal motion is neglectable. The colloids I use for shearing experiment (Chapter 4) are poly-methylmethacrylate (PMMA), which are the same polymer known as Plexiglas^{TM} on a large scale. To prevent aggregation, the PMMA spheres are coated with sterically stabilizing agent poly-12-hydroxystearic acid (PHSA) [26]. For visualization, colloids are dyed with rhodamine $6G$, either after swelling them or when the colloids are synthesized [27, 28, 29]. The solvent is a mixture of 85% cyclohexybromide and 15% decalin by weight. As mentioned in Section 2.2, for 3D confocal imaging, this solvent matches both the density and the index of refraction of PMMA colloids. The interaction between the colloids is steric

repulsion within a very short distance comparing to colloidal size. Therefore, colloids are nearly ideal hard spheres [30], and become a good model to test the theories and simulations on dense liquid. The PMMA colloids in Weeks' lab are from Andrew Schofield in University of Edinburgh, and a 3D image of them is shown in Fig. 2.2(b).

2.1.2 Phase transition of hard-sphere system

One of the control parameters for the hard-sphere system is volume fraction ϕ, which is the ratio of total volume taken by particles to the that of the whole suspension. For monodisperse colloidal suspension, the spherical volume fraction is $\phi = (4\pi/3)a^3n$, where a is the radius and n is the number density. Fig. 2.1 is the phase diagram for monodisperse hard-sphere colloidal system controlled by volume fraction ϕ [31]. In a dilute suspension, $0 < \phi < 0.494$, particles are far from each other and diffuse freely like in a simple liquid. Those spheres remain in a disordered state until $\phi > 0.494$, when crystallines start to appear. And when $\phi > 0.545$, the whole suspension has a ordered crystal structure. And according to the mathematical geometry, this ordered structure has a most dense packing $\phi = \frac{\pi}{3\sqrt{2}} = 0.74$, with hexagonal close packed (HCP) layers. In addition to these equilibrium phases, colloids can also have non-equilibrium behavior. For example, at $\phi = 0.55$, if particles quickly sediment down by centrifuging, they would pack randomly without enough time to explore the entropy favored crystallization state under Brownian motion. And in such dense packing, particles are kinetically trapped, and this random structure could remain for a long time. In experiment (Chapter 4), we use centrifuging to get dense colloidal suspension in disordered structures. When $\phi > \phi_g \approx 0.58$, the system acts like a glass. The transition is the point where particles no longer diffuse through the sample. For $\phi < \phi_g$ spheres, the supercooled liquid region, particles do diffuse at long times, although the asymptotic diffusion coefficient D_∞ decreases sharply as the concentration increases [32, 33, 34]. Therefore, the difference between the supercooled

liquid and the glass is the previous could reach equilibrium crystallization state after a long time; while the glass never reach crystallization, or the diffusion time is infinite long. It should be noticed that the glass transition at ϕ_g occurs even though the spheres are not completely packed together; in fact, the density must be increased to $\phi_{\mathrm{RCP}} \approx 0.63$ for "random-close-packed" (RCP) spheres (proved in math) [24, 35, 36, 37, 38] before the spheres are motionless.

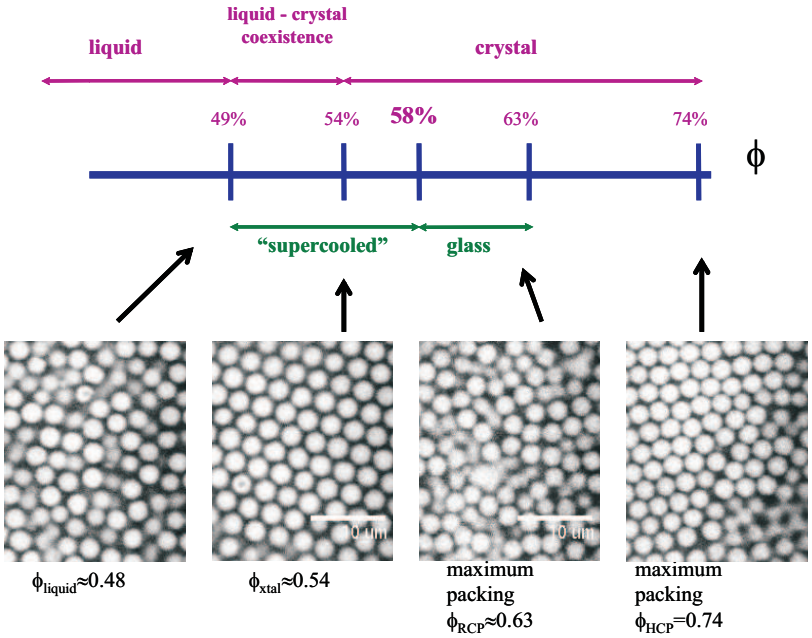

Figure 2.1: Phase diagram of hard sphere system by the control parameter volume fraction ϕ from [31]. The states above (pink labeled) are equilibrium states, and the one below (green labeled) are non-equilibrium. The bottom are colloids images for four different states: liquid, liquid-crystal coexistence, densest random packing, and densest crystallization.

2.2 Confocal microscope

Although the bright-field microscope is simple and fast (30 frames per second), there are some limits especially for 3D imaging. In my colloidal shearing experiment (Chapter 4), to investigate the 3D structure changes during shearing, we use a fast confocal microscope. Similar to an ordinary fluorescent microscope, a confocal microscope uses

laser light exciting the fluorescent dye in a sample, and then collects the emitting light. But the special designs of confocal microscopy are point to point illumination of the sample, and rejection of out of focus light [31, 39]. Fig. 2.2(a) shows the working principle of a confocal microscope. Laser light (blue line) is directed by the dichroic mirror towards rotating mirrors, scanning the sample in xy plane point by point. The fluoresced light (green line) from the sample then returns back in the same path as the laser light before the dichroic mirror. Because the fluoresced light has lower frequency (lower energy) than the laser light, the dichroic mirror lets it passing through toward the detector rather than reflecting to the laser source. Before the detector, there is a screen with a pinhole, placed in the "conjugated focal plane" of the sample, which is the origin of the "confocal" term. This pinhole design rejects all out-of-focus light, and only allows the focus point reaching to the detector. As shown in Fig. 2.2(b), a 3D image is a stack of 2D slices in xy focal plane at different depths along z direction (optical axis). Our confocal has a piezo-actuator, moving objective lens along z axis in very small increments up to 0.2 μm limit. Therefore, the imaging speed of a confocal microscope depends on the rotating mirrors and the piezo-actuator. The confocal microscope in my colloid experiment (Chapter 4) is "VT-Eye" from Visitech^{TM}. The imaging speed for 2D graphs goes up to 300 frames per second. Given that one 3D graph is a stack of 2D image slices, the 3D speed I could get in experiment is 0.3 frames per second, by using 100 slices in the z direction.

For my dynamic experiment (see Chapter 4), it is important to consider the time lag from the top slice of a 3D stack to the end slice, making sure they are not moving significantly to each other. Therefore, I need to balance the dynamic speed with acquisition time for one stack. Another consideration for the 3D imaging is that the resolution is better in xy focal plane than the z optical axis. Besides, confocal microscopy has specific requirements on the sample for a clear 3D image. For example, in my colloidal experiment (Chapter 4), I use poly-methylmethacrylate (PMMA)

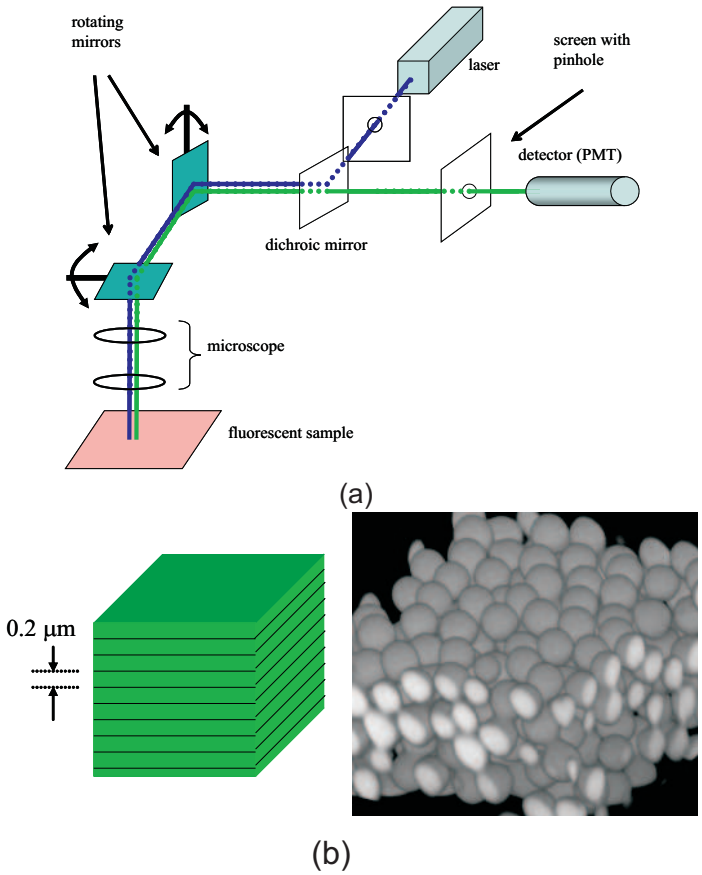

Figure 2.2: (a) Working principle of confocal microscopy from [31]. It is almost same as a normal fluorescent microscope: the laser provide excitation light, and excite the emission photons from the fluorescent sample with a lower frequency. The excitation and emission light share the same path before meeting the dichroic mirror. This mirror reflects the high frequency excitation light but let the low frequency emission light passing through to the detector. This special design for the "confocal" is the pinhole in front of the detector. It collects the light in focus and filters out other light from the background. Therefore, a confocal microscope actually images only one point at a instant time. The rotating scanning mirrors allow the microscope reading the sample in the focus plane. In this way, a confocal microscope give a clear 2D image by trading off the speed. (b) One 3D image of a confocal microscope is a stack of 2D ones. Typically, the resolution in x and y directions are 0.2 μm, and in z direction is 0.5 μm. Therefore, z direction determines the resolution of the whole 3D image. On the right it is the reconstructed 3D image of PMMA colloids with the diameter of 2.3 μm.

colloids in a mixed solution (85% cyclohexybromide and 15% decalin by weight). In this sample, the index of refraction of the colloids and the solution match. Otherwise, laser light could not pass deep into the dense suspension before refraction. In addition, to avoid gravity effect, the density of the colloids also matches with the suspension. And those sample details about colloids are explained in Section 2.1.

Chapter 3

Computer programming on colloids

In Weeks' lab, we have a suite of particle tracking programs, analyzing microscopic structures of soft materials. The software we use is Interactive Data Language (IDL) by ITT Visual Information Systems. Similar to Matlab, its algorithm is a matrix based scientific programming language, with packages of mathematical function, data analysis tools, scientific visualization, and animation tools.

3.1 Colloid identification algorithm

From the 3D movie taken by a confocal microscope, we need to identify particle locations. The algorithm is originally from John Crocker and David Grier [40]. Although the program is designed for images of bright spheres on dark background, we found it works as well for non-spherical objects [41].

The steps for colloid identification is as following: The first step is to filter out noise with very low or very high spatial frequency, by using a spatial bandpass filter. This step smooths out neighbor pixel variation and eliminates image noise. Short wavelength noise comes from the image detecting. For example, the readout noise is caused by camera operation and electronic circuits. The dark current noise is from the thermal noise of silicon chips. The shot noise is caused by light intensity, bigger

fluctuation for lower intensity. Long spatial wavelength noise may come from the slight misalignment of the optics. As shown in Fig. 3.1(a) and (b), the image looks clearer after filtering out low and high frequencies.

The second step is to identify the centers of spherical colloids. In an ideal case, the spherical center should also be the weight center of brightness in the range of particle radius r_0. But in the real image, the brightest voxel could be off center due to the noise. Therefore, the idea of the center identifying program is to find particle centers which are also near to the weight centers of the brightness. At the beginning, the program chooses the center as the point brighter than its neighbors and also among 30% brightest voxels of the whole image. Then given the particle radius r_0 as a parameter, the program calculates the weight center of brightness around the particle position. If the weight center is more than half a voxel away from the particle center, it is then identified as the new center for the spherical particle. And this center swap keeps repeating until the center difference is less than 0.5 voxel. This refinement procedure could obtain the particle centers with the resolution less than 1/10 of the pixel size. The accuracy of center identification is also dependent on how many pixels across a particle. Given that the actual pixel resolution of our confocal microscope is $\sim$0.2 μm, the size of colloids I used is 2 μm in diameter, which covers $\sim$10 pixels in x,y and z directions. As shown in Fig. 3.1(c), the possible positions of particles are labeled by the red dots. However, some of them are mislabeled with no particles there due to the noise.

The third step is then to remove any false particles. When looping refinement procedure for candidate particle locations, other quantities of each sphere image's brightness distribution are calculated. And basing on that, we could distinguish spherical colloids from noise. For example, in Fig. 3.1(d), we plot the sphere's radius vs. its brightness for all possible colloids. Usually the brightest ones are real colloids, and we can see two distinct points at the upper right corner with large brightness

and proper radius sizes. And the particle centers of the two dots in the image is in Fig. 3.1(e). In the similar way, we could also distinguish real particles from noise by checking other brightness quantities. For instance, colloids should be identified as spheres in images. So if particle candidates look like rods with large eccentricity, that could be fake ones, or at least need to be pick up for further checking.

3.2 Tracking algorithm

Particle tracking is important for understanding microscopic structure changes in soft materials. The tracking algorithm for non-interacting colloids is devised by John Crocker and David Grier [40]. The cost function of the algorithm is the mean squared frame to frame displacement of particles (MSFD) [42]. Within the tracking range of the old positions, the algorithm chooses the new positions in the following frame by minimizing the MSFD. There are some limits in this tracking algorithm. Given that the tracking procedure basically compares particles' positions in consecutive frames, if a particle does not move too much, the program could follow it near the old position in the next frame. However, if a particle moves too fast, over the average inter-particle distance, the program could not distinguish it from its neighbors between consecutive frames. Therefore, for very dense liquid with short inter-particle distance, imaging speed has to be fast enough to match up the short inter-particle distance. Besides, the classic Crocker&Grier's algorithm was designed for self-diffusion system, where particles move randomly due to Brownian motion. If there is any large driven motion in colloidal flow, the particles' moving distance would be larger than inter-particle space.

In my colloid shearing experiment (Chapter 4), because of the tracking limit of the classic Crocker&Grier (CG) mentioned above, we use a algorithm similar to the iterated CG tracking algorithm [42]. The idea is to first find out overall average

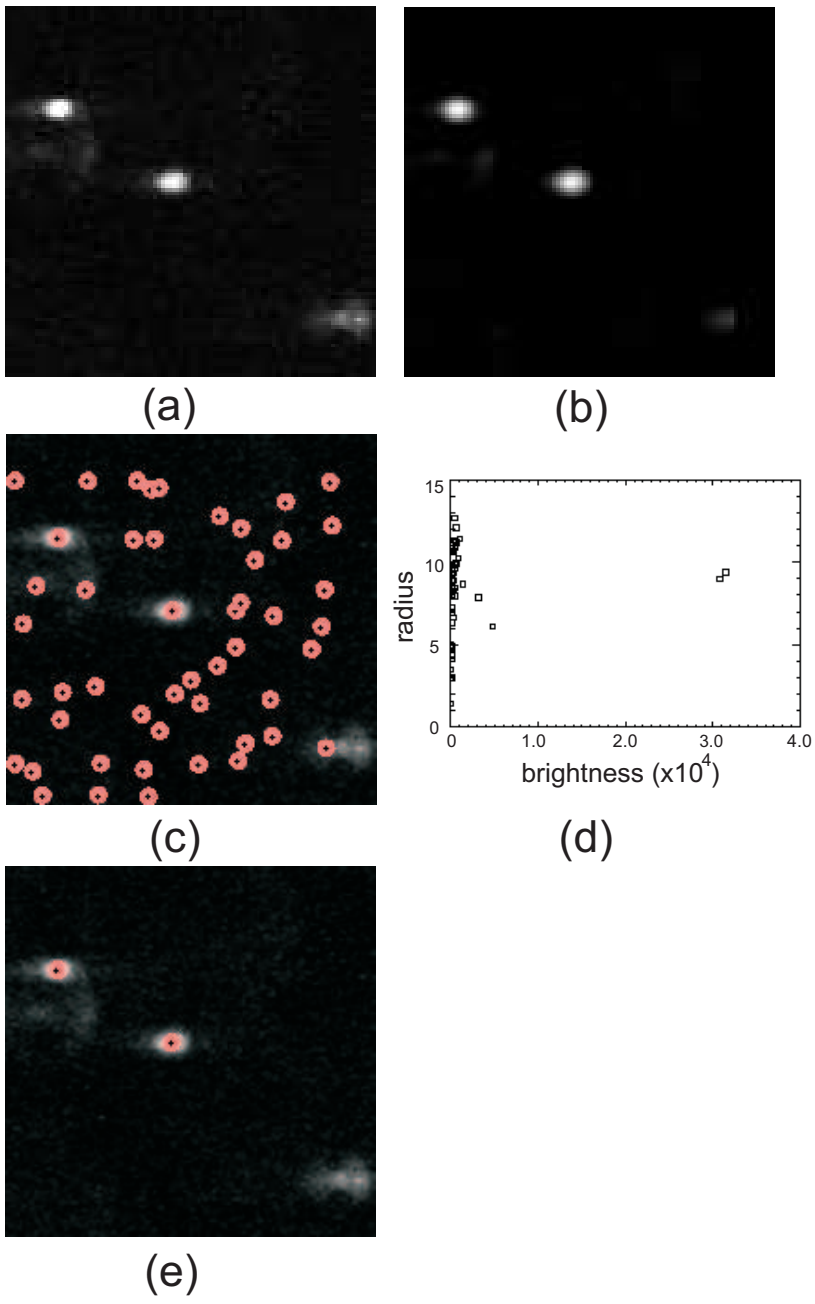

Figure 3.1: (Color online) Steps for spherical colloid identification. The image is from http://www.physics.emory.edu/∼weeks/idl/tracking.html. The particles are 2 μm diameter colloids. For a raw image (a), we first filter out the noise with too high or too low frequency (b). Then we find particle centers (c) from the looping refinement procedure [40]. To distinguish real spheres from noise, the spheres' radius vs. brightness is plotted (d). And the two brightest spheres from (d) are identified as real particles, which are plotted in (e).

shear-induced motion of the colloidal suspension, then remove the motion from all of the particles' trajectories and re-track particles in the "co-shearing" reference frame, and finally add back in the shear-induced motion that previous removed.

In Besseling's iterated CG tracking algorithm, the removed coherent motion is obtained from the initial tracking by using the classic CG algorithm. It works well for the movie under slow shearing but not for the fast shearing. The classic CG algorithm is originally designed for particles with random small motion, so it has a speed limit on tracking. Therefore, to obtain the coherent motion under fast shearing, we use the method "correlated imaging tracking" or "particle image velocimetry" (PIV). The idea of the PIV method is to find the best overlapping by moving around between consecutive images at the same z depth. And the distance shifts with the maximum image correlations, are the average motions of all particles in the sample, as shown in Fig. 3.2. The standard PIV image correlation is [42]: Given two consecutive 2D images at time i and $i-1$ at a region of n×m pixel size, $I_i(x,y)$ and $I_{i-1}(x,y)$ are the intensities at position (x,y) at time i and $i-1$. The covariance is defined as

$$cov[I_{i-1}(x,y), I_i(x,y)] = \frac{1}{[(n\times m)-1]}\sum_{p=1}^{n}\sum_{q=1}^{m}[I_{i-1}^{pq} - \langle I_{i-1}\rangle][I_i^{pq} - \langle I_i\rangle], \tag{3.1}$$

where $I_i^{pq}(x_p, y_q)$ is the intensity at (x_p, y_q). The average intensity for the entire image $\langle I\rangle$ is $\frac{1}{[n\times m]}\sum_{p=1}^{n}\sum_{q=1}^{m} I^{pq}$. And the variance of a single image is

$$var[I(x,y)] = \frac{1}{[(n\times m)-1]}\sum_{i=1}^{n}\sum_{j=1}^{m}[I^{ij} - \langle I\rangle]^2. \tag{3.2}$$

Then the correlation $c[I_{i-1}(x,y), I_i(x,y)]$ of the two images is

$$c[I_{i-1}(x,y), I_i(x,y)] = \frac{cov[I_{i-1}(x,y)I_i(x,y)]}{\sqrt{var[I_{i-1}(x,y)]var[I_i(x,y)]}}. \tag{3.3}$$

By a shift $(\Delta X', \Delta Y')$ between the two images, the correlation is $c[I_{i-1}(x,y)I_i(x -$

$\Delta X', y - \Delta Y')$. And the maximum correlation in a desired range corresponds the optimum shift $(\Delta X, \Delta Y)$. From a series of xy plane shifts $(\Delta X(z), \Delta Y(z))$ at different depth z, we could obtain the shear motion. One advantage of the second way, PIV method, is no requirement for the identification of individual particles as in the first one. So the PIV method could be used for obtaining larger average motion. By combining the tracking algorithms of iterated CG and imaging correlation, we could track particles under fast shearing.

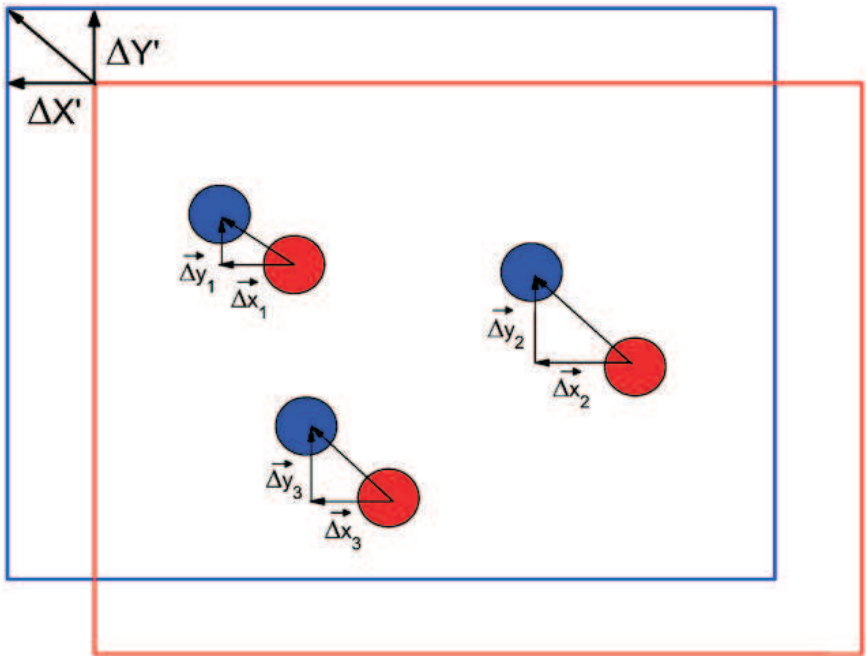

Figure 3.2: (Color online) Illustration of the shifting and correlation procedure from [42]. Particles moves over displacement $(\Delta x, \Delta y)$ between frame 1 and frame 2. The entire image is shifted over a range of $(\Delta X', \Delta Y')$, and the maximum correlation corresponds to the optimum shift $(\Delta X, \Delta Y)$.

Chapter 4

Microscopic structural relaxation in a sheared supercooled colloidal liquid

The rheology of dense amorphous materials under large shear strain is not fully understood, partly due to the difficulty of directly viewing the microscopic details of such materials. We use a colloidal suspension to simulate amorphous materials, and study the shear-induced structural relaxation with fast confocal microscopy. We quantify the plastic rearrangements of the particles in several ways. Each of these measures of plasticity reveals spatially heterogeneous dynamics, with localized regions where many particles are strongly rearranging by these measures. We examine the shapes of these regions and find them to be essentially isotropic, with no alignment in any particular direction. Furthermore, individual particles are equally likely to move in any direction, other than the overall bias imposed by the strain. This work has been published in [43].

4.1 Motivation

Many common materials have an amorphous structure, such as shaving cream, ketchup, toothpaste, gels, and window glass [44, 45, 46, 47]. In some situations these are viscous liquids, for example when window glass is heated above the glass transition temperature, or a shaving cream foam that has been diluted by water to become a liquid with bubbles in it. In other situations these are viscoelastic or elastic solids, such as gels and solid window glass [2]. For solid-like behavior, when a small stress is applied, the materials maintain their own shapes; at larger stresses above the yield stress, they will start to flow [48, 49, 50]. Understanding how these materials yield and flow is important for the processing of these materials, and understanding their strength in the solid state [51, 52, 53].

A particularly interesting system to study is a colloidal suspension. These consist of micron or submicron sized solid particles in a liquid. At high particle concentration, macroscopically these are pastes and thus of practical relevance [48]. Additionally, for particles with simple hard-sphere like interactions, colloidal suspensions also serve as useful model systems of liquids, crystals, and glasses [30, 54, 55, 9]. Such colloidal model systems have the advantage that they can be directly observed with microscopy [56, 31, 57]. Our particular interest in this chapter is using colloidal suspensions to model supercooled and glassy materials. The control parameter for hard sphere systems is the concentration, expressed as the volume fraction ϕ, and the system acts like a glass for $\phi > \phi_g \approx 0.58$. The transition is the point where particles no longer diffuse through the sample; for $\phi < \phi_g$ spheres do diffuse at long times, although the asymptotic diffusion coefficient D_∞ decreases sharply as the concentration increases [32, 33, 34]. The transition at ϕ_g occurs even though the spheres are not completely packed together; in fact, the density must be increased to $\phi_{\mathrm{RCP}} \approx 0.64$ for "random-close-packed" spheres [24, 35, 36, 37, 38] before the spheres are motionless. Prior work has shown remarkable similarities between colloidal suspensions and conventional

molecular glasses [30, 32, 58, 59, 60, 61, 62, 63, 64].

One important unsolved problem related to amorphous materials is to understand the origin of their unique rheological behavior under shear flow. Early in the 70's, theory predicted the existence of "flow defects" beyond yielding [51], later termed shear transformation zones (STZ) [8]. These microscopic motions result in plastic deformation of the sheared samples [65, 66]. Simulations later found STZs by examining the microscopic local particle motions [53, 67, 68]. Recently fast confocal microscopy has been used to examine the shear of colloidal suspensions [69], and STZ's have been directly observed [9]. This provided direct evidence to support theoretical work on STZ's [51, 70, 8, 71].

However, questions still remain. First, most of the prior work has focused on the densest possible samples, at concentrations which are glassy ($\phi > \phi_G$) [69, 9]. Given that the macroscopic viscosity of colloidal suspensions change dramatically near and above ϕ_G [72], it is of interest to study slightly less dense suspensions under shear, for which rearrangements might be easier [13]. In this chapter, we present such results. Second, prior investigations of sheared amorphous materials have used a variety of different ways to quantify plastic deformation [73, 74, 69, 9]. In this chapter, we will compare and contrast plastic deformations defined in several different ways. While they do capture different aspects of plastic deformation, we find that some results are universal. In particular, in a sheared suspension, there are three distinct directions: the strain velocity, the velocity gradient, and the direction mutually perpendicular to the first two (the "vorticity" direction). We find that plastic deformations are isotropic with respect to these three directions, apart from the trivial anisotropy due to the velocity gradient. The deformations are both isotropic in the sense of individual particle motions, and in the sense of the shape of regions of rearranging particles.

4.2 Experimental details

The experimental setup of our shear cell is shown in Fig. 4.1 and is similar to that described in Refs. [75, 69]. The glass plates are 15 mm in diameter, and to the top plate is glued a small piece of glass with dimensions 5 mm×1 mm, with the long dimension oriented in the direction of motion x. The purpose of this piece of glass is to decrease the effective gap size. Between the plates are three ball bearings, used to control the gap size; for all of our data, we maintain a gap size of $H = 130$ μm. Over the 5 mm length of the small pieces of glass, the gap varies by no more than 15 μm; over the narrower dimension of the small pieces of glass, the gap varies by no more than 10 μm. Thus, overall the sample is between two plates which are parallel to within 1% and in the direction of shear, they are parallel to within 0.3%.

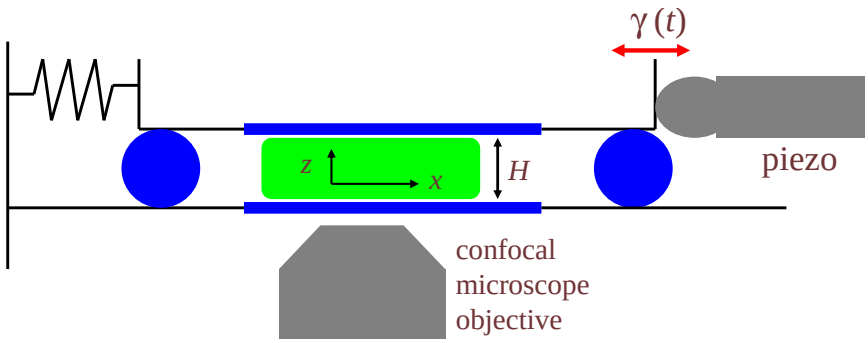

Figure 4.1: (Color online) Sketch of the shear cell. A fluorescent sample (gray, green online) is put between two parallel glass plates (dark gray, blue online) with gap H set by three ball bearings, two of which are shown. The top plate is movable, controlled by a piezo motor driven by a triangular wave. The bottom plate is fixed, and the confocal microscope takes images from underneath. Note the definition of the coordinate system, where x is in the velocity direction and z is in the velocity gradient direction.

A droplet of the sample (volume ∼200 μl) is placed between the two pieces of glass. The top plate is free to move in the x direction, and the bottom plate is motionless. The shear rate is controlled by a piezo-electric actuator (Piezomechanik GmbH Co.) driven by a triangular wave signal with a period ranging from $T = 150$ to 450 s and an amplitude of $A = 175$ μm. Thus we achieve strains of $\gamma_0 = A/H = 1.4$. Prior to

taking data, we allow the shear cell to go through at least one complete period, but usually not more than three complete periods.

Our samples are hard-sphere colloids (Fig. 4.2), as introduced in Section 2.1. And the volume fraction ϕ is in the range of "supercooled liquid".

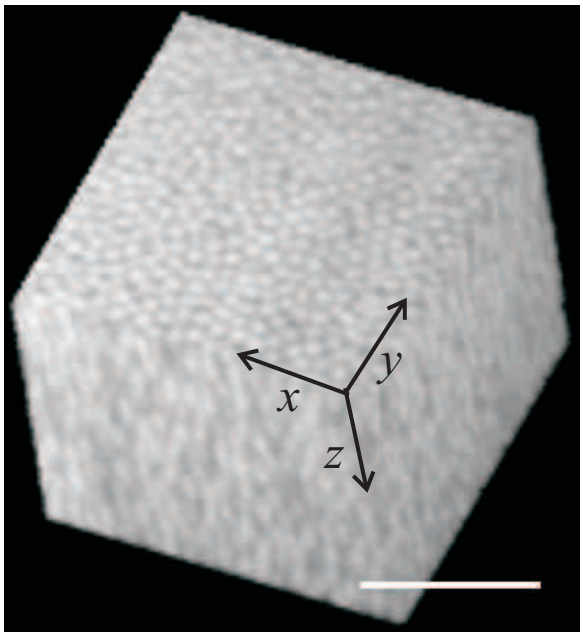

Figure 4.2: A 20×20×20 μm^3 image of a supercooled colloidal liquid taken 15 μm away from the fixed bottom plate by our confocal microscope in less than 1 s. The scale bar represents 10 μm.

To characterize the relative importance of Brownian motion and the imposed strain field, we can compute the modified Peclet number, $Pe^\star = \dot{\gamma}a^2/2D_\infty$, where D_∞ is the long time diffusion coefficient of the quiescent sample. We measure D_∞ from mean square displacement data taken from the quiescent sample with the same volume fraction. The large Δt data for the mean square displacement can be fit using $\langle \Delta x^2 \rangle = 2D_\infty \Delta t$. Roughly, $a^2/2D_\infty$ reflects the average duration a particle is caged by its neighbors in the dense suspension.

$\dot{\gamma}$ is the imposed strain rate $2A/(HT)$, and a is the particle size. The extra factor of 2 in $\dot{\gamma}$ is because we use a triangle wave, and thus the half period sets the strain rate. For our samples, we find $D_\infty \approx 5 \times 10^{-4}$ μm^2/s, and we have $\dot{\gamma}$ ranging from

0.0060 to 0.0180 s^{-1}; thus $Pe^\star \approx 7 - 20$. Given that $Pe^\star > 1$, the implication is that the motions we will observe are primarily caused by the strain, rather than due to Brownian motion. We use the modified Peclet number based on D_∞ rather than the bare Peclet number based on the dilute-limit diffusivity D_0, as we will focus our attention on the dynamics at long time scales, which we will show are indeed shear-induced.

Shear-induced crystallization has been found in previous work [76, 77]. As we wish to focus on the case of sheared amorphous materials, we check our data to look for crystalline regions using standard methods which detect ordering [78, 79, 80, 81, 82]. Using these methods, we find that particles in apparently crystalline regions comprise less than 3% of the particles in each of our experiments, and are not clustered, suggesting that the apparently crystalline regions are tiny. This confirms that our samples maintain amorphous structure over the time scale of our experiments, although perhaps if we continued the shearing over many more cycles we would find shear-induced crystallization.

We use a confocal microscope to image our sample (the "VT-Eye", Visitech), using a 100× oil lens (numerical aperture = 1.40) [83, 39, 31]. A 3D image with a volume 50×50×20 μm^3 is acquired in less than 2 s; these images contain about 6000 particles. The 3D image is $256 \times 256 \times 100$ pixels, so approximately 0.2 μm per pixel in each direction. Figure 4.2 shows a representative image from a somewhat smaller volume. The 2 s acquisition time is several orders of magnitude faster than the diffusion for particles in our high volume fraction sample. To avoid any boundary effects [84], we scan a volume at least 20 μm away from the bottom plate. Particle positions are determined with an accuracy of 0.05 μm in x and y, and 0.1 μm in z. This is done by first spatially filtering the 3D image with a bandpass filter designed to remove noise at high and low spatial frequencies, and then looking for local maxima in the image intensity [40]. Our algorithms for colloid identification and tracking are

in Sections 3.1 and 3.2.

Due to the strain, particles that start near one face of the imaging volume are carried outside the field of view, while on the opposite face new particles are brought inside. Thus, for larger strains, the total number of particles viewed for the entire duration diminishes. For the data discussed in this work, we consider both instantaneous quantities and quantities averaged over the entire half-cycle of strain. For the former, we view ~ 5500 particles, while for the latter, we typically can follow ~ 3000 particles, which limits our statistics slightly.

4.3 Results

4.3.1 Locally observed strain

Our goal is to understand if the local shear-induced motion is isotropic in character. However, first we seek to understand and quantify the more global response of our sheared samples.

When shearing disordered materials or complex fluids, one often finds shear localization or shear banding, due to the nonlinear yielding and relaxation in local regions [49, 48, 85, 86]. To check for this in our data, we start by taking 3D images under the applied shear rate $\dot{\gamma}_{\text{macro}} = 0.016\ \text{s}^{-1}$ over a very large range in z, from 0 to 70 μm away from the bottom plate, almost half of the gap between two shearing plates. To allow us to visualize more clearly over such a large depth, we dilute the dye concentration by mixing dyed and undyed colloids at a number ratio of around 1:80 and keeping the desired volume fraction $\phi \approx 0.50$. Our sample does indeed form a shear band, as shown in Fig. 4.3 on the following page, which shows the particle velocity v_x in the direction of the shear as a function of the depth z. The velocity changes rapidly with z in the range $0 < z < 20$ μm, and then more slowly for $z > 20$ μm; thus much of the shear occurs adjacent to the stationary plate at $z = 0$ μm, similar

to prior work which found shear adjacent to one of the walls [87, 49, 48, 85, 86]. Furthermore, the velocity profile is relatively stable during the course of the half-period, as seen by the agreement between the velocity profiles taken at different times during this half period (different lines in Fig. 4.3. Thus, the shear band develops quickly inside the supercooled colloidal liquid, and remains fairly steady under the constant applied strain rate. The location and size of the shear band varies from experiment to experiment.

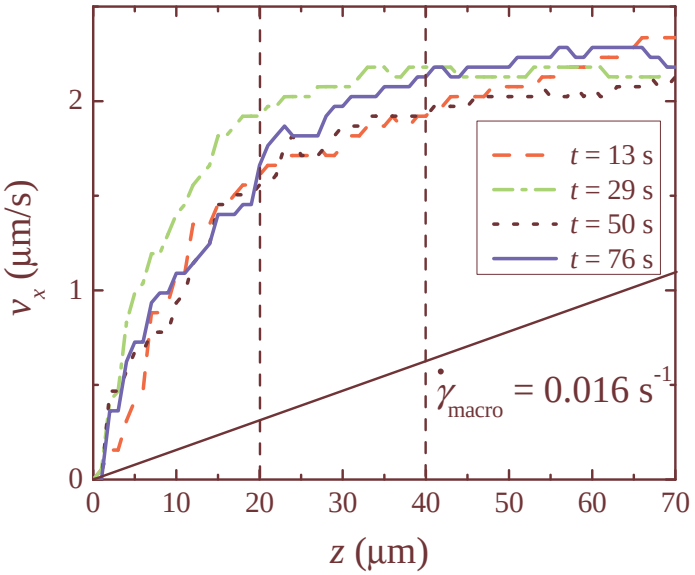

Figure 4.3: (Color online) Shear profile $v_x(z)$ within a 50×50×70 μm^3 volume, measured at different times during one half period $T/2 = 84$ s. The total macroscopic strain applied in 84 s is 1.35. The sample has a volume fraction $\phi \approx 0.50$, and the global applied shear rate is $\dot{\gamma}_{\mathrm{macro}} = 0.016$ s^{-1} controlled by the piezo motor. If there was not a shear band, one would expect to observe a linear velocity profile as indicated by the lower thick diagonal line. The four curves represent different times during the half period as indicated. Note that these data are obtained using a coarse-grained image velocimetry method [42], rather than particle tracking. Here we take rapid images over the full volume with a spacing of $z = 1$ μm in the vertical direction. For each value of z, we cross-correlate subsequent images to obtain a mean instantaneous velocity v_x with a resolution of 0.05 μm/s, set by the pixel size and the time between images. See Ref. [42] for further details.

Given the existence of a shear band, the applied strain is not always the local strain. In this work we wish to focus on the motion induced by a local strain, rather than the global formation of shear bands. Thus, for all data sets presented below, we

always calculate the local instantaneous strain rate $\dot{\gamma}_{\text{meso}}(t) = \frac{v_x(z+\Delta z,t)-v_x(z,t)}{\Delta z}$. Here $\Delta z = 20$ μm is the height of the imaged volume. Related to $\dot{\gamma}_{\text{meso}}$, we can calculate the total local applied strain by integrating $\dot{\gamma}_{\text{meso}}(t)$:

$$\gamma_{\text{meso}}(t) = \int_0^t \dot{\gamma}_{\text{meso}}(t')dt'. \tag{4.1}$$

Furthermore, we verify that for each data set considered below, $v_x(z)$ varies linearly with z within the experimental uncertainty, and thus $\dot{\gamma}_{\text{meso}}$ is well-defined, even if globally it varies (Fig. 4.3 on the preceding page).

While the shape of the shear band is essentially constant (Fig. 4.3 on the previous page), in many cases the local strain rate varies slightly with time. As our forcing is a triangle wave, over any given half cycle the global applied strain rate is a constant. We can measure the local strain rate for each data set; a typical example is shown in Fig. 4.4 on the following page. This figure shows the local instantaneous measured strain rate within the region 20 μm $< z <$ 40 μm, over one full period. After the shearing starts, $\dot{\gamma}_{\text{meso}}$ quickly rises up to 0.015 s^{-1}, implying that the shear band has formed. Subsequently, the local strain rate continues to increase up to 0.030 s^{-1} over the rest of the half period. The small fluctuations of $\dot{\gamma}_{\text{meso}}$ are due to the microscopic rearrangements of particles, which can be somewhat intermittent. Given that the local instantaneous strain rate is not constant (despite the constant applied strain rate), we will characterize our data sets by the time averaged local strain rate defined as

$$\bar{\dot{\gamma}}_{\text{meso}} = \frac{\gamma_{\text{meso}}(t)}{t} \tag{4.2}$$

typically using $t = T/2$, the half period of the strain. That is, we consider $\bar{\dot{\gamma}}_{\text{meso}}$ as one key parameter characterizing each data set, although we will show that we see little dependence on this parameter. In the rest of the chapter, the choice $t = T/2$ will be assumed, except where noted when we wish to characterize the mesoscopic

strain for time scales shorter than $T/2$.

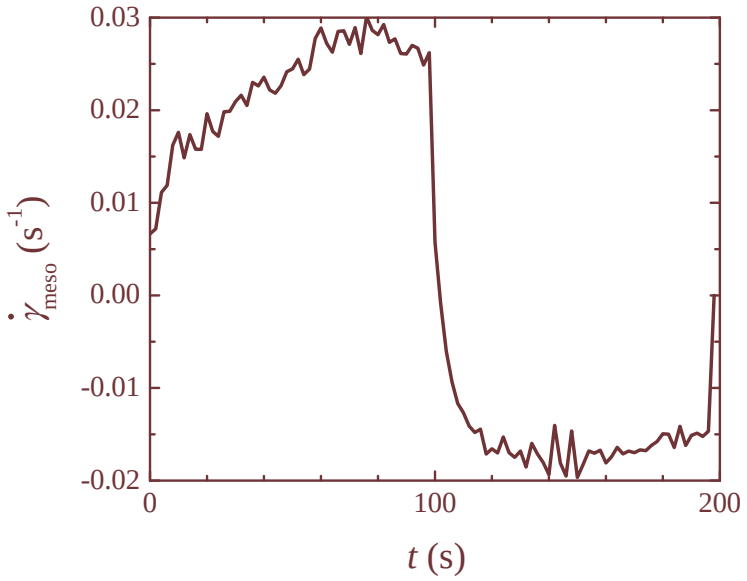

Figure 4.4: A typical example of a measured local instantaneous shear rate over one period of shearing in a gap of 20−40 μm away from the fixed bottom plate. The sample has volume fraction $\phi = 0.51$, the applied strain rate is $\dot{\gamma}_{\text{macro}} = 0.013$ s^{-1}, and the period is $T = 200$ s.

At this point, we have defined the key control parameters, which are measured from each experimental data set: the strain rate $\bar{\dot{\gamma}}_{\text{meso}}$ and the strain amplitude γ_{meso}. We next consider how these variables relate to the magnitude of the shear-induced particle motion.

4.3.2 Individual particle motions

Because of our large local strains (measured to be $\gamma_{\text{meso}} > 0.3$ for all cases), we observe significant particle motion, as shown Fig. 4.5 on page 37(a,b). In the laboratory reference frame, the microscopic velocity gradient is obvious either in the raw trajectories [Fig. 4.5 on page 37(a)] or in the large displacements [Fig. 4.5 on page 37(b)] measured between the beginning and end of the half period. However, in a sense, much of this motion is "trivial"; we wish to observe what nontrivial local rearrangements are caused by the strain. To do this, we consider the non-affine motion by remov-

ing averaged particle displacements at the same depth z from the real trajectories of particles [69, 73, 88, 68, 89],

$$\tilde{x}_i(t) = x_i(t) - \int_0^t \dot{\gamma}_{\text{meso}}(t')z_i(t')dt' \tag{4.3}$$

where the removed integral represents the shearing history of the particle i. To be clear, the shearing history is based on the average motion within the entire imaged region, and the remaining motion of particle i is caused by interactions with neighboring particles due to the shear. This motion is shown in Fig. 4.5 on the following page(c), showing the $\tilde{x}z$ plane rather than the xz plane; the particles move shorter distances. Their overall displacements in this "de-sheared" reference frame are shown in Fig. 4.5 on the next page(d). A few trajectories are up to 2 μm long, comparable to the particle diameter. These non-affine displacements shown in Fig. 4.5 on the following page(d) are much smaller than the raw displacements of Fig. 4.5 on the next page(b), but much larger than thermally activated Brownian motion, which takes more than 1000 s to diffuse over a 1 μm distance in our dense samples (comparable to the particle radius a). These non-affine motions $\tilde{x}$ reflect shear-induced plastic changes inside the structure.

To quantify the amount of this non-affine motion $\tilde{x}$, one could calculate the mean squared displacements (MSD) often defined as

$$\langle \Delta\tilde{x}^2 \rangle(\Delta t) = \langle (\tilde{x}_i(t + \Delta t) - \tilde{x}_i(t))^2 \rangle_{i,t} \tag{4.4}$$

where the angle brackets indicate an average over time t, as well as particles i. Thus this identity assumes that environmental conditions remain the same for all the time, since it does not depend on t. However, as shown by Fig. 4.4 on the preceding page, the shear rate $\dot{\gamma}_{\text{local}}(t)$ depends on the time. Therefore, we use an alternate

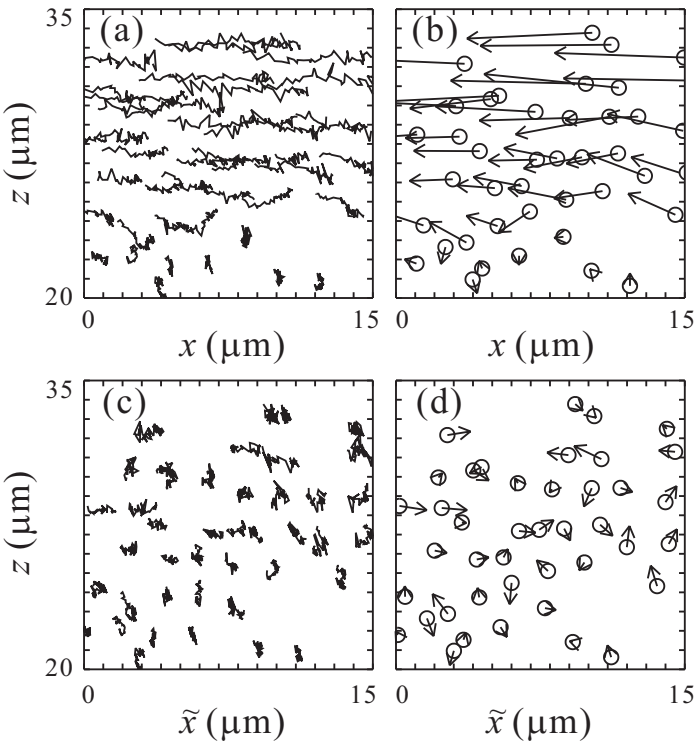

Figure 4.5: Trajectories of colloids in an xz slice (5 μm thick in the y direction), see Fig. 4.1 on page 29 for the coordinate axes. The sample has $\phi = 0.51$, and the data shown correspond to a locally measured accumulated strain $\gamma_{\rm meso} = 0.43$ over 45 s of data, so the effective strain rate is $\bar{\dot{\gamma}}_{\rm meso} = \gamma_{\rm meso}/\Delta t = 0.0096$ s^{-1}. (a) Trajectories in a reference frame co-moving with the average velocity $v_x(z = 20\ \mu{\rm m})$. (b) Displacements corresponding to data from panel (a), where the start point of each particle is marked with a circle and the end point is marked with an arrowhead. (c) The same data, but with the affine motion removed; this is the $\tilde{x}z$ plane. (d) Displacements corresponding to panel (c).

formulation

$$\langle \Delta\tilde{x}^2 \rangle(t) = \langle (\tilde{x}_i(t) - \tilde{x}_i(t=0))^2 \rangle_i \tag{4.5}$$

where the angle brackets only indicate an average over particles, and t is the time since the start of a half period of shear. Figure 4.6(a) shows mean squared displacement (MSD) of the non-affine motion $\Delta\tilde{r}^2 = \Delta\tilde{x}^2 + \Delta y^2 + \Delta z^2$ as a function of t for five different experiments with different strain rates $\bar{\dot{\gamma}}_{\text{meso}}$, from 0.02 to 0.006 s^{-1}. In each case the curves nearly reach a slope of 1 on the log-log plot, indicating that shear quickly facilitates particles' rearrangements. The magnitude of the motion is $\Delta\tilde{r}^2 \approx 1\ \mu\text{m}^2$, indicating that the original structure is mostly lost [90].

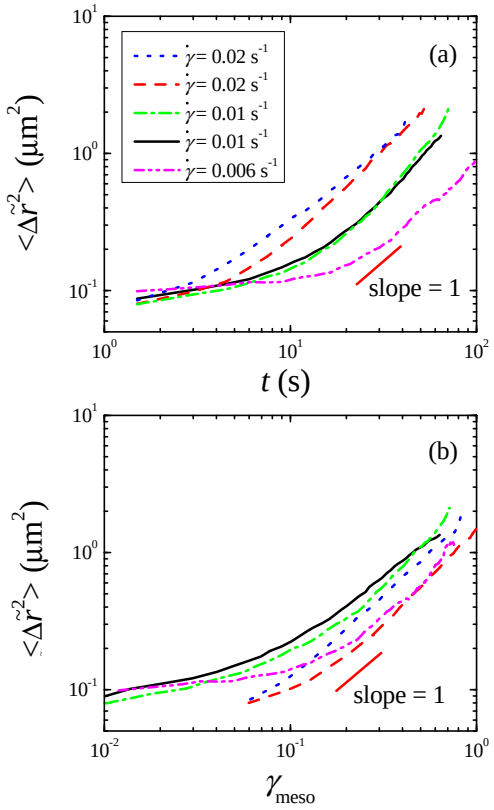

Figure 4.6: (Color online) (a) The mean square displacement of the non-affine motion $\Delta\tilde{r}$ as a function of the time t since the start of shear. (b) The same data plotted as a function of the accumulated strain $\gamma_{\text{meso}} = \int_0^t \dot{\gamma}_{\text{meso}}(t')dt'$. The five curves represents five data sets with the same volume fraction $\phi = 0.51$ but three different shear rates $\bar{\dot{\gamma}}_{\text{meso}}$ as indicated in the figure. The total accumulated strain is the final point reached by each curve in panel (b).

Figure 4.6 on the preceding page(a) also shows that $\Delta\tilde{r}^2$ is larger for faster strain rates at the same t. We find that this motion is determined by the accumulated strain, as shown in Fig. 4.6 on the previous page(b) by replotting the MSD as a function of γ_{meso} (Eqn. 4.1 on page 34). In this graph, the curves are grouped closer together and there is no obvious dependence on $\bar{\dot{\gamma}}_{\text{meso}}$.

It suggests that the accumulated strain is an important parameter in the structural relaxation, which was also found in previous work on shear transformation zones [91, 89], and is similar behavior to that seen for athermal sheared systems [92]. Additionally, Fig. 4.6 on the previous page(b) shows that the slopes of the curves are close to 1 when $\gamma_{\text{meso}} > 0.1$, confirming that the accumulated strain in our experiments is large enough to rearrange the original structure in a supercooled colloidal liquid. We stress that the rough agreement between the curves seen in Fig. 4.6 on the preceding page(b) is based on the locally measured applied strain, and not the macroscopically applied strain.

An earlier study of steady shear applied to colloidal glasses by Besseling et al. [69] found that the diffusion time scale τ scaled as $\dot{\gamma}^{-0.8}$, and simulations also found power law scaling [67, 68]. The collapse of our MSD curves [Fig. 4.6 on the previous page(b)] seems to imply $\tau \sim \dot{\gamma}^{-1.0}$. It is possible that the disagreement between these results is too slight to be clear over our limited range in $\dot{\gamma}$ (less than one decade). Also, we study supercooled fluids whereas Ref. [69] examines colloidal glasses. Furthermore, our maximum local strain is $\gamma_{\text{meso}} = 1.6$, while Ref. [69] considers steady strain up to a total accumulated strain of 10. Another recent study of sheared colloidal glasses [93] implies a result similar to ours, $\tau \sim \dot{\gamma}^{-1.0}$, but did not discuss the apparent difference with Ref. [69].

To better understand the mean square displacement curves (Fig. 4.6 on the preceding page), we wish to examine the data being averaged to make these curves. We do so by plotting the distributions of displacements $\Delta\tilde{r}$ in Fig. 4.7 on page 41. To

better compare the shapes of these distributions, we normalize these displacements by the strain and thus plot $P(\Delta s)$ where $\Delta s \equiv \Delta\tilde{r}/(\gamma_{\text{meso}}^{0.5})$; this normalization is motivated by the observation that at large γ_{meso}, we have $\langle\Delta\tilde{r}^2\rangle \sim \gamma_{\text{meso}}$ (Fig. 4.6 on page 38) [89]. Furthermore, we normalize $P(\Delta s)$ so that the integral over all vectors $\Delta\vec{s}$ is equal to 1, similar to Ref. [89]. Figure 4.7 on the next page shows that the distributions corresponding to small strains are much broader than those corresponding to large strains. For the smallest strain, the distribution has a large exponential tail over 3 orders of magnitude. For larger strains ($\gamma_{\text{meso}} > 0.1$), the curves are no longer exponential and the tails are shorter, indicating fewer extreme events. These curves appear more like Gaussian distributions. At the larger strain values ($\gamma_{\text{meso}} > 0.1$), the distributions collapse; this is the same strain regime for which the mean square displacement becomes linear with γ_{meso} [Fig. 4.6 on page 38(b)]. As the Ref. [89] suggests, the exponential tail for small strains is similar to what has been seen for individual plastic events [94, 88], while the distributions for larger strains are consistent with successive temporally uncorrelated plastic events drawn from the exponential distribution. However, it is possible that these events are spatially correlated, which will be seen below.

The mean square displacement data we have shown (Fig. 4.6 on page 38) treats all three directions equivalently, with the exception that the x displacements have had their nonaffine motions removed. However, the three directions are not equivalent physically: the x direction corresponds to the shear-induced velocity, the y direction is the vorticity direction, and z is the velocity gradient direction. To look for differences in motion between these three directions, we plot the probability distribution of the displacements $[\Delta\tilde{x}, \Delta y, \Delta z]$, in Fig. 4.8 on page 42. The three distributions agree with each other, and in fact are symmetric around the origin. This suggests that the shear-induced motions are isotropic. Furthermore, they are well-fit by a Gaussian, suggesting that the shear-induced motion liquefies the sample (at least at the large

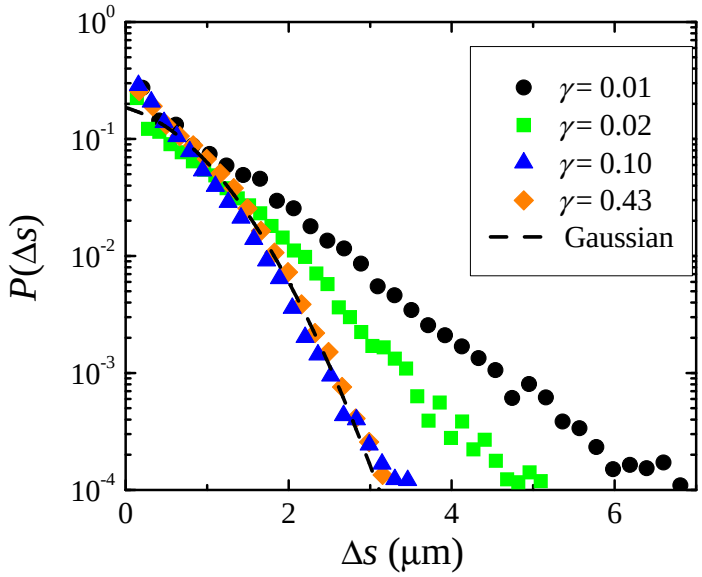

Figure 4.7: (Color online) Probability distribution function of $\Delta s = \Delta\tilde{r}/\gamma_{\rm meso}^{0.5}$, the nonaffine displacement $\Delta\tilde{r}$ scaled by the local strain $\gamma_{\rm meso}^{0.5}$. The data shown are from one experimental run, using portions of the data corresponding to strain increments $\gamma_{\rm meso} = 0.01$, 0.02, 0.10, and 0.43. These correspond to time intervals $\Delta t = 1.5$, 4.5, 16.5, and 45 s. $P(\Delta s)$ is normalized so that the integral over all vectors $\Delta\vec{s}$ is equal to 1, similar to Ref. [89]. For small strains, the curves have large exponential tails, and for larger strain, the tails become smaller and appear more Gaussian. The dashed line is Gaussian fit for $\gamma_{\rm meso} = 0.43$. For this sample, the data and parameters are the same as Fig. 4.5 on page 37.

γ_{meso} considered for Fig. 4.8). This seems natural in the context of jamming, where adding more strain moves the sample farther from the jammed state [2]. Of course, in our raw data the Δx data show a significant bias in the direction of the shear-induced velocity; but it is striking that the non-affine displacements $\Delta\tilde{x}$ show no difference from the displacements in y and z, as also found in sheared colloidal glass [69, 68].

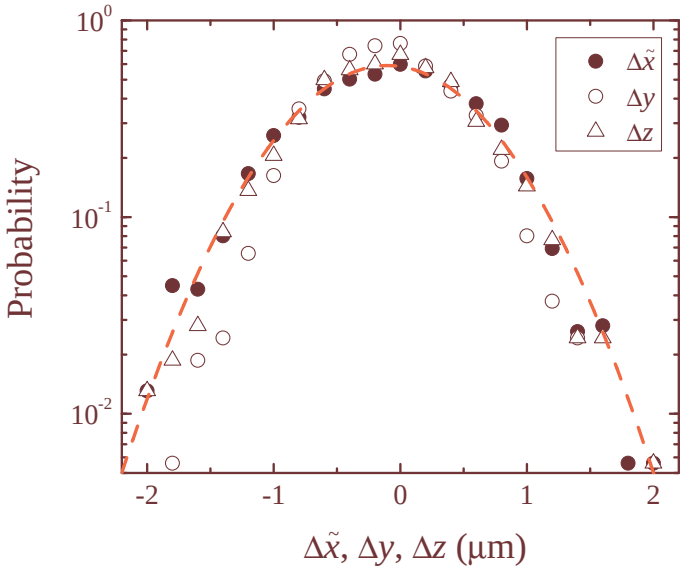

Figure 4.8: (Color online) Probability distribution functions for non-affine motions in each direction, $\Delta\tilde{x}$ (filled cycle), Δy (hollow circle) and Δz (hollow triangle). The mean of $\Delta\tilde{x}$, Δy and Δz are 0 μm, and the standard deviations are 0.67, 0.53, and 0.62 μm. The red curve is a Gaussian fit to the $\Delta\tilde{x}$ data. For this sample, the parameters are the same as Fig. 4.5 on page 37 ($\phi = 0.51$, $\gamma_{\text{meso}} = 0.43$, $\bar{\dot{\gamma}}_{\text{meso}} = 0.0096$ s^{-1}, $\Delta t = 45$ s).

Thus far, we have established that shear-induced particle displacements are closely tied to the total applied strain γ_{meso} [Fig. 4.6 on page 38(b)]. We then introduced the nonaffine motion $\Delta\tilde{r}$ which we find to be isotropic, on the particle scale: individual particles are equally likely to have shear-induced displacements in any direction (Fig. 4.8). While the distributions of displacements are isotropic, this does not imply that displacements are uncorrelated spatially. To check for this, we calculate two

displacement correlation functions as defined in Ref. [95, 96, 97] :

$$S_{\vec{r}}(R,\Delta t) = \frac{\langle \Delta\vec{\tilde{r}}_i \cdot \Delta\vec{\tilde{r}}_j \rangle}{\langle \Delta\tilde{r}^2 \rangle}, \tag{4.6}$$

$$S_{\delta r}(R,\Delta t) = \frac{\langle \delta\tilde{r}_i \delta\tilde{r}_j \rangle}{\langle (\delta\tilde{r})^2 \rangle}, \tag{4.7}$$

where the angle brackets indicate an average over all particles; see Refs. [95, 97] for more details. The mobility is defined as $\delta\tilde{r} = |\Delta\tilde{r}| - \langle|\Delta\tilde{r}|\rangle$, in other words, the deviation of the magnitude of the displacement from the average magnitude of all particle displacements. The correlation functions are computed for the nonaffine displacements, using $\Delta t = 45$ s to maximize the "signal" (nonaffine displacements) compared to the "noise" (Brownian motion within cages, on a shorter time scale).

The two correlation functions are shown in Fig. 4.9 on the following page for a representative data set. These functions are large at short separations R and decay for larger R, suggesting that neighboring particles are correlated in their motion. In particular, the vector-based correlation $S_{\vec{r}}$ has a large magnitude at small R, showing neighboring particles have strongly correlated directions of motion, even given that we are only considering the nonaffine displacements. The two correlation functions decay somewhat exponentially, as indicated by the straight line fits shown in Fig. 4.9 on the next page, with decay constants $\xi_{\vec{r}} = 6.4$ μm$= 6.1a$ and $\xi_{\delta r} = 2.5$ μm$= 2.4a$ (in terms of the particle radius a). The larger the slope, the more localized the correlation is. $\xi_{\vec{r}}$ is similar to that found previously for supercooled colloidal liquids, and $\xi_{\delta r}$ is slightly shorter than the prior results [95]. Overall, these results confirm that the shear-induced particle motion is spatially heterogeneous, quite similar to what has been seen in unsheared dense liquids [98, 12, 13, 95, 14, 15, 97] and granular materials [99, 100]. The length scale may be equivalent to the correlation length scale for fluidity discussed in Refs. [65, 66]. For example, an experimental study of sheared polydisperse emulsions found a fluidity length scale comparable to 1-2 droplet

diameters near the glass transition [65].

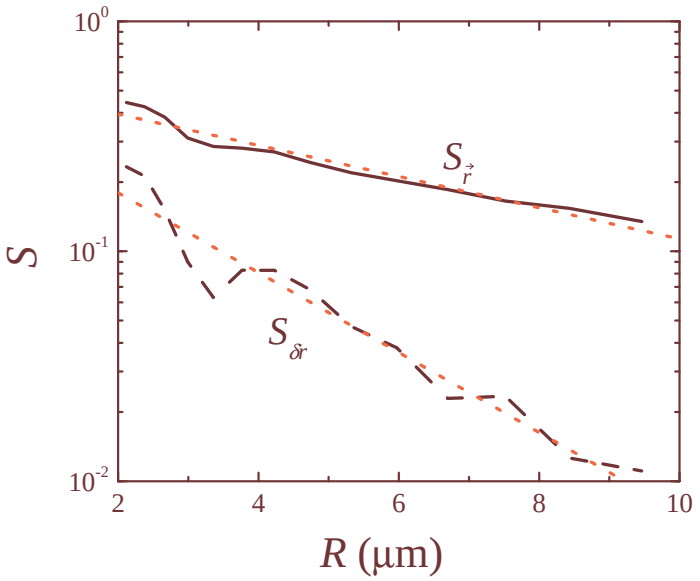

Figure 4.9: (Color online) Spatial correlation functions $S_{\vec{r}}$ and $S_{\delta r}$ characterizing particle motion. The data are the same as Fig. 4.5 on page 37 ($\phi = 0.51$, $\gamma_{\rm meso} = 0.43$ over 45 s of data, and $\bar{\dot{\gamma}}_{\rm meso} = \gamma_{\rm meso}/\Delta t = 0.0096$ s^{-1}). The solid and dashed lines correspond to $S_{\vec{r}}$ and $S_{\delta r}$ averaged over all the particles in the sample. The dotted lines (red) correspond to exponential fits with length scales $\xi_{\vec{r}} = 6.4$ μm and $\xi_{\delta r} = 2.5$ μm.

Considering all of our data sets, we do not find a strong dependence on either the strain rate $\dot{\gamma}$ or the total strain γ for the ranges we consider ($\bar{\dot{\gamma}}_{\rm meso} = 0.006 - 0.02$ s^{-1}, $\gamma_{\rm meso} = 0.3 - 1.6$). We do not have a large amount of data with which to calculate the correlation functions; unlike prior work, we cannot do a time average [95]. If we use an exponential function to fit our different data (different strains, strain rates, and volume fractions), the mobility correlation $S_{\delta r}$ yields a length scale $\xi_{\delta r} \approx 1.8 - 3.9$ μm and the vector correlation $S_{\vec{r}}$ yields a length scale $\xi_{\vec{r}} \approx 3.2 - 7.5$ μm. To check this, we also calculate

$$\xi' = \frac{\langle R \cdot S(R) \rangle}{\langle S(R) \rangle} \tag{4.8}$$

where the angle brackets indicate averages over R; for a perfect exponential, we would have $\xi' = \xi$. Using this method, we find more consistent length scales of $\xi'_{\delta r} \approx (3.0 - 4.0)a$ and $\xi'_{\vec{r}} \approx (3.5 - 4.3)a$. Our data do not suggest any dependence

of these length scales on the control parameters over the range we investigate. Of course, as $\dot{\gamma} \to 0$, we would expect to recover the original unstrained sample behavior [67]. Similar samples in this volume fraction range were previously found to have length scales with similar values, $\xi_{\delta r} \approx 4a - 8a$ and $\xi_{\vec{r}} \approx 6a$ [95]. However, the time scales for this motion are much longer than that for our sheared samples.

4.3.3 Defining local plastic deformation

We wish to look for spatially heterogeneous dynamics, that is, how the shear-induced motion takes place locally and how particles cooperate in their motion. Several prior groups have examined local rearrangements in simulations and experiments [8, 74, 9, 65], but have used differing ways to quantify the motion. We will discuss those quantities together, and compare them using our data. We have two goals: first, to understand how different measures of local rearrangements reveal different aspects of the motion; and second, to see if the spatial structure of rearranging groups of particles exhibits any particular orientation with respect to the shear direction.

For all of these definitions of rearranging groups of particles, it is useful to define a particle's nearest neighbors. Our definition of a particle's nearest neighbors are those particles within the cutoff distance r_0, set by the first minimum of the pair correlation function $g(r)$.

We start by quantifying the local strain seen by an individual particle, which is based on the average motion of its neighbors. For a particle i with center at $\vec{r}_i(t)$, the relative positions of its neighbors j are $\vec{d}_{ij}(t) = \vec{r}_j(t) - \vec{r}_i(t)$. These neighboring particles move, and their motions over the next interval Δt are given by $\Delta\vec{d}_{ij}(t) = \vec{d}_{ij}(t + \Delta t) - \vec{d}_{ij}(t)$, as shown in Fig. 4.10 on the following page.

The strain tensor $\mathbb{E}_i$ for this region around particle i is then determined by minimizing the mean squared difference between the actual relative motions $\Delta\vec{d}_{ij}(t)$ and

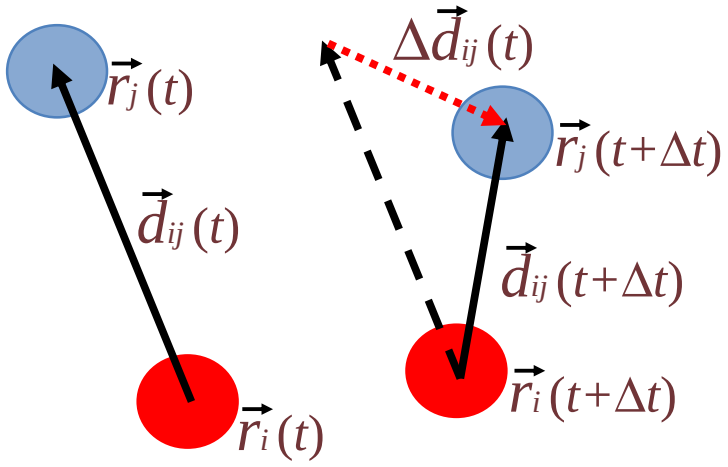

Figure 4.10: (Color online) Sketch illustrating the definition of the motion of the relative position vector $\Delta\vec{d}_{ij}$ of two neighboring particles, red and blue (dark and light gray). $\vec{r}_i(t)$ represents the position of particle i at time t, $\vec{d}_{ij}(t)$ is the relative position between particles i and j at time t, and $\Delta\vec{d}_{ij}(t)$ is how the vector $\vec{d}_{ij}$ changes over the time interval $(t, t+\Delta t)$.

that predicted by $\mathbb{E}_i$, in other words, choosing $\mathbb{E}_i$ to minimize

$$D^2_{i,\min} = \min\left[\Sigma_j \left[\Delta\vec{d}_{ij}(t) - \mathbb{E}_i\vec{d}_{ij}(t)\right]^2\right]. \tag{4.9}$$

The error, $D^2_{i,\min}$, quantifies the plastic deformation of the neighborhood around particle i, after removing the averaged linear response $\mathbb{E}_i\vec{d}_{ij}(t)$ [8]. Thus, $D^2_{i,\min}$ is one way to quantify the local nonaffine rearrangement, "local" in the sense of an individual particle i and its neighbors. We term $D^2_{i,\min}$ the "plastic deformation." Note that the sum is computed over the ten nearest particles j to particle i, otherwise the value of $D^2_{i,\min}$ would depend on the number of neighbors. In practice, most of these neighboring particles are within 3.0 μm of particle i, which is comparable to the first minimum of the pair correlation function $g(r)$, which motivates our choice of ten neighbors.

Of course, quite often $\mathbb{E}_i$ is different from the overall strain over the imaged volume, which in turn is different from the macroscopically applied strain. In practice, given that the shear is applied in x direction with the velocity gradient along z, we only

treat the xz components of Eqn. 4.9 on the previous page; that is, $\vec{d}_{ij}$ and $\mathbb{E}_{ij}$ can be written as :

$$\vec{d}_{ij} = \begin{bmatrix} x_{ij} \\ \\ z_{ij} \end{bmatrix}, \mathbb{E}_i = \begin{bmatrix} \epsilon_i^{xx} & \epsilon_i^{xz} \\ \\ \epsilon_i^{zx} & \epsilon_i^{zz} \end{bmatrix}. \tag{4.10}$$

To better understand this local strain tensor $\mathbb{E}_i$, we follow the method of Ref. [9, 8]. If the particle-scale local strain was identical to the imposed strain, we would expect $\epsilon_i^{xz} = \gamma_{\text{meso}}$ and the other matrix elements to be zero. We find that these expectations are true on average (for example $\langle \epsilon_i^{xz} \rangle = \gamma_{\text{meso}}$) but that for individual particles their local environment can be quite different. For each experiment, the distributions of all four matrix elements have similar standard deviations, and examining different experiments the standard deviations are between 24% - 39% of γ_{meso}.

To quantify the measured particle-scale strain, we define the "local strain"

$$\gamma_{i,\text{micro}} = \epsilon_i^{xz} + \epsilon_i^{zx} \tag{4.11}$$

(using the definition of the strain tensor which is related to $\mathbb{E}$ [101]). That is, this quantity is a local approximation to the strain $(\frac{\partial u_x}{\partial z} + \frac{\partial u_z}{\partial x})$. The local strain $\gamma_{i,\text{micro}}$ is now a second way to quantify the local rearrangement of the neighborhood around particle i, in addition to $D^2_{i,\text{min}}$. The diagonal elements, ϵ_i^{xx} and ϵ_i^{zz}, relate to the dilation of the local environment. In particular, the local environment stretches by a factor of $(1 + \epsilon_i^{xx})$ in the x direction and likewise $(1 + \epsilon_i^{zz})$ in the z direction. If these matrix elements are zero, then the local environment remains the same; positive matrix elements correspond to expansion and negative matrix elements correspond to contraction. We define the overall dilation as $\delta e_i = (1 + \epsilon_i^{xx})(1 + \epsilon_i^{zz}) - 1$, which is a third way to quantify the local rearrangement around particle i.

A fourth way to consider local particle motion is the previously defined nonaffine displacement, $\Delta\tilde{r}^2$. The key difference is that D^2_{min}, γ_{micro}, and δe all are derived

from the actual particle motion Δr, whereas $\Delta\tilde{r}^2$ removes the motion caused by γ_{meso} (through Eqn. 7.10 on page 84).

To demonstrate how neighboring particles rearrange and result in larger values of these various parameters, Fig. 4.11 on page 50 shows an example using real trajectories. The original positions of the particles are shown, along with displacement vectors indicating where they move after the sample is strained with $\gamma_{\text{meso}} = 0.58$. The overall strain is seen in that particles near the top move farther than those at the bottom; however, the red (dark) particle in the middle has an unusual motion, moving downward in the $-z$ direction. Figure 4.11 on page 50(b) shows the motion of the surrounding particles, as seen in the reference frame attached to the red (dark) particle. It is these displacements that are used in the calculation Eqn. 4.10 on the previous page. Figure 4.11 on page 50(c) shows the predicted final positions of the particles (drawn large) based on $\mathbb{E}_i$, as compared to the actual final positions (drawn small); the red (dark) particle is considered "particle i". This local region experiences both shear and a strong dilation in the z direction, both captured by $\mathbb{E}_i$. The differences between the predicted and actual final positions result in a moderately large value of $D^2_{\text{min}} = 56\ \mu\text{m}^2$. In particular, note that D^2_{min} is defined based on vectors pointing from the red (dark) reference particle to the other particles, and because the red particle moves downward, the vectors are all greatly stretched and this increases D^2_{min}. Finally, Fig. 4.11 on page 50(d) shows the positions of the same particles after the strain has been applied, where now the box represents the mesoscopic strain $\gamma_{\text{meso}} = 0.58$. The large spheres represent the expected positions if the motion was affine, and the small spheres show the actual positions. Differences between the expected and actual positions result in large values of the nonaffine displacement $\Delta\tilde{r}$. For the red (dark) particle, $\Delta\tilde{r} = 2.97\ \mu\text{m}$. Overall, the anomalous motion of the central particle i is because under the large local strain, this particle makes a large jump out of its original cage. It is these sorts of unusual motions that result in large

plastic deformations within the sample.

4.3.4 Collective particle motions

To investigate the relationships between these quantities, a 3 μm-thin y slice of a sample with volume fraction $\phi = 0.51$ is shown in several ways in Fig. 4.12 on page 51. In panel (a), the x displacement is shown, making the strain apparent. Panel (b) shows the original Voronoi volumes for each particle at $t = 0$. The Voronoi cell for each particle is defined as the volume closer to the center of that particle than to any other particle. In subsequent panels, the darker colors indicate larger local rearrangements, as measured by the non-affine displacement $\Delta\tilde{r}^2$ [panel (c)], plastic deformation $D^2_{\rm min}$ [panel (d)], local strain $\gamma_{\rm micro}$ [panel (e)], and dilation δe [panel (f)]. It can be seen that the darker colored particles cluster together, indicating that for each of these measures of local rearrangement, the motions are spatially heterogeneous [9]. This is a real-space picture showing conceptually what is indicated by the correlation functions in Fig. 4.9 on page 44, that neighboring particles have similar motions. These pictures are qualitatively similar to those seen for thermally-induced cage rearrangements in supercooled liquids [14, 13, 12, 102, 103] and glasses [104, 105, 106, 100, 107]. Furthermore, by comparing these images, it is apparent that particles often have large values of several quantities simultaneously; in particular compare panels (c) and (d), and panels (e) and (f). While the correspondence is not exact, it suggests that all four of these ideas are capturing similar features of rearranging regions. However, it is also clear that there are differences between (c) and (d) as compared to (e) and (f). In the latter two panels, the region of high activity is spread out over a larger area; more of the particles are deforming by these measures at the same time. Nonetheless, in all four cases, the particles around $x \approx 2 - 4$ μm are experiencing the most extreme deformations.

The Voronoi volume [Fig. 4.12 on page 51(b)] has previously been found to be

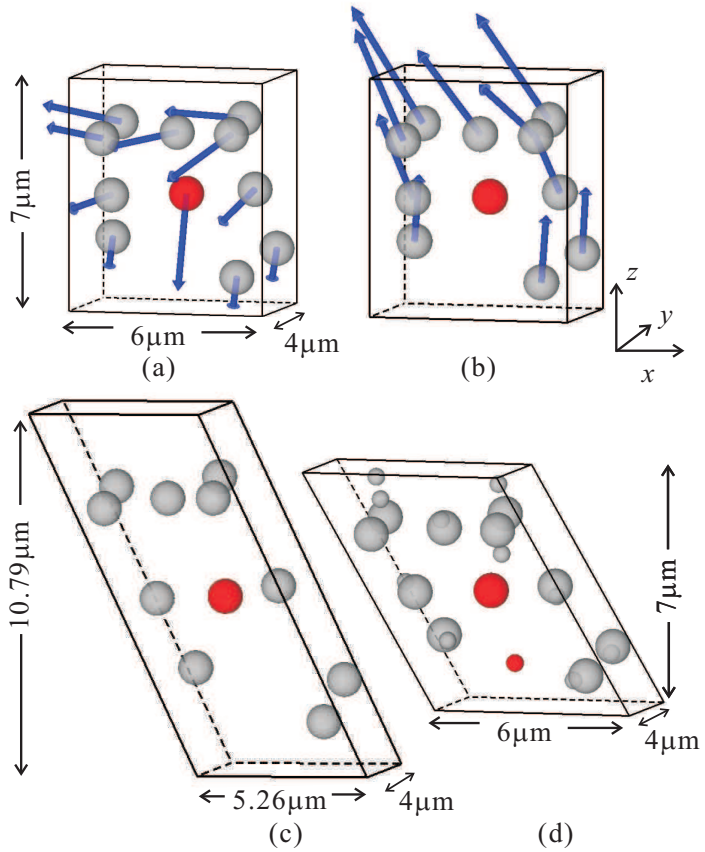

Figure 4.11: (Color online.) These four sketches show different portrayals of a particle with unusual motion. (a) Particle motion as seen in the laboratory reference frame. The arrows indicate displacement vectors. (b) Similar to (a) except the motion are in the reference frame where the central red (darker) particle is motionless. (c) The large spheres correspond to the expected positions of the particles, and the smaller spheres correspond to the actual positions of the particles. The distortion of the box and the expected positions of the particles are calculated based on the measured local strain tensor $\mathbb{E}_i$, where the red (darker) particle is particle i. For this local neighborhood, we have $\gamma_{\text{micro}} = 0.73$ and a dilation primarily in the z direction ($\epsilon^{xx} = -0.1, \epsilon^{zz} = 0.5$, and $\delta e = 0.35$). (d) The positions of the same particles after the strain has been applied, where now the box represents the mesoscopic strain $\gamma_{\text{meso}} = 0.58$. The large spheres represent the expected positions if the motion was affine, and the small spheres show the actual positions. For all panels, to show the displacements in three dimensions better, the radii of the large spheres are 0.5 of the real scale. The data correspond to a sample with $\phi = 0.51$, $\gamma_{\text{meso}} = 0.58$, $\bar{\dot{\gamma}}_{\text{meso}} = 0.014\ \text{s}^{-1}$, and $\Delta t = 40$ s.

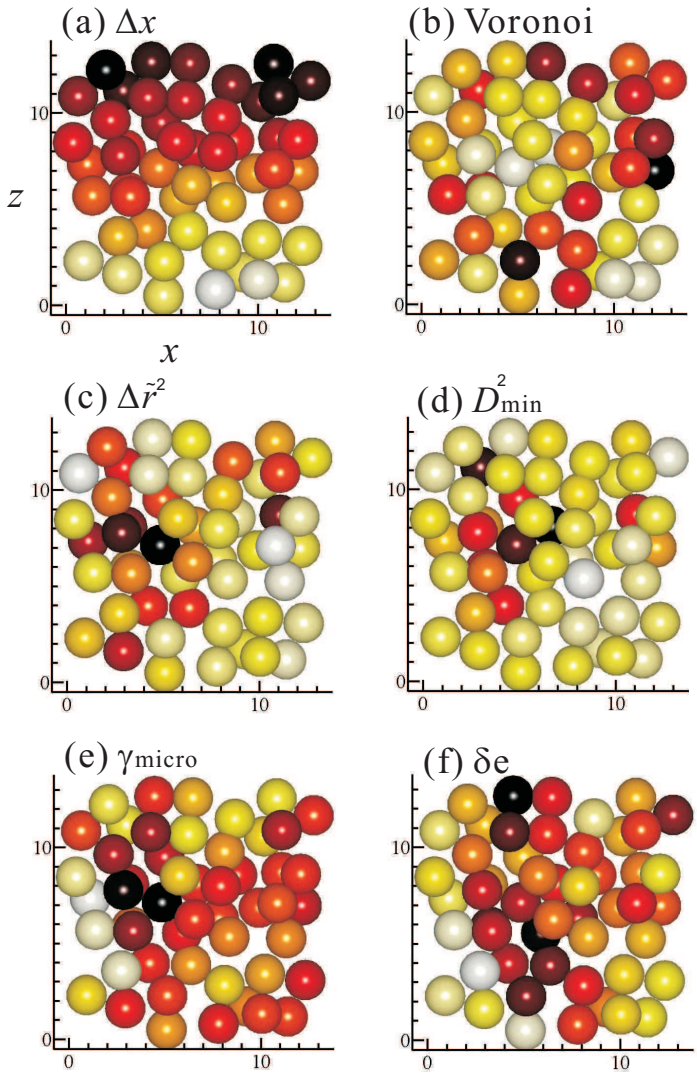

Figure 4.12: A 3 μm thin cut through the sample, showing the xz shear plane; the axes are as labeled in (a). The particles are drawn in their location at $t = 0$, the start of this strain half-cycle. (a) Darker particles have larger values of Δx, thus indicating the applied strain. The top particles (large z) are moving left (dark colors) and the bottom particles are moving right (light colors). (b) Darker particles have larger Voronoi volumes at $t = 0$. (c) Darker particles have larger values of the non-affine motion $\Delta\tilde{r}^2$. (d) Darker particles have larger values of the plastic deformation D^2_{min}. (e) Darker particles have larger values of the local strain γ_{micro}. (f) Darker particles have larger values of the dilation δe. The sample is the same as the data shown in Fig. 4.5 on page 37; see that figure caption for details.

slightly correlated with particle motion in unsheared colloidal supercooled liquids [90, 108]; that is, particles with large Voronoi volumes have more space to move and thus are likely to have larger displacements than average. Here it appears that there is no correlation between the Voronoi volume and the particle motion, suggesting that for these strained samples the local volume is not a crucial influence on the motion [68]. This is probably because in the end, all cages must rearrange for the strain to occur.

To demonstrate the relationships between the measures of plastic deformation more quantitatively, we compute 2D histograms comparing pairs of the variables, shown in Fig. 4.13 on page 54. The darker color indicates larger joint probability, and the dotted line represents the mean value of the quantity on the vertical axis corresponding to the quantity on the horizontal axis. Figure 4.13 on page 54(a) shows that on average, particles with a large plastic deformation D^2_{min} are also much likelier to have a large nonaffine displacement $\Delta\tilde{r}^2$. This is suggested by the specific example shown in Fig. 4.11 on page 50(c,d). Similarly, Fig. 4.13 on page 54(b) shows that a particle's microscopic strain γ_{micro} is well correlated with the dilation δe. For these data, the mesoscopic strain is $\gamma_{\text{meso}} = 0.43$; particles with $\gamma_{\text{micro}} < \gamma_{\text{meso}}$ are more often in local environments that contract ($\delta e < 0$), and vice-versa. As a contrast, Fig. 4.13 on page 54(c) shows a somewhat weaker correlation between D^2_{min} and γ_{micro}. The Pearson correlation coefficients between these quantities are $C(D^2_{\text{min}}, \Delta\tilde{r}^2) = 0.43 \pm 0.11$, $C(\gamma_{\text{micro}}, \delta e) = 0.42 \pm 0.09$, and $C(\gamma_{\text{micro}}, D^2_{\text{min}}) = 0.17 \pm 0.05$. The uncertainties are from the standard deviations of the correlation coefficients from the nine different experiments we conducted.

Overall, Fig. 4.13 on page 54 suggests that D^2_{min} and $\Delta\tilde{r}^2$ both capture the idea of plastic deformation [88]. The correspondence between these two variables is non-trivial, given that $\Delta\tilde{r}^2$ is based on trajectories with the overall strain removed (the strain computed from all observed particles), whereas D^2_{min} only accounts for the very

localized strain of the neighboring particles. In contrast, γ_{micro} and δe are well-suited to examine particles moving in atypical ways; typical particles have $\gamma_{\text{micro}} \approx \gamma_{\text{meso}}$ and $\delta e = 0$. These two separate ideas (plastic deformation and atypicality) are only weakly correlated. Other than the three specific comparisons shown in Fig. 4.13 on the next page, all other comparisons are even less correlated ($|C| < 0.1$). We also examined the quantities $|\gamma_{\text{micro}} - \gamma_{\text{meso}}|$ and $|\delta e|$ as ways to measure the deviations from typical behavior; these quantities are also only weakly correlated to the other measures of deformation.

We now return to the question of the isotropy of the motion. Figure 4.8 on page 42 indicates that the distribution of all particle motions is isotropic, but it is possible that the spatially heterogeneous groups of highly mobile particles shown in Fig. 4.12 on page 51 are themselves oriented along a preferred direction. To investigate the 3D structures of these relaxation regions, we quantify the sizes of these active regions in the x, y and z directions. To start, we define connected neighboring particles as those with separations less than r_0, the distance where pair correlation function $g(r)$ reaches its first minimum. (Note that this is slightly different from the neighbor definition used for Eqn. 4.9 on page 46; see the discussion following that equation.) For a given quantity, we consider active particles as those in the top 20% of that quantity, similar to prior work [12, 13, 104, 67]. We then define the active region as a cluster of connected active particles. For example, Fig. 4.14 on page 55 shows a cluster of particles with large non-affine displacements [panel (a)] and a cluster with large plastic deformations [panel (b)]. Each cluster is drawn from the same data set, and the particles drawn in red (darker) are common to both clusters. (Note that clusters drawn based on γ_{micro} and δe are smaller. In Fig. 4.12 on page 51(e,f), more regions have large values of these parameters, but the top 20% most active are not clustered to the extent they are in Fig. 4.12 on page 51(c,d).)

We wish to understand if the shapes of such clusters show a bias along any par-

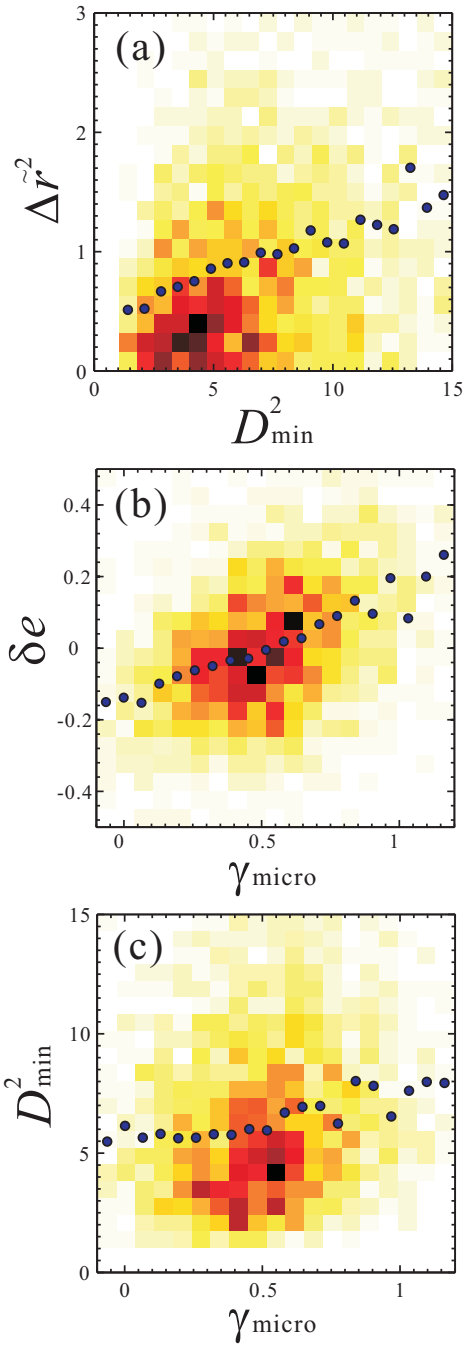

Figure 4.13: (Color online) 2D histograms of (a) $D^2_{\rm min}$ and $\Delta\tilde{r}^2$, (b) $\gamma_{\rm micro}$ vs. dilation δe and (c) $\gamma_{\rm micro}$ and $D^2_{\rm min}$. The sample has the same parameters as Fig. 4.5 on page 37; see that caption for details. In these histograms, darker colors stand for the larger probability. The dotted lines are the average values of the y axis corresponding to each value on the x axis. The correlation coefficients between each pair of variables are (a) $C = 0.43 \pm 0.11$, (b) $C = 0.42 \pm 0.09$, and (c) $C = 0.17 \pm 0.05$; see text for details.

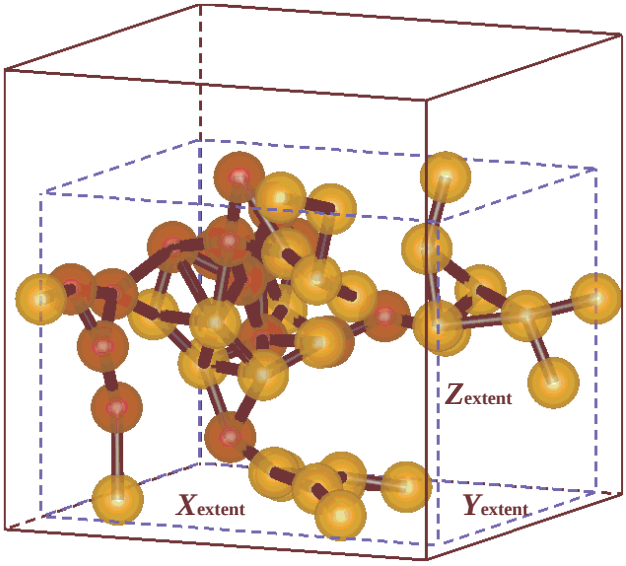

(a) $\Delta\tilde{r}^2$ cluster

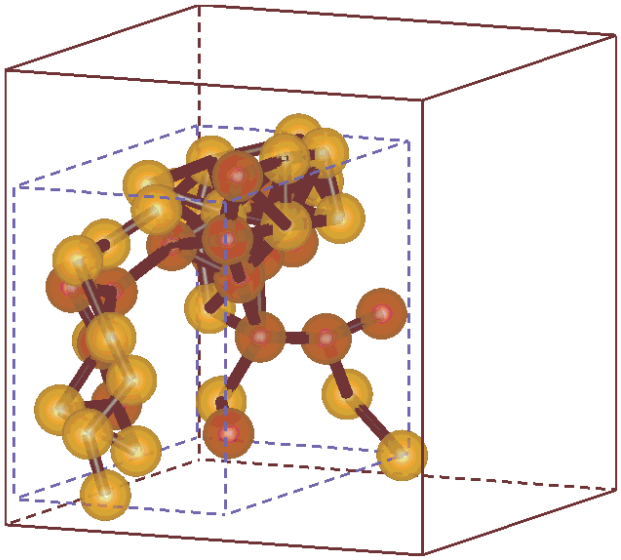

(b) D^2_{min} cluster

Figure 4.14: (Color online.) A cluster of neighboring particles with large values of (a) non-affine motion $\Delta\tilde{r}^2$ and (b) plastic deformation D^2_{min}. To avoid biasing the cluster shape, the particles are drawn from within a 15×15×15 μm^3 cube (solid lines). The dashed lines indicate the spatial extent of the two cluster shapes in each direction. The cluster in (a) is $14 \times 12 \times 11$ μm^3 and the cluster in (b) is $8 \times 14 \times 10$ μm^3. The red particles are common between the two clusters, and the black bonds indicate neighboring particles; particle sizes are drawn 0.8 times the actual scale, to make the connections more visible. In each case, the particles shown are the top 20% for the parameter chosen. The data corresponds to the same parameters as in Fig. 4.5 on page 37; see that caption for details.

ticular direction. It is important that the experimental observation volume not bias the result, so from within the observed 3D volume we consider only particles that start within an isotropic cube of dimensions $15\times15\times15$ μm^3. The size of this cube is chosen to be the largest cube for which all the particles are within the optical field of view for the full half-cycle of shear for all experiments. (See the related discussion at the end of Sec. 4.2 on page 29.) Within this isotropic volume, we consider the largest cluster from each experiment and for each considered variable. We then define the extent of that cluster in each direction from the positions of each particle within the cluster as $x_{\text{extent}} = \max(x_i) - \min(x_i)$ and similarly for y and z.

Anisotropic cluster shapes would be manifested by systematic differences in the relative magnitudes of x_{extent}, y_{extent}, and z_{extent}. We compare these in Fig. 4.15 on the next page for clusters of particles with large non-affine motion $\Delta\tilde{r}^2$ [panel (a)] and large plastic deformation D^2_{min} [panel (b)]. The comparison is made by using the ratios $y_{\text{extent}}/x_{\text{extent}}$ and $z_{\text{extent}}/x_{\text{extent}}$, thus normalizing the extent in the y and z directions by that of the shear velocity direction x. Thus, if a cluster has the same extent in x and y, $y_{\text{extent}}/x_{\text{extent}}$ should be equal to 1, along the vertical dashed line. Similarly, for the same extent in x and z, points should be along the horizontal dashed line with $z_{\text{extent}}/x_{\text{extent}} = 1$. If the extent is the same for y and z, the points should be along the diagonal line with $y_{\text{extent}}/x_{\text{extent}} = z_{\text{extent}}/x_{\text{extent}}$. For an isotropic cluster with same size in all dimensions, the point should be in the center (1,1).

As shown in Fig. 4.15 on the following page, for all of our data, we find no systematic anisotropy; the cluster extent ratios are mostly clustered around the isotropic point (1,1). Due to random fluctuations, no cluster is perfectly isotropic, yet the points seem fairly evenly distributed around the three dashed lines. Thus, while the shear-induced rearrangements take place in localized regions (Fig. 4.12 on page 51), the data indicate that these regions on average have no directional bias. This seems true for both the nonaffine displacements $\Delta\tilde{r}^2$ in Fig. 4.15 on the following page(a)

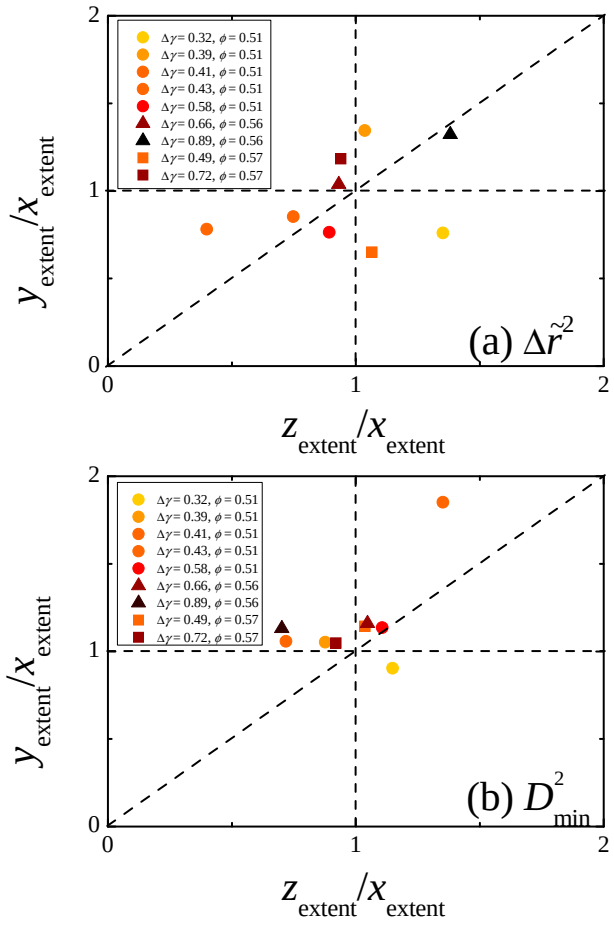

Figure 4.15: Comparison between the cluster extent in x, y and z, based on different variables. (a) Particles with the largest non-affine motion $\Delta\tilde{r}$. (b) Particles with the largest plastic deformation D^2_{min}. The symbols represent different volume fractions: $\phi = 0.51$ (circles), 0.56 (triangles) and 0.57 (squares). Colors (or grays from light to dark) represent different accumulative strains $\gamma_{\text{meso}} = 0.3 - 0.9$. The clusters are comprised of the top 20% of the particles with the given characteristic.

and the plastic deformation $D^2_{\min}$ in Fig. 4.15 on the previous page(b).

4.4 Discussion

We examined the microscopic plastic deformations occurring in several sheared dense colloidal suspensions. Our first main observation is that on average, individual particles have no bias in their direction of motion, other than that trivially imposed by the strain. When this imposed motion is removed from the particle trajectories, the remaining shear-induced motion is isotropic: particles are equally likely to move in any direction. Our second main observation is on the shape of groups of particles undergoing plastic rearrangements. There are several ways to determine which particles are rearranging, and we have shown that all of these are useful for highlighting local regions of deformation. Furthermore, the shapes of these regions are also isotropic. However, we cannot rule out that with more data and subtler analysis, we might find anisotropies in particle motion [109]. In this 2D simulation [109], the shear time is 10 times longer than the relaxation time. While in my 3D colloidal experiment, the shear time is around the relaxation time. Therefore, if shear strain is much larger, we might see anisotropic shape in rearranging regions.

In our results, we find little dependence on the overall volume fraction ϕ, total strain, or strain rate. For the volume fraction, all of our samples are dense liquids with $\phi < \phi_G$. At significantly lower volume fractions, presumably particles would not be caged and the shear-induced rearrangements might be quite different [92]. At higher volume fractions $\phi > \phi_G$, prior work has seen similar results [69, 9] although not examined the shapes of the rearranging regions in detail. It is possible that results in glassy samples might be different, given that near ϕ_G slight changes in volume fraction have large consequences [72], but we have not seen clear evidence of that in our data. For the total strain, we have not examined a wide range of parameters.

In all cases, we are studying sufficiently large enough strains to induce irreversible, plastic rearrangements.For the strain rates, all of our strain rates are fast enough such that the modified Peclet number $Pe^{\star}$ is at least 7, so that thermally induced diffusive motion is less relevant. It is likely that at slower strain rates (lower Peclet numbers), different behavior would be seen [67].

Previous work [110, 111, 112, 76] found that oscillatory shear can induce crystallization of concentrated colloidal suspensions. The 'induction time' of this crystallization is strain dependent: a larger strain amplitude results in shorter induction time. In our experiments, we studied only a limited number of oscillations, and our strain amplitude $\sim$1. We did not observe crystallization in any of our experiments. It is likely that were we to continue our observations for much longer times, we could see the onset of shear-induced crystallization, and so we note that our experiments are probably studying a non-equilibrium state. Additionally, Fig. 4.4 on page 35 shows that our strain rate takes a while to stabilize after flow reversal, which again suggests that our results are not in steady-state. Thus, it is possible that our primary observation, that the shear-induced particle rearrangements are isotropic in character, is limited only to the transient regime we observe. It is still intriguing that in this regime, particle motion is so isotropic. For example, Fig. 4.4 on page 35 shows that the sample takes a while to requilibrate after shear reversal, yet there is no obvious signature of this in the particle motion or the configurations of the particles. Likewise, presumably the long-term crystallization will be caused by anisotropic motion (and result in further anisotropic motion), but no signs of this are present in the early-time amorphous samples we study. It would be interesting to conduct longer-term experiments to relate the particle rearrangements to those resulting in crystallization. Alternatively, it would be also interesting to use a cone-and-plate geometry shear cell capable of indefinitely large strains [42], to reach the steady-state constant shear regime.

By studying the plastic deformation in colloidal systems, we can have a better understanding on the mechanics of amorphous alloys [52, 53], which has unique scientific and potential practical interests. And the mechanic model on deformation is about the "shear transformation zone" (STZ) [53, 51, 8]. Different from the structural defect as in lattice dislocation, the STZ is an event that happens in locals [53, 51, 8] . Given that the experimental observation on alloys is hard, direct search for the local events are not available yet [53]. Therefore amorphous colloids are good experimental tools to test the mechanic in amorphous materials, or even predict new properties of the metals [51, 9] . Based on our results, we could propose that when amorphous alloys are under shear, the plastic deformation inside would extend in any directions, other than along the shear direction. And this could lead to a unique change on the electric bands, which would introduce an interesting electromagnet property into the alloy.

Chapter 5

Experimental techniques for studying emulsions

Besides colloids, I also use emulsion to study plastic changes under shear. Comparing to hard-sphere colloids, soft droplets allows us study their inter-forces from the deformed shapes. For this experiment, we need to make emulsion droplets with controlled size, and make sample chambers with desired geometries. So in this chapter I will talk about the experimental techniques on this emulsion experiment.

5.1 Producing emulsion samples

We make emulsion droplets using the microfluidic technique called "co-flow" geometry [113], by collaborating with Dr. Alberto Fernandez-Nieves at Georgia Tech. The idea is analogy to water dripping in a faucet. If we let water flow at a very low rate, water will drip out one droplet at a time. This droplet size is dependent on the surface tension (water to air), the faucet size, and the flow rate. If those factors are constant, the droplet size will be very stable. If the flow rate keeps increasing, a water stream or jet, rather than droplets, will be formed. Even if the jet could break down into droplets in the end, the size distribution will be in a large range.

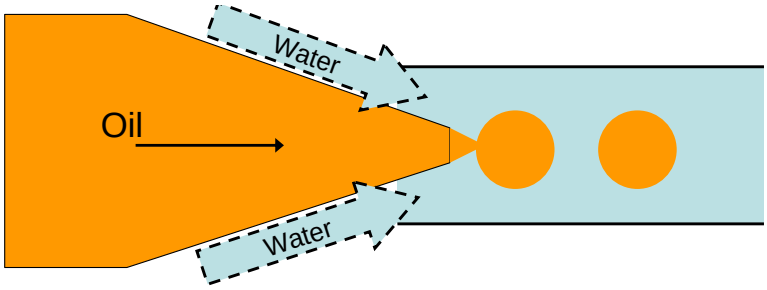

Figure 5.1: The sketch of co-flowing geometry for droplet making. The oil flow is in the inner tube, and the water with surfactant is flowing in the outer tube. The shear on the interface between the water and oil break the oil flow into droplets. This method could make oil droplets with narrow size distribution.

In the co-flowing geometry, instead of water in air, we make oil droplets in water (surfactant is added to stabilize droplets). The faucet we use is a pipette with a fine orifice of 40 μm size, pulled by a pipette puller and smoothed by a micro forge (Fig.5.3). As shown in Fig. 5.1, this circular capillary is carefully slid into another capillary of bigger size ($\sim$200 μm). We align up the two capillaries under microscope, trying to make their centers along one straight line. Therefore the small capillary is for oil flow and the larger one is for water flow. The oil we used is silicon oil from Fisher^{TM} (poly-dimethylsiloxane, density=0.963 kg/m^3, viscosity=100 mPas). And the surfactant in water is Fairy^{TM} soap (a polymer surfactant), which is strong enough to prevent droplets from coarsening. The capillary tubes are connected with the syringes. By using the syringe pump, we could control the flow rate precisely, and droplet size are quite monodisperse with less than 1% polydispersity. The flow rates I used in experiment is $\sim$0.1 ml/h for oil and $\sim$0.1 ml/min for water. And the droplet size under these flow speeds is around 300 μm in diameter. However, in Fig. 5.6, the polydispersity of the sample is much larger as shown in Fig. 5.2. To prevent crystallization, we use binary sample with radius $r = 240$ and 290 μm. But the polydispersity here is around 15%, much larger than what made from the coflowing geometry. It is due to the fact that droplet rupture when they are squeezed into the 2D chamber. The droplet breakup is significantly influenced by the surfactant,

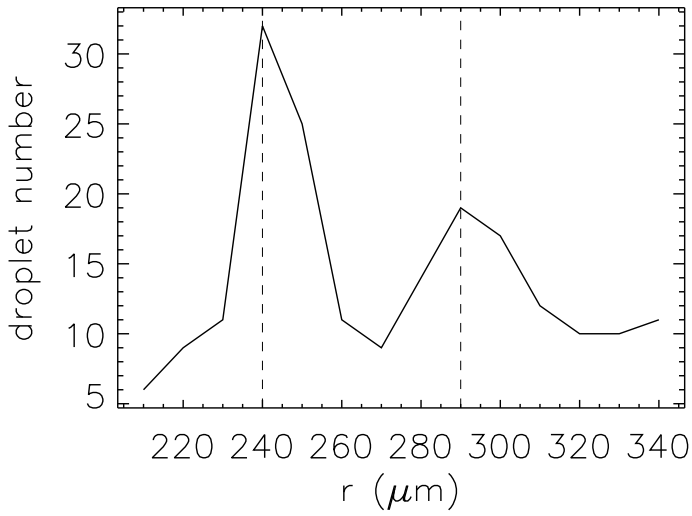

Figure 5.2: The radius distribution of droplet in Fig. 5.6. The sample is binary of droplet radius=240 and 290 μm, but with the polydispersity around 15%.

wetting characteristics of the chamber material, and the shearing. This has not been well understood yet, although people apply this to break up droplets in microfluidic technique [114, 115].

5.2 Microfluidic chip

Since in emulsion experiment (Chapter 7) the 2D chamber's wetting characteristics is significantly important for the droplets stability, we introduce two ways of making the microchannels with different materials, one is silicon glass, and another is PDMS (polydimethylsiloxane).

The glass chamber (Fig.5.4(a)) is basically made from two parallel glass slides separating by a thin film of Scotch^{TM} tape with $\sim$200 μm thickness (McMaster-Carr No.75975A658). By cutting out the hopper shape from the tape, we could make the channel between the glass slides. Since the double-sided Scotch^{TM} tape could be cut into any shape, we could make different channel easily. However, there is a limit to the precision for this hand making device. As seen in Fig. 5.6, the angles of the two sides of the hopper are not identical with 2° of uncertainty.

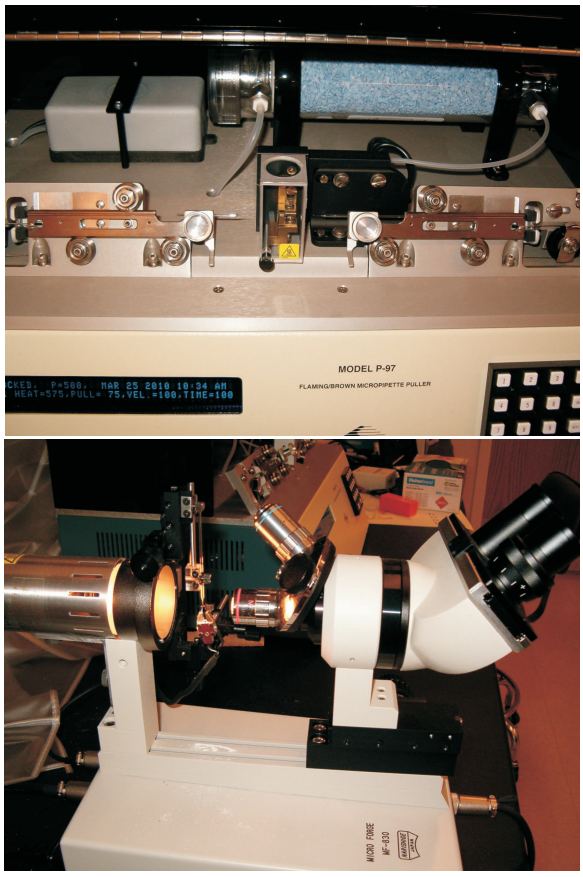

Figure 5.3: (a) The pipette puller in our lab to pull out a fine orifice for a capillary tube (Model P-97 from Sutter Instrument Co., USA). (b) The microforge in our lab to cutting pipette tips to particular sizes (MF-830 from Narishige^{TM}, Japan). The manipulation is precisely controlled under the observation of the microscope lens on the right.

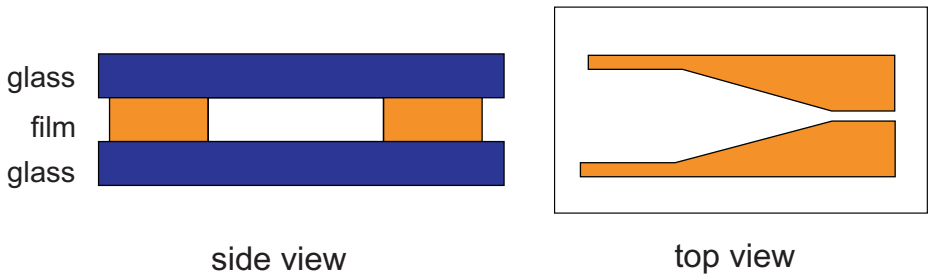

Figure 5.4: The sketch of micro channel made from glass slides. The double-sided Scotch^{TM} tape is sandwiched between two parallel glass plates (side view), determining the height of the micro channel. By cutting the tape into the channel shape (top view), the micro device could be made.

The gap of the chamber made from the double-side Scotch^{TM} tape is fixed, and so the choices for droplets sizes in experiment is limited. So if we want to study much smaller droplets, say 100 μm or even less, we need to either find a thinner tape or make the chamber in a quite different way. And the soft lithography is a technique for constructing micro devices [116, 117]. By collaborating with Dr. Hang Lu and her student Jan Krajniak at Georgia Tech, we make micro channels from PDMS (polydimethylsiloxane). The procedure shown in Fig. 5.5 is as following: First, the micro channel design is drawn by computer aided design tool (CAD), and a photo mask is printed by a high-resolution printer according to the design. Second, a silicon wafer is spin-coated with a thin film of photosensitive SU-8 epoxy. The film thickness determines the height of the micro channel (200 μm in my experiment). The coated wafer is then exposed under UV through the photo mask, and the microchannel pattern is created on the wafer. Third, PDMS liquid is casted on to the mold, and placed in a oven for solidation. Fourth, the solid PDMS channel is placed on a glass slide, after the inlets and the outlets are drilled out.

5.3 Bright-field microscope

A microscope is a common tool to investigate the structure of soft materials, due to the fact that the size of material components is usually 10nm -1mm. Bright-field microscopy is the simplest among kinds of optical microscopes, and it is used in my emulsion experiment (Chapter 7). The working principle of bright-field microscopy is: light source is focused by a condenser lens, projected to the sample placed on the stage, and then collected by the objective lens. The microscope I used is Leica^{TM} DM-IRB inverted microscope. To obtain a large field of view, we use low magnification: 1.6$\times$ objective lens and 0.33$\times$ C-mount. So the image size is 11.2$\times$8.5 mm^2. A CCD camera (Hitachi^{TM} KP-M2U) transmits the optical image into a computer, and images are

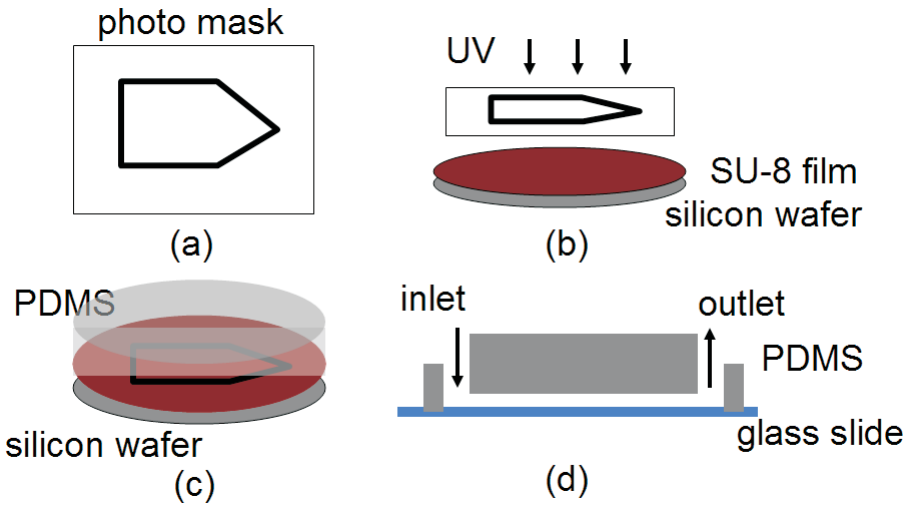

Figure 5.5: The procedure of the soft lithography [117]. (a) Photo mask of microchannel design is printed by a high-resolution printer. (b) Through the photo mask, the silicon wafer coated with photosensitive SU-8 film is exposed under UV light. And the design is created on the mold. (c) PDMS (liquid) is casted on the mold, and baked in a oven for a solidation. (d) After punched out the inlets and outlets, the solid PDMS channel is placed on a glass slide.

recorded by the software "OpenBox1.7" at the speed up to 30 frames per second. A image of bright field microscopy is dependent on the contrast between the indices of refraction of sample components. Take the oil-in-water droplet image from my emulsion experiment (Fig. 5.6) for example. Both oil and water are transparent, and light could pass through without changing the direction. Therefore, the image pixels are uniformly bright either outside of the droplets (water phase) or inside (oil phase). But on the droplet boundary refractive indices of the two media have large contrast (water 1.3 and silicon oil 1.5), which reflects the light and leaves the dark regions in the image. Basing on those dark round edges, we could identify individual droplets. The thickness of the dark boundary is dependent on the refraction difference, larger contrast thicker boundary. If there is any air bubble mixing inside, the boundary would appear thicker than oil droplets, given their refractive indices are 1.0 for air, 1.3 for water, and 1.5 for silicon oil.

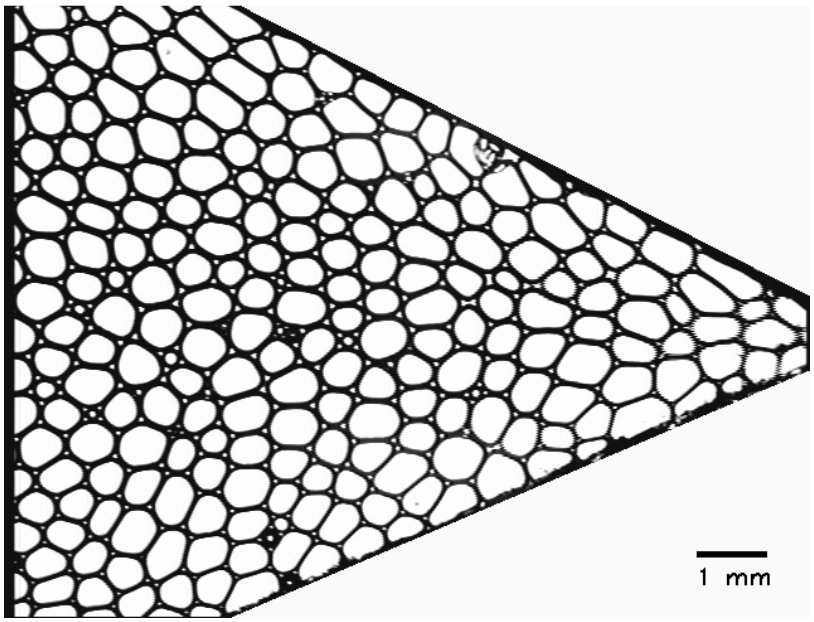

Figure 5.6: A image of the oil-in-water emulsion droplets from the experiment in Chapter 7. It is taken by a 1.6× objective lens and a 0.33× C-mount. The droplets are silicon oil in water with the surfactant Fairy^{TM} soap (a polymer surfactant). To prevent crystallization effect, binary droplets (0.29 mm and 0.24 mm in diameter) are used, with polydispersity 15%. Its dark boundary comes from the contrast between the refractive indices of the silicon oil (1.5) and water (1.3), where the light is reflected and less amount is collected by objective lens. The angle of the channel is 25°±2°. The whole field of view is 11.2 mm×8.5 mm, and the scale bar is 1 mm. The gap of the chamber between the two parallel glass slides are around 0.2 mm.

Chapter 6

Computational techniques for studying emulsions

In emulsion experiment, we want to identify droplet shapes for force calculation, as well as center position for dynamic motions. Besides, the images of emulsion and colloids are quite different. Therefore, we need specific algorithms for the emulsion experiment, and some of them are different from colloids algorithm discussed in Chapter 3.

6.1 Emulsion droplet identification algorithm

As indicated in Fig.5.6, the emulsion droplet could be identified from its black boundary where the light is reflected at the interface between oil and water. The original idea of the program is from Ken Desmond, which is as following. First, we choose a brightness threshold, less bright pixel set to be 0 and the rest be 255 (Fig. 6.1(a)-(b)). By this way, the original image is simplified into a binary one, where black (0) is boundary and bright (255) is oil or water. Second, we use the blob coloring method (IDL code "label_region") to distinguish individual droplet areas, and take the middle positions for droplet centers (Fig. 6.1(c)-(d)). Third, from those centers we search

for the nearest black point at an angle, and identify it as a point on the boundary. As shown in Fig. 6.2(a), We use 200 boundary points to represent one droplet from angles equally around the center in 360 degrees. And from the 200 point convex shape we calculate the droplet radius, deformation, and other quantities. The radius r is the mean of the distances r_i from the center to the boundary points. Fig. 6.2(b) shows the radius r as a function of time. The noise is partly due to the fact that the droplet shape changes during the time, as well as the image resolution. However, the uncertainty of the radius is within 10%.

$$r = \langle r_n \rangle = \left(\Sigma_{n=1}^{200}\ r_n\right)/200, \tag{6.1}$$

and the deformation D is the standard deviation of r_i

$$D = \frac{\sqrt{\langle r_n^2 \rangle - \langle r_n \rangle^2}}{\langle r_n \rangle}, \tag{6.2}$$

where $\langle r_n^2 \rangle = \left(\Sigma_{n=1}^{200}\ r_n^2\right)/200$.

The tracking algorithm for droplets is similar to for colloids in Chapter 3. Given the sample is not monodisperse, we make sure the moving distance between consecutive frames are less than the smallest droplets.

6.2 Neighbor identification algorithm

An amorphous solid, unlike crystalline, has no long-range order. So in the disordered structure, particles motions are directly influenced by their neighbors. Therefore, it is important to identify "neighbors" when studying microscopic structures. Generally, there are two ways to define neighbors. One is the particle distance is shorter than a certain threshold. This definition is used in the data analysis of my colloidal experiment (Chapter 4), where colloids have a fixed spherical shape. Another way

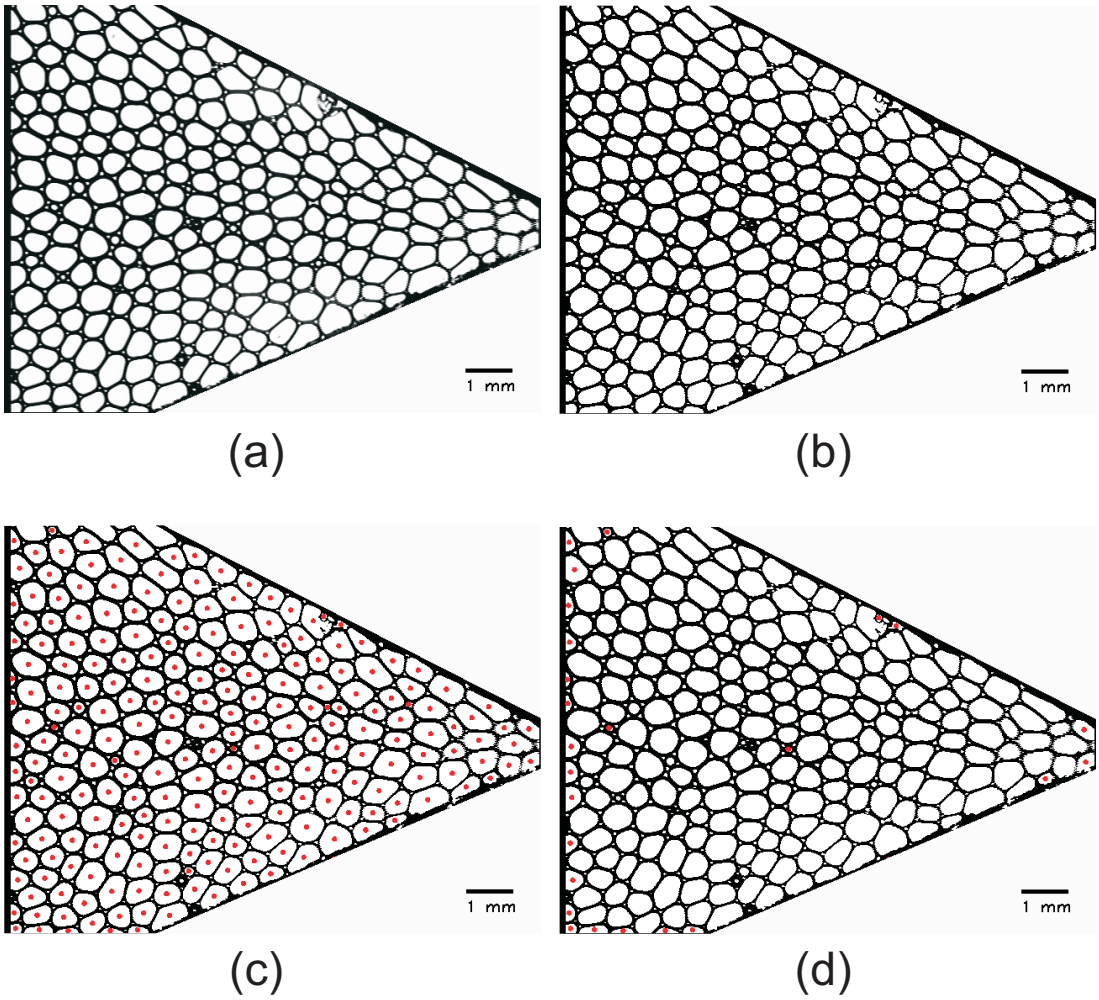

Figure 6.1: (Color online) Steps for emulsion droplet identification. We first set the threshold value (100 here) for pixel brightness of the original image (a), and simplify it into a binary picture (b), 0 for less bright and 255 for more. Then we use the blob coloring method (IDL code "label_region") to identify individual droplets, and the centers of those regions are set to be the droplet positions (labeled by red points in (c)). Finally, we eliminate the droplets either with too small radius or with incomplete shape on the boundaries, as shown in (d).

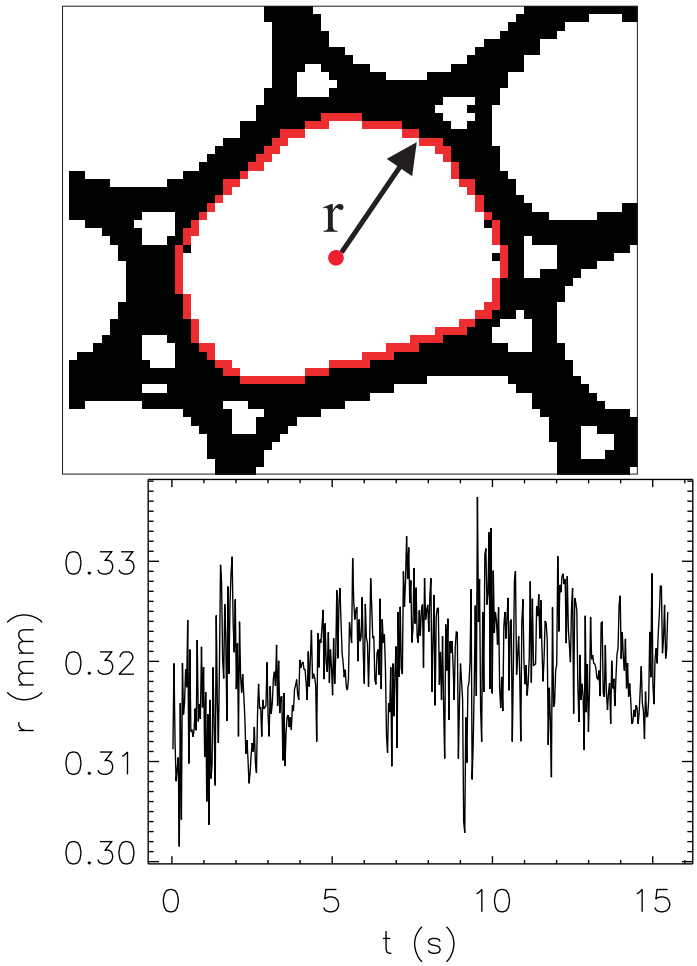

Figure 6.2: (a) The perimeter of a droplet from 200 points on its boundary. The radius r is from the center to the boundary points. (b) The radius r as a function of time.

is using Voronoi diagram or Dirichlet tessellation [118, 119, 120]. As Fig.6.3 shows, Delaunay triangulation (blue line in (a)) is applied on the particles positions, where the network cuts the space into small triangles. And then the Voronoi polygons (red in (b)) are generated basing on the Delaunay triangulation. Those polygons are considered as the local free space for individual particles. And particles who share the boundaries are considered as nearest neighbors. There are different definitions to draw Voronoi polygons or cells, and one common way is requiring boundary points have equal distances to the neighboring particles, $d_i = d_j$ in Fig.6.3(c). Given the polydispersity of the sample, we use the definition of Laguerre (radical) tessellation [118, 119, 120]. In this geometry, the Euclidean distance d_i and d_j are weighted by the radius of particle i and j (r_i and r_j). Therefore, the relation $d_i = d_j$ in Voronoi tessellation changes into $d_i^2 - r_i^2 = d_j^2 - r_j^2$ in Laguerre (radical) tessellation. By this weighted geometry, bigger droplets tend to have larger cells or free spaces. In the data analysis of my emulsion experiment (Chapter 7), I use this Laguerre (radical) tessellation to identify "neighbors" for deformed droplets. The program is original from Ken Desmond.

6.3 Neighbor switch algorithm

A typical plastic rearrangement I want to observe is called "T1 events". It describes four neighboring droplets slipping through each other with topological rearrangements. As shown in Fig. 6.4, two neighboring particles are separated apart, and other two squeeze in between and become new neighbors. As discussed above, "neighbors" is based on the Laguerre (radical) Voronoi. This definition is actually very sensitive to the noise from droplet identification. Besides, for two droplets on the edge of "neighboring", if they are just rattling a little bit in local space with no much difference to eye, it could be identified as a dramatic event by the program as "neighboring apart"

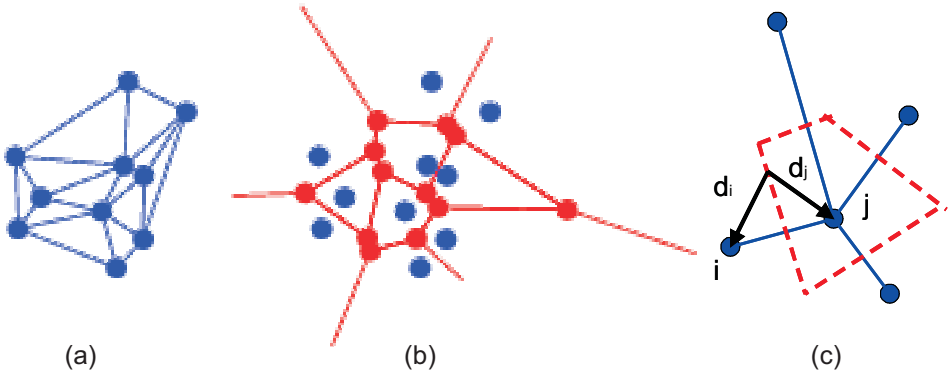

Figure 6.3: (Color online) Voronoi diagram. The image is from http://mathworld.wolfram.com/VoronoiDiagram.html. (a) Delaunay triangulation create a network of particle positions (blue points), cutting the space into the triangle cells. (b) Voronoi polygons (red) is generated from the triangulation, and the red dots are the vertices of voronoi. (c) One of the common Voronoi tessellation is requiring boundary points have equal distances to neighboring nuclei points $d_i = d_j$. In Laguerre (radical) tessellation, the Euclidean distance is weighted, and the relation is $d_i^2 - r_i^2 = d_j^2 - r_j^2$, where r_i^2 and r_j^2 are the weights for nuclei points i and j. And we use droplet radius as the weight r_i for each droplet, which gives larger droplets larger voronoi cells.

or "neighboring rejoin". So to eliminate the noise affect on the Voronoi definition, I add extra criteria for "neighboring apart": the centers of particles should move away at least 10% of their distance. And in the similar way, for "becoming neighbors", I require two droplets move closer no less than 10% distance, as well as being new neighbors from Voronoi tessellation. And to find T1 event, the program searches "new neighbors" at one time step, and "old neighbors" at another time step. And then we draw a line between each pair of droplet centers as "neighbor bonds". If the old bonds and new bonds are crossing, we take it as one T1 event, where one neighbor bond break and another bond forms at the same time.

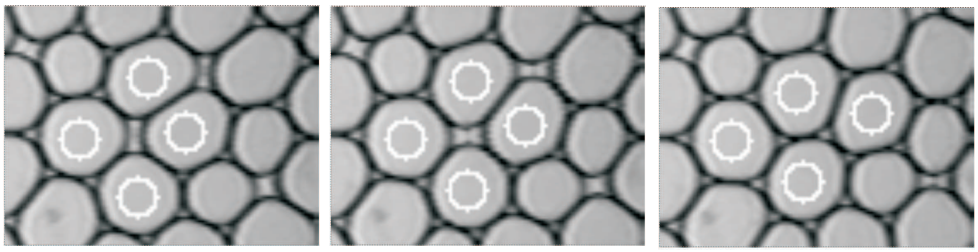

Figure 6.4: (a)-(c) The three images show a typical T1 rearrangement between the four particles labeled by circles. The field of view is around 1×1 mm^2, and the time interval of this rearrangement is around 1 s.

Chapter 7

Stress flucatuations in a 2D frictionless flow through a hopper

7.1 Introduction

As discussed in Section 1.4, force network has been found in jammed materials in both frictional [4, 25] and frictionless systems [2, 21, 19]. In this network, small portion of particles support large stresses, and there are strong spatial correlations between them, forming "force chains" [19, 20]. This chain structure determines the rigid nature of dense materials under static state [19, 20]. Because the force chain is contributed by small amount of particles, it changes or fluctuates under shear [22]. The yield flow of jammed material under shear has been studied in many previous work, where particles' deformation in force chains [22, 121, 122, 123, 124] and local rearrangements [125, 126, 127, 86, 128, 73, 129, 74] are examined. It is found that the distribution of force impulses or fluctuations are related to the force network inside the material [130, 22]. Recent simulations founds that without static friction, the force distribution would be more heterogeneous, and force chains could extend to a longer length scale [24]. Therefore, we hypothesize that comparing to frictional grains, frictionless systems could have more fragile force chains, and the stress fluctuations

could be more obvious under shear.

Comparing to the force study in the static case [21, 19, 4, 25], the experiments and simulations on dynamic flow are still limited. And many geometries focus on the Couette shear [22, 130, 131, 128, 132, 125], as discussed in Fig. 1.5. In other geometry, for example flow through a hopper, people also found large stress fluctuations [23, 133]. In the granular hopper experiments [23, 133], the flux rate is almost constant over time without intermittent and shocks (see in Section 1.4). Therefore, this suggests to us that the stress fluctuations on the wall comes not from the unsteady flow rate, but maybe the changes of force chains inside the dense flow. Given that force fluctuations are found in frictionless bubbles under Couette shear [128, 86, 125], we conjecture that stress fluctuations could also be found when emulsion flows through a hopper. In addition, it is interesting to us to understand plastic changes in sheared flow by comparing systems with and without static friction.

In addition to macroscopic stress fluctuations during yielding under shear, people are also trying to understand the plasticity through micro rearrangements [134, 16, 17, 123, 73, 74, 69, 9]. As discussed in my colloidal experiment (Chapter 4), the idea of shear transformation zones ("STZ") is proposed by Spaepen in late 70s [51] and later developed by Falk and Langer [8]. This theory describes plasticity as irreversible local rearrangement between particles during shear. And in frictionless system, the so-called "T1" event is studied as an elementary plastic rearrangement [134, 16, 17], as shown in Fig. 6.4. The "T1" event describes four neighboring droplets slipping through each other with topological rearrangements. Although this micro rearrangements has been studied in previous work [134, 16, 17, 123, 74, 69, 9], its relation to the stress fluctuation is still not clear yet. Although simulation [135] and experiments [134, 123, 74] found some evidences, more experimental proof are still in need.

Therefore, we use frictionless emulsion to study the stress fluctuations in the dense flow through a hopper. Similar to the idea of using 2D photoelastic disks studying 3D

jamming of granular materials [21, 19, 22], we use 2D emulsion by squeezing droplets into a thin chamber forming disk shapes. By tracking individual particles, we are able to study their microscopic rearrangements and plastic changes during the flow. At the same time, we are able to quantify the stress on droplets from the deformed droplets in 2D images. Therefore in our 2D emulsion experiment, we are investigating the relation between the macro stress and micro dynamics.

7.2 Results

Fig. 7.1 is a list of six emulsion data flowing through the 2D hopper. They have almost the same shape of hoppers and the same area fraction of samples. But the flux rates range from 0.33 to 2.93 mm^2/s. To study the situations with different flux rates, we compare the data 1, 5 and 6 in the following.

The typical data we discuss below is the data 1, which has the largest flux rate.

Data	Flux Rate (mm^2/s)	Mean Droplet Radius (mm)	Area Fraction	Hopper Angle (degree)	Orifice Size (mm)
1	2.93	0.266	0.90	25.0 +/- 1.9	1.1
2	0.83	0.251	0.92	27.4 +/- 1.9	0.7
3	0.75	0.136	0.93	27.4 +/- 0.4	0.4
4	0.33	0.136	0.94	27.4 +/- 0.4	0.4
5	1.33	0.168	0.90	25.5 +/- 0.2	0.8
6	0.61	0.150	0.91	25.7 +/- 0.6	0.6

Figure 7.1: The table list of six emulsion data with different flux rates. To study the situations with different flux rates, we compare the data 1, 5 and 6 in the following.

7.2.1 Flow profile

To understand the velocity field and the shearing condition in our emulsion flow, we first investigate the velocity profiles at two locations with different widths, as shown

in Fig. 7.2. It is found that at both locations, the velocity profiles could be fitted well by parabolic curves. In contrast to the results described in Chapter 4, where the colloidal suspension exhibited a shear band (Fig. 4.3), for our flowing emulsion we do not find a shear band. Given that channel width is less than 20 droplet size, this smooth distribution of flow profiles may be from the confinement effect on hopper boundary [65]. And this similar tendency is also found in much smaller flow rate, as found in Fig. 7.2(c)-(d). Given the velocity profiles in Fig. 7.2, we use parabolic

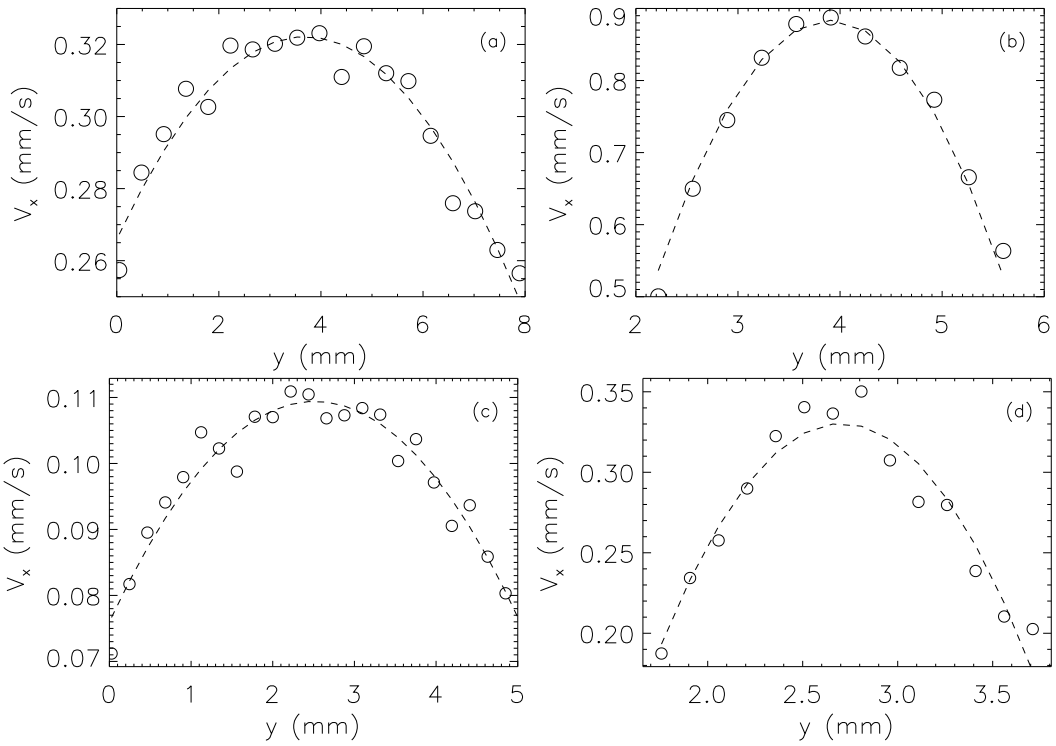

Figure 7.2: (a) Data 1: $V_x(x, y)$ (circle) distribution in the left side of channel with the width of around 20 droplet diameters. The dash line is the parabolic fitting curve as in Eqn. 7.1. (b) Data 1: $V_x(x, y)$ distribution at the right side the channel with the width of around 7 droplet diameters. (c) and (d) are for the data 6 with the similar analysis to (a) and (b).

fitting for all x locations along the hopper, which is

$$V_x(x, y') = \beta(x) \times y'^2 + \alpha(x). \tag{7.1}$$

The $y' = y - y_{cent}$ is the relative position along y axis to the channel center. The fitting parameters α is the flow velocity along the center of the hopper. And β is the curvature of the parabolic velocity profiles. The distributions of α and β along the channel (x axis) are shown in the Fig. 7.4(b)-(c).

Given that the flux rate is an important control parameter in my experiment, we can calculate it from the droplet tracking in the movie. Since our tracking is based droplet centers, as shown in Fig. 7.3, the space that droplets can go actually is one radius away from the real hopper boundaries. And $w(x)$ is defined as the channel width that droplet centers can reach, which is between the dashed lines. So the real flux rate $A(x)$ includes two parts. One is the integration of the continuous flow across the width of $w(x)$ along y axis, which is $\int_{\frac{-w(x)}{2}}^{\frac{w(x)}{2}} V_x(x, y') \times dy'$. And another is half-size droplets sliding along the real boundaries, which is $V_x(y' = \frac{w}{2}) \times \langle d \rangle$, where $\langle d \rangle$ is the mean droplet diameter. Therefore the flux rate of the 2D flow can be written as

$$A(x) \ = \int_{\frac{-w(x)}{2}}^{\frac{w(x)}{2}} V_x(x, y') \times dy' + V_x(y' = \frac{w}{2}) \times \langle d \rangle. \tag{7.2}$$

And by using the parabolic fitting in Eqn. 7.1, the area flux can be expressed as

$$\begin{aligned} A(x) &= 2 \int_0^{\frac{w(x)}{2}} V_x(x, y') \times dy' + (\beta \times (\frac{w}{2})^2 + \alpha) \times \langle d \rangle \\ &= \frac{1}{12} \beta(x) \times \big(w^3(x) + 3\langle d \rangle w^2(x)\big) + \alpha(x) \times \big(w(x) + \langle d \rangle\big). \end{aligned} \tag{7.3}$$

Given the flux is controlled by syringe pump, $A(x)$ should be steady along the channel and independent of x, which is confirmed in Fig. 7.4(d).

In Fig. 7.4(a), the channel width is decreasing linearly along x. This is determined by the geometry of the hopper, with the boundary angle of $\theta \approx 25°$. And this distribution can be fitted by

$$w(x) = 2 \times \tan(\theta)(x_0 - x), \tag{7.4}$$

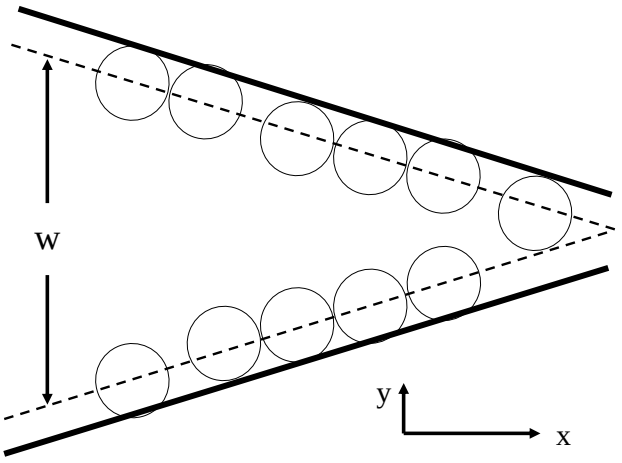

Figure 7.3: A sketch of the hopper with the thick boundaries. The dashed lines are the limit where droplet centers can reach in the channel. W is defined as the width that droplet centers could go. x axis is in the direction of flow, and y axis is the direction perpendicular to flow.

where x_0 is the position where the dashed lines meet in Fig. 7.3. Given that $A(x)$ in Eqn. 7.3 should be independent of x, we assume that both $\beta \times \big(w^3(x) + 3\langle d\rangle w^2(x)\big)$ and $\alpha(x) \times \big(w(x) + \langle d\rangle\big)$ are constants. Therefore, we fit the α by using

$$\alpha(x) = \frac{k_\alpha}{\big(w(x) + \langle d\rangle\big)}, \tag{7.5}$$

which works well in Fig. 7.4(b). we can fit the β by using

$$\beta(x) = \frac{-k_\beta}{\big(w^3(x) + 3\langle d\rangle w^2(x)\big)}, \tag{7.6}$$

which works well in Fig. 7.4(c). And so the flux rate $A(x)$ can be obtained as

$$A(x) = k_\alpha - k_\beta/12. \tag{7.7}$$

Given α is the flow velocity along the center of the hopper, Eqn. 7.5 shows that it is almost inversely proportional to the width of the channel. It is easy to understand since the flux rate along the channel is constant and flow speed should be larger at

narrower regions. The parameter β, induced by the wall effect [65], relates to the local strain rate, which is obvious in Eqn. 7.9. In other words, more α means droplets move faster, but more β means more local strains which is what we think is most important for local rearrangements ("T1 events"). So Eqn. 7.6 shows how confined boundary effect the velocities inside the dense flow. And giving the consideration of both "constant flux rate" and "wall confinement", we finally can obtain the flux rate A by Eqn. 7.7.

To check if the area flux rate is steady along the channel, we plot $A(x)$ in Fig. 7.4(d), by using Eqn. 7.2 and the parabolic fitting in Eqn. 7.1. And the dash line $A(x) = k_\alpha - k_\beta/12 = 2.93$ mm^2/s is from the math fitting in (a)-(c). From the graph, we can see the flux rate $A(x)$ is almost steady in the channel along the x axis, within the standard deviation less than 5%. It also confirms the gap of our chamber is almost uniform along the channel. And similar results are found in other data, as shown in Fig. 7.4(e)-(h).

The fitting above is an typical example for getting the velocity profiles from the flow through a hopper. And we use the similar fitting for all six data listed in Fig. 7.1, and the result is shown in Fig. 7.5. We find that those fitting parameters k_α and k_β are linearly dependent on flux rate A. In other words, those flow profiles can be scaled by the flux rate $A(x)$, which confirms our fittings discussed above. In addition, $k_\beta \approx 2 \times k_\alpha$. It suggests that the "wall confinement" has stronger influence on the faster flow than "constant flux rate", which leads to larger strain rates distributing in the narrow regions.

So basing on the fitting in Fig. 7.4, the velocity distribution in the channel could be written as

$$\begin{aligned} V_x(x, y') &= \beta(x) \times y'^2 + \alpha(x) \\ &= \frac{-k_\beta}{\big(w^3(x) + 3\langle d\rangle w^2(x)\big)} \times y'^2 + \frac{k_\alpha}{\big(w(x) + \langle d\rangle\big)}, \end{aligned} \tag{7.8}$$

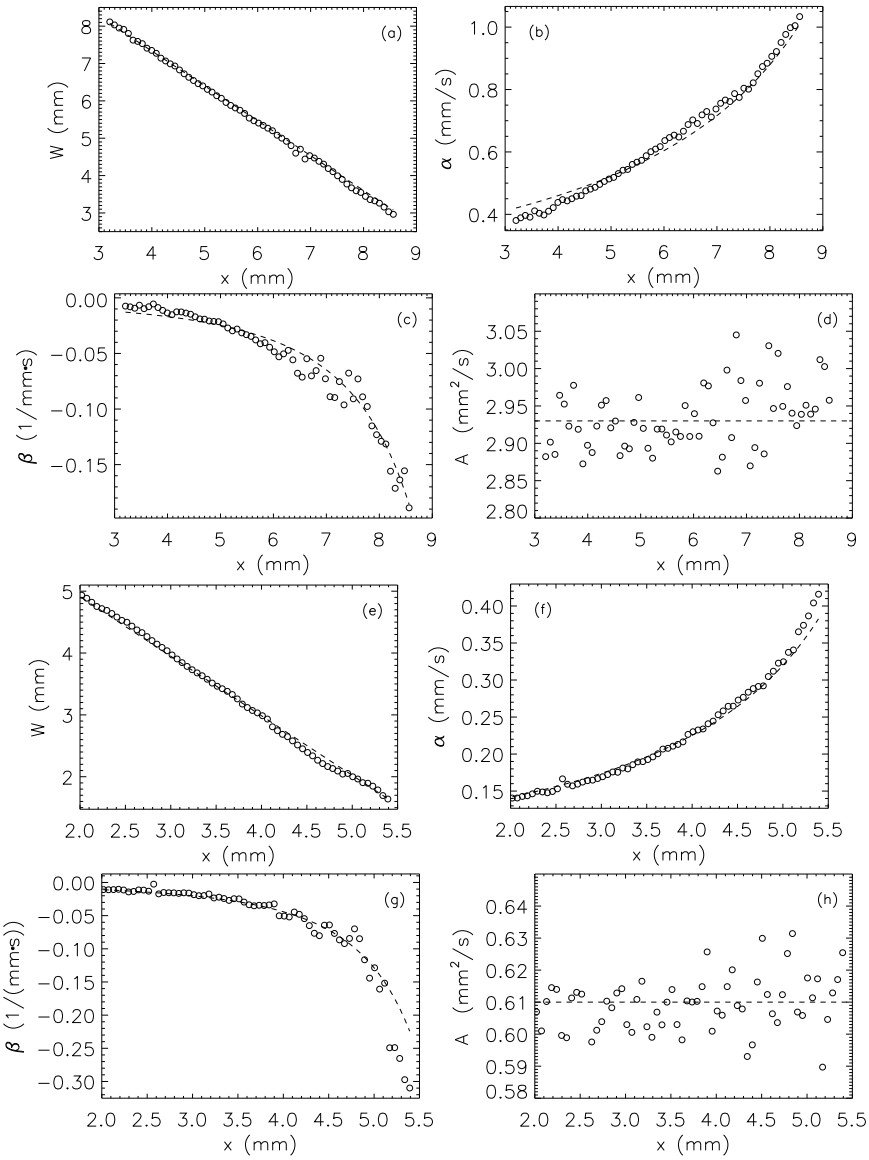

Figure 7.4: (a) Data 1: width of channel $w(x)$ as a function of x position. The dashed line is from Eqn. 7.4 with $\theta = 25^\circ$ and $x_0 = 11.86$ mm. (b) Data 1: The parameter $\alpha(x)$ as a function of x position. The dashed line is from Eqn. 7.5 with $k_\alpha = 3.6$ mm^2/s and $\langle d \rangle = 0.24$ mm. (c) Data 1: The parameter $\beta(x)$ as a function of x position. The dashed line is from Eqn. 7.6 with $k_\beta = 8.0$ mm^2/s. (d) Data 1: Area flux $A(x)$ as a function of x position. The hollow circles are based on Eqn. 7.3, with the parameters $\alpha(x)$, $\beta(x)$ and $w(x)$ from the parabolic fitting in Eqn. 7.1. The dashed line is $A(x) = k_\alpha - k_\beta/12 = 2.93$ mm^2/s. (e)-(h) are for the data 6 with the similar analysis above. (e) Data 6: Eqn. 7.4 with $\theta = 25.7^\circ$ and $x_0 = 7.1$ mm. (f) Data 6: Eqn. 7.5 with $k_\alpha = 0.735$ mm^2/s and $\langle d \rangle = 0.14$ mm. (g) Data 6: Eqn. 7.6 with $k_\beta = 1.5$ mm^2/s. (h) Data 6: flux rate $A(x) = 0.61$ mm^2/s from Eqn. 7.7 with $k_\alpha = 0.735$ mm^2/s and $k_\beta = 1.5$ mm^2/s.

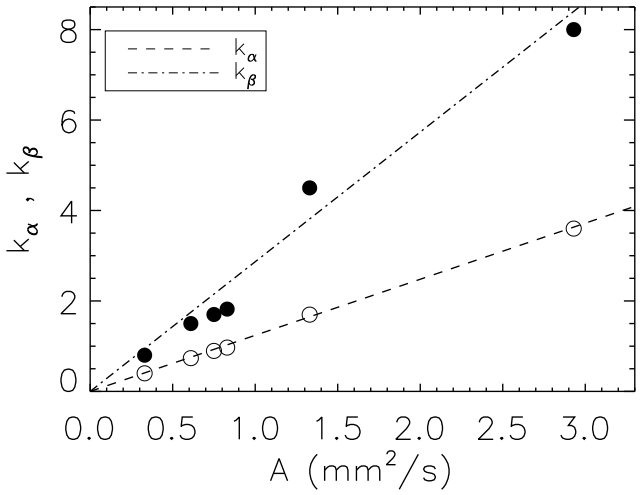

Figure 7.5: The fitting parameter k_α and k_β as a function of flux rates from the listed data in Fig. 7.1. The slope of the straight line for k_α is 1.24, and the slope of straight line for k_β is 2.87.

which is shown in Fig. 7.6(a). The darker color corresponds to the larger magnitude, and white curves are contour lines. Due to the hopper geometry, the velocity is larger (darker) when close to the narrow end. And because of the shearing and confinement effect from the boundary, the velocity contour lines are smooth. In addition, the distribution of the strain rate $\dot{\gamma}$ could be derived from Eqn. 7.1, which is

$$\dot{\gamma}(x, y') = \delta V_x(x, y')/\delta y' = 2\beta(x) \times |y'|. \tag{7.9}$$

As shown in Fig. 7.6(b), the large strain rates concentrate on the boundary sides near the narrow end of hopper.

7.2.2 Rearrangements

Due to the strain rates from the velocity field, there are rearrangements between droplets. The rearrangements lead to deviation from the mean velocity field, which we call nonaffine motions in Chapter 4. The nonaffine rearrangement could be calculated

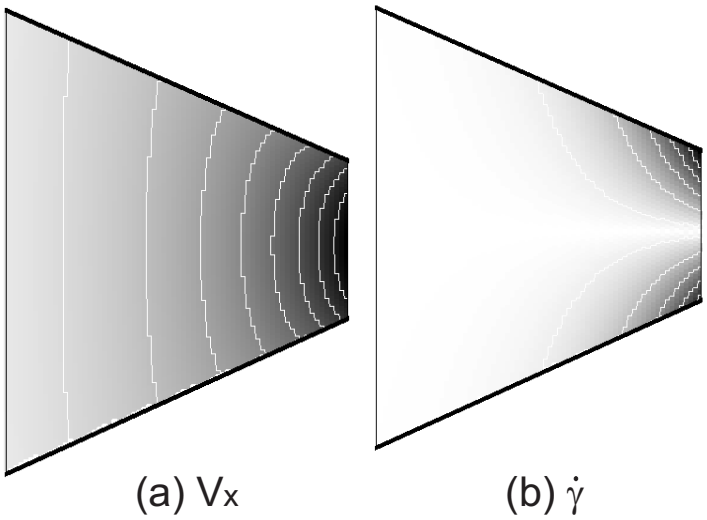

Figure 7.6: (a) The distribution of velocity profile V_x, basing on Eqn. 7.8. (b) The distribution of strain rate $\dot{\gamma}$, basing on Eqn. 7.9. The darker color corresponds to the larger magnitude, and the white curves are contour lines.

by removing the mean Eqn. 7.1 from the real velocities of droplets,

$$\tilde{V}_x(x, y) = V_x - \beta(x) \times y'^2 - \alpha(x). \tag{7.10}$$

Fig. 7.7(a) is the probability of nonaffine motion $\tilde{V}_x$ at two x locations 3.5 (hollow circles) and 7 mm (solid circles). Both have non-Gaussian tails, and the $\tilde{V}_x$ for narrower location has larger standard deviation. Given that the distribution of the velocity field could affect the nonaffine rearrangement, we normalize the nonaffine motion by the velocity field $\tilde{V}_x/V_x$, and get the Fig. 7.7(b). After the normalization, the probability distributions seem to overlap to each other. And this tendency holds for nonaffine motion at all location of the hopper, as shown in Fig. 7.7(c). This velocity scaling suggests that there are some similarity between the rearrangements at different locations of the hopper. But it also implies that in the narrower region with larger flow rate, the kinetic energy for rearrangement is larger, which could lead to some irreversible plastic changes during the flow. In Fig. 7.7(c), there is a bumper on the left shoulder. It is due to non symmetrical shape of the hopper, where

the boundary angles have $\pm 2^\circ$ bias. And in Fig. 7.7(d), we see the scaled nonaffine motions $\tilde{V}_x/V_x$ do not symmetrically distribute along y axis. Fig. 7.7(e)-(h) shows that this scaling of nonaffine motion $\tilde{V}_x$ by velocity V_x holds for all the data with different flux rates.

To quantify the plastic rearrangement, we use the definition of "T1" event [134, 16, 17] as introduced in Fig. 6.4. Fig. 7.15(a) shows the distribution of T1 events in the hopper. Most of the T1 events happen near the narrow region, which confirms that larger nonaffine motion have higher chance of triggering plastic events.

7.2.3 Stress fluctuations

Plastic changes of materials usually involves large energy fluctuations in macro mechanics. And this mechanical change is related to the stress distribution inside material. There are two ways to quantify interaction between droplets, one is from droplet contacts and another is from their deformed shapes. Because of the surface tension, the 2D droplets prefer to have round shape. When under compression or stress from neighbors, a droplet would be deformed, and at the same time have contact area with the neighbors. The larger the stress is, the larger contact and larger shape deformation the droplet would have.

From the image, we identify the droplet contact (green lines) as shown in Fig. 7.9(a). Similar to the droplets' interaction in 3D [4], we assume the force magnitude between droplets is proportional to their contacts $l_{contact}$. Therefore, the interaction in 2D could be written as $f_{contact} = \sigma l_{contact}/R'$, where $R' = R_{gap}R_{2D}/(R_{gap} + R_{2D})$ and σ is the surface tension [136]. R_{gap} and R_{2D} are the two radii of curvature of the quasi-2D droplet, one is from the side view of the narrow chamber, and another is from the top view. R_{gap} is the radius between the channel gap, which is approximately half channel gap $H/2$. And R_{2D} is the disk radius in the 2D image taken from the channel top. Given that $R_{gap} < R_{2D}$ in the 2D system, R' is approximately equal to

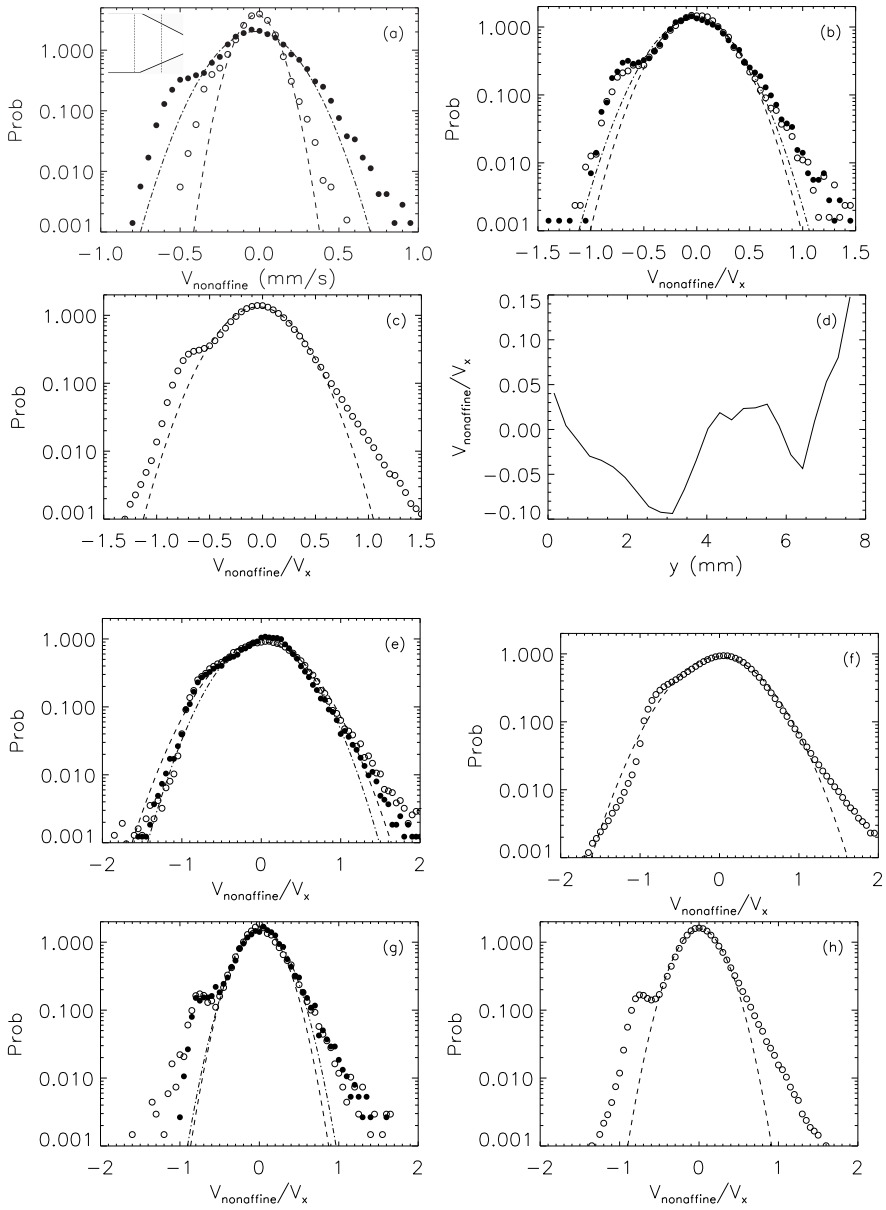

Figure 7.7: (a) Data 1: The probability distribution of nonaffine mobility $\tilde{V}_x$ at $x = 3.5$ mm (hollow circles) and 7 mm (filled circles). The region at $x = 3.5$ mm has the width of 16 droplet diameters, and the region at $x = 7$ mm has the width of 9 droplet diameters. The dashes lines are Gaussian fitting. (b) Data 1: The probability distribution of $\tilde{V}_x$ normalized by V_x at $x = 3.5$ mm (hollow circles) and 7 mm (filled circles). The dashed lines are Gaussian fitting. The two curves almost overlap to each other. (c) Data 1: Probability distribution of $\tilde{V}_x$ normalized by V_x for all the droplets in the channel. The data are averaged over 2700 droplets from a movie of 200 s. (d) Data 1: Averaged $\tilde{V}_x/V_x$ as a function of y. (e) Data 6: similar analysis to (b) for the data 1. (f) Data 6: similar analysis to (c) for the data 1. (g) Data 5: similar analysis to (b) for the data 1. (h) Data 5: similar analysis to (c) for the data 1.

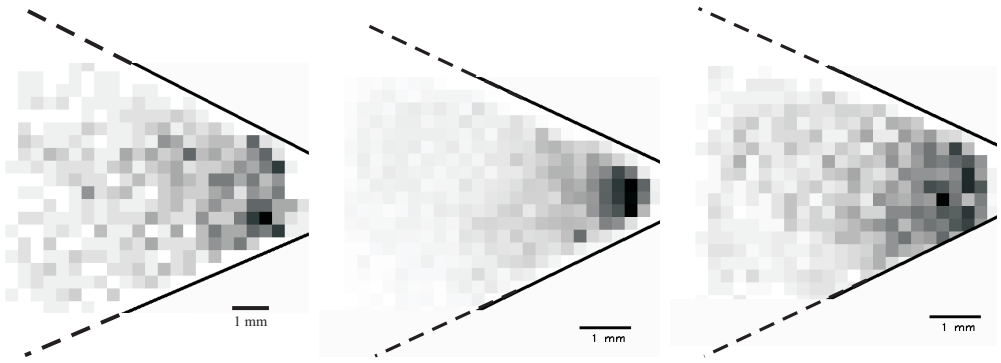

Figure 7.8: (a)-(c) The distribution of T1 events in the channel for the data 1, 6, and 5. The dark color corresponds to the higher probability of T1 rearrangements in that region. Due to the image-size limit, part of the channel on the left can not be observed, which is extended by the dashed lines.

R_{gap}, which is close to the half of the chamber gap $H/2$. So $f_{contact} \approx 2\sigma l_{contact} H$, where H and σ are constant for droplets in the same chamber. Fig. 7.9(b)-(d) is the probability distribution of contacts. Given that force magnitude $f_{contact} \sim l_{contact}$, the shape of distribution of $l_{contact}$ is also that of the stresses. The tail of large contact (or large force) shows that the probability distribution has an exponential decay, similar to the stress distribution found in 3D frictionless emulsion [4]. To check the spatial distribution of those large stress or contact, we plot Fig. 7.9(a). The large stresses are represented by the thick red lines. The graph shows that most of the large stress are near the hopper boundary, and some of them align up into chains perpendicular to the wall. This perpendicular orientation of large force chains is due to the shearing on wall [137, 19]. And because large shear rates concentrate near the wall of the narrow region (Fig. 7.6(b)), the large stresses tend to distribute in this region. From Fig. 7.9(a), the red color indicates large interacting forces between droplets. It shows that those large (red) force chains extend several droplet sizes. And when the gap narrows down to this size on the right side, the chains cross both sides of the hopper forming a temporary (jamming) arch, which is similar in granular materials [3]. In addition, those large force chains starting from wall suggest that the the stress on the wall is directly related to that inside the hopper. Therefore, the micro rearrangements

happening in the flow could affect the macro stress on the boundary.

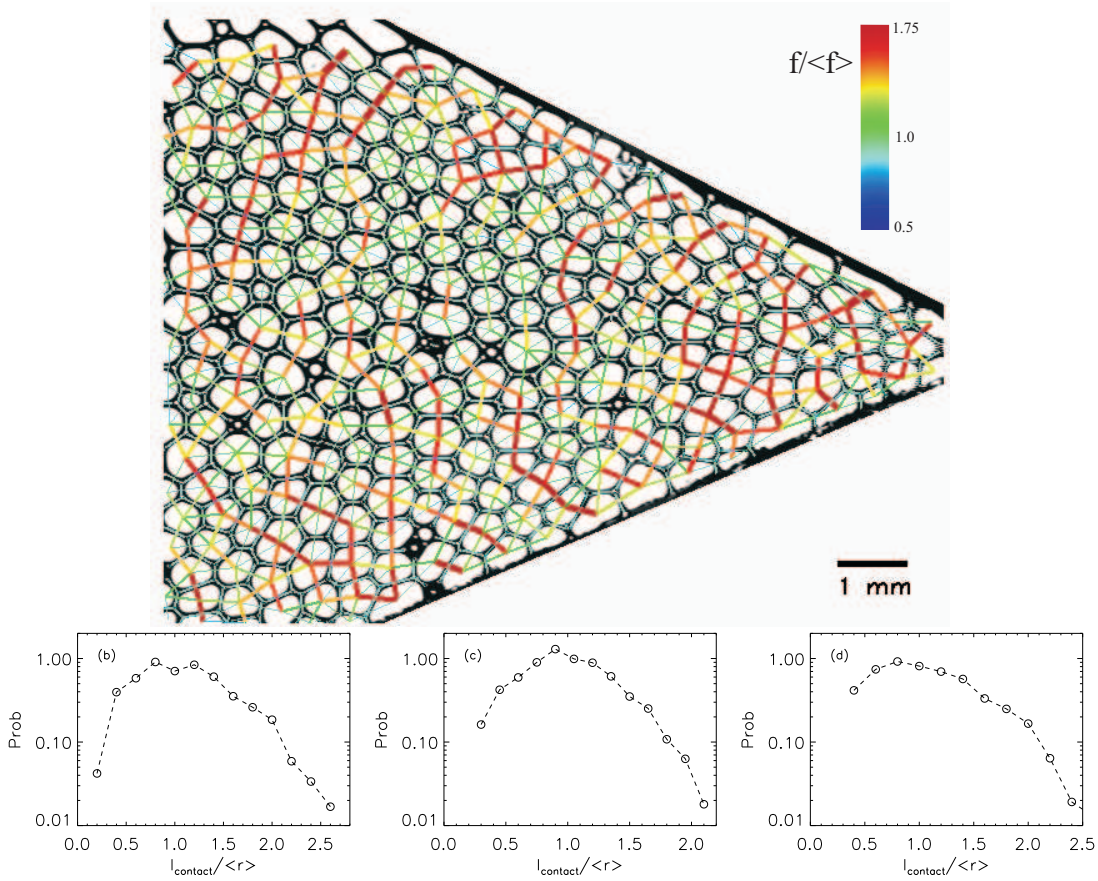

Figure 7.9: (a) A force map from a image of the data 1. The contacts (green lines) between neighboring droplets are identified by the code originally from Ken Desmond. By assuming the contact forces are linearly dependent on the contact length, we plot the short bonds connecting droplet centers to represent the interactions between them. The bond thickness of are linearly independent on the force magnitude. And the color bar indicates the stresses, linearly increasing from $0.5\langle f_{contact}\rangle$ (blue) to $1.75\langle f_{contact}\rangle$ (red). The stresses smaller than $0.5\langle f_{contact}\rangle$ are colored blue, and the stresses larger than $1.75\langle f_{contact}\rangle$ are colored red. And the stress between is colored based on the color bar. (b) The probability distribution of contact $l_{contact}$ from (a). (c)-(d) The probability distribution of contact $l_{contact}$ from images of data 6 and 5.

Another way to quantify the stress on a droplet is based on its deformed shape. We define the droplet deformation as the standard deviation of the radius:

$$D = \frac{\sqrt{\langle r^2\rangle_\theta - \langle r\rangle_\theta^2}}{\langle r\rangle_\theta}, \tag{7.11}$$

where the $r(\theta)$ is the distance from droplet center to its boundary in the direction of angle θ to the x axis. And we use 200 points as the perimeter for each droplet boundary with a equal angle interval from 0 to 2π. Fig. 7.10(a) shows the distribution of deformation in the hopper. Agreeing with Fig. 7.9(c), more large deformation distribute on the wall near the narrow end. To confirm the correlation between the two methods of stress quantification, we plot the largest contact length on a droplet as a function of its deformation for different data with various flux rates, as in Fig. 7.10(b)-(d). They all show that on average the droplets having larger shape deformation D tend to have larger contacts $l_{contact}$ with neighbors. This confirms the strong correlation between contacts and the shape deformation, and the droplet interaction could be quantified by either way. Therefore, droplet deformation is used to quantify stress in the later discussion.

To quantify the stress on macro scale, we obtain the averaged deformation in a large region. Given different velocities at different location of the hopper, we consider the temporal distribution of mean deformation at 3 sections along the channel in Fig.7.11. It shows that stress fluctuations exist in all sections, and sometimes large stress drops happen during short time. It confirms that even without static friction, the dense flow through hopper still have stress fluctuations, similar to that in frictional granular materials [23, 133]. And the large stress releases or fluctuations are also found in granular materials under shear [23, 133, 22, 131].

It is believed that the large energy release during the stress fluctuations may be related to the shear-induced plasticity. To quantify the fluctuations, we consider two aspects of the deformation drops: magnitude ΔD_{drop} and lag time Δt_{drop} [131], as shown in Fig. 7.11. In the landscope of temporal deformation, ΔD_{drop} is a deformation decrease from the local maxima to the local minima, and Δt_{drop} is the lag time during this drop. So to investigate the stress fluctuations during the whole movie, we plot Fig. 7.12, the probability distribution of deformation decrease ΔD_{drop} and lag time

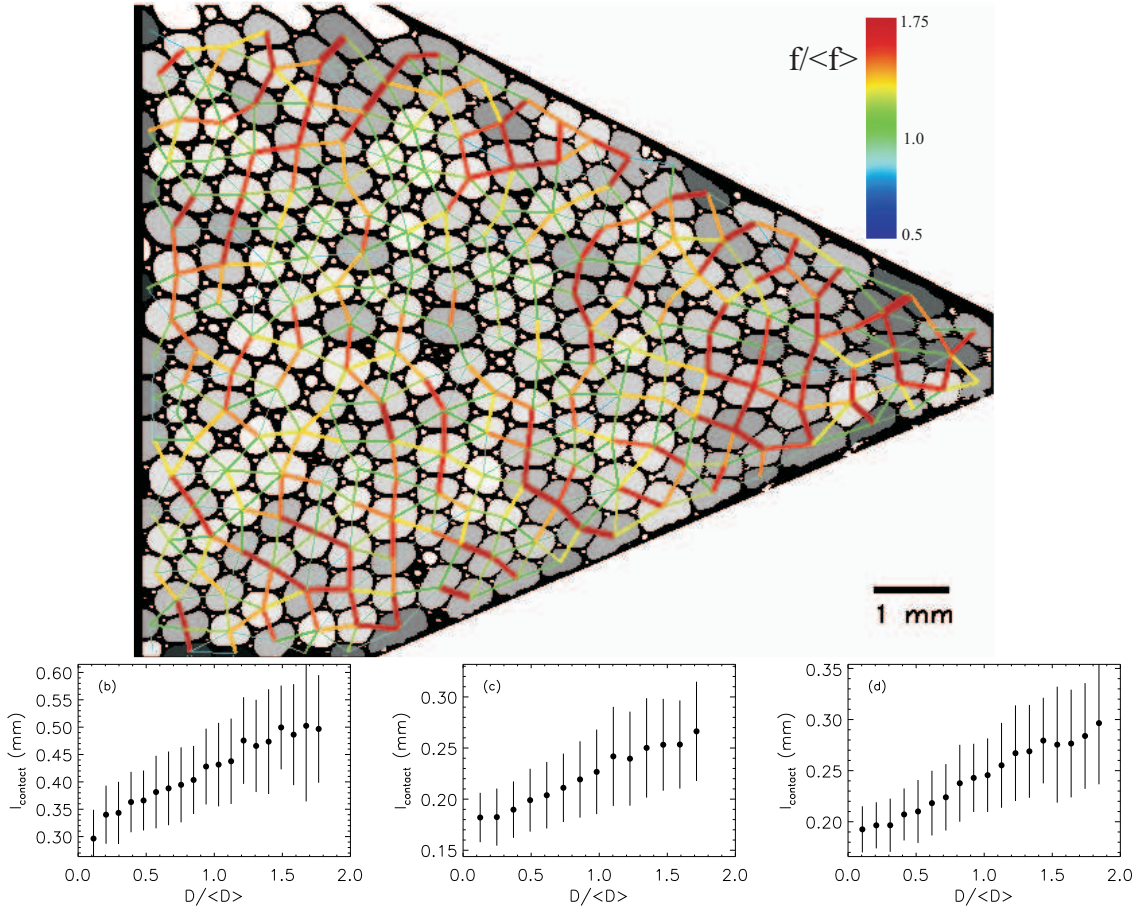

Figure 7.10: (a) The deformation distribution along the channel, overlapped with the forces in Fig. 7.9(c). Each droplet is shaded with a shade of gray corresponding to the deformation. The deformation ranges from 0 to 0.4, and the larger magnitude corresponds to the darker color. (b)-(d) Data 1, 6, and 5: The largest contact length $l_{contact}$ on a droplet as a function of its deformation D normalized by the mean $\langle D \rangle$. The vertical bars represent the standard deviation.

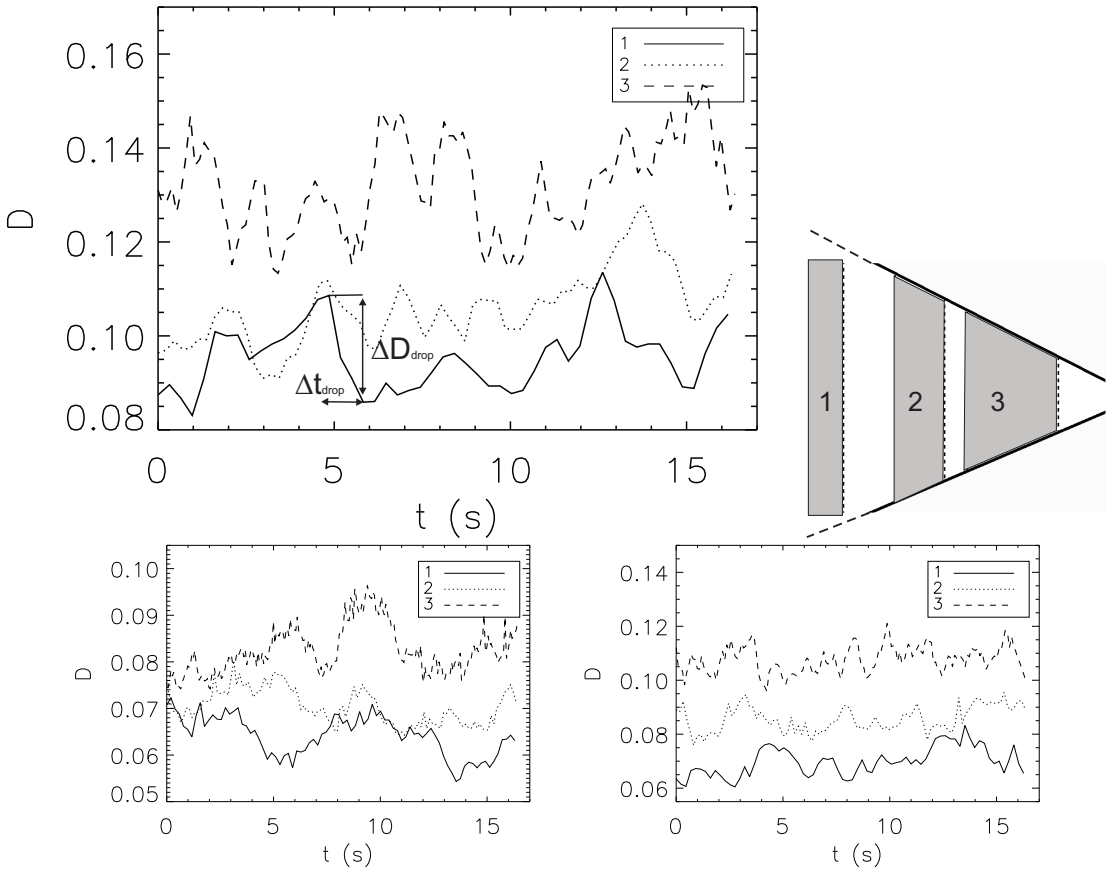

Figure 7.11: (a) Data 1: The deformation fluctuations at 3 sections along the channel as indicated in (b). The left region (solid line) has the widest gap ($\sim 19\langle d\rangle$, $\langle d\rangle = 0.48$ mm is mean droplet diameter). Due to the limitation of the image size, the region can not cover the whole part of the channel (dashed lines). The middle region (dots) has the gap of $\sim 13\langle d\rangle$. The right region (dashed line) has the narrowest gap of $\sim 7\langle d\rangle$. To reduce noise, the deformation is averaged over droplets in each region during a short time scale τ. To keep the same amount of droplets for the statistics in the different regions, we choose the time intervals τ inversely proportional to $\langle V_x\rangle_y(x)$ (0.33, 0.23, and 0.13 s), and select those regions with same amount of area. During the fluctuation, there are built-up events (increase in deformation) and release events (decrease in deformation). And to investigate stress fluctuations, we consider the deformation decrease ΔD_{drop} and lag time Δt_{drop} in each release event [131]. (c)-(d) The deformation fluctuations for the data 6 and 5.

Δt_{drop}. Given that the deformation is larger and flow rate is faster near the narrow region, the deformation D is normalized by the mean $\langle D \rangle$ in (a), and the lag time τ is scaled by the average time intervals $\bar{\tau}$ inversely proportional to V_x. The probability distributions in both graphs are roughly exponential. The decay constant for the are around $0.08\langle D \rangle$ and 2.1τ, which are insensitive to the time interval τ we choose. And in other data as shown in Fig. 7.12(c)-(f), the decay constant for D_{drop} is smaller for smaller flux rates, but no much difference to t_{drop} distribution. It suggests that larger flux rate could lead to larger deformation drops, but the temporal distribution should be the same. In addition, those graphs show that the distribution of stress drops in these regions are qualitatively same after the scaling, either in the deformation drop or lag time. It means that the statistics of the stress fluctuations are similar in the three regions, although the velocity and shear conditions are different. In the previous shear experiment on granular material [131] similar results are found, where the statistics of stress fluctuations distribution is found qualitatively same under different shear rates. All that suggests that the exponential decay in stress drops is not dependent much on shear rates or flow rates.

In addition, it is interesting to check the power spectrum of deformation fluctuations $D(t)$. Fig. 7.13 shows the power spectra for different regions. In this log-log plot, the straight line has a slope of -1. And at high frequency $\omega/2\pi > 0.1$ s^{-1}, the spectrum $P(\omega) \sim \omega^{-1}$, which holds for different regions with different shear rates. After scaled by the averaged deformation $\langle D \rangle$ at each regions, those spectra almost overlap to each other. And the similar power-law in stress fluctuation spectrum is also found in granular experiments [138].

7.2.4 Stress fluctuations vs. T1 event

As discussed above, the plasticity could be quantified either by stress fluctuations in macro scale, or by the T1 events in micro scale. Therefore, it is interesting to inves-

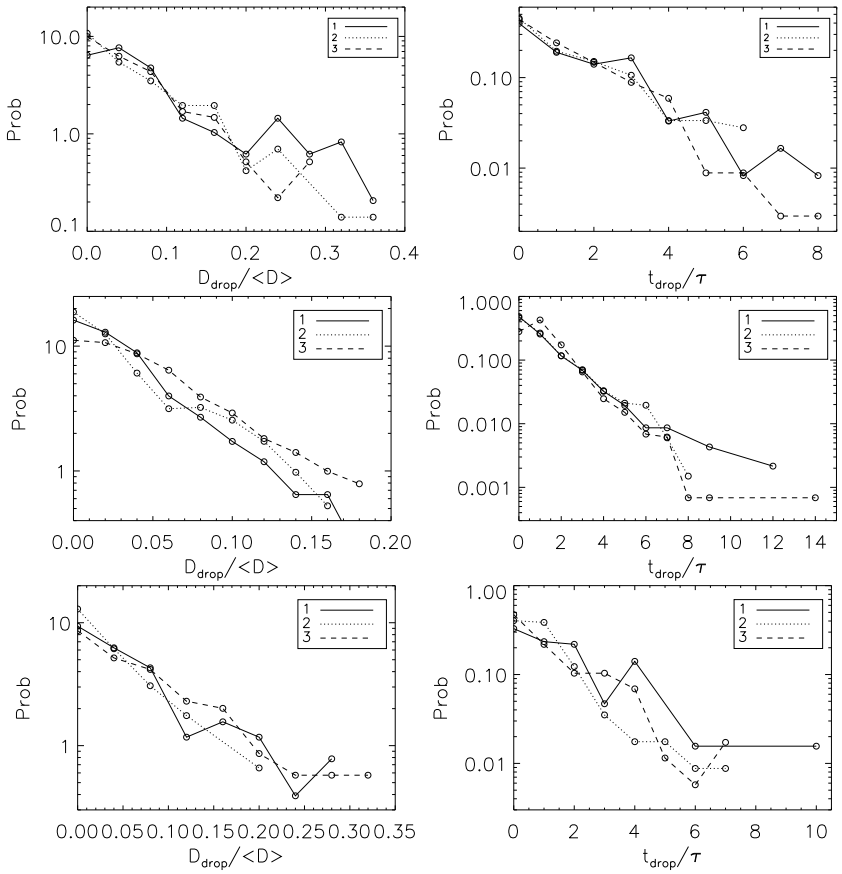

Figure 7.12: (a) Data 1: Probability distribution of deformation decrease ΔD_{drop} (a) and lag time Δt_{drop} (b) of stress fluctuations at 3 sections same as in Fig. 7.11: the left (solid line) with the widest gap of $\sim 19\langle d\rangle$, the middle (dots) with the gap of $\sim 13\langle d\rangle$, and the right (dashed line) with the narrowest gap of $\sim 7\langle d\rangle$. Given that the deformation is larger and flow rate is faster near the narrower region, the deformation D is normalized by the mean $\langle D\rangle$ in each region (a). And the lag time τ is scaled by time intervals $\tau = 0.33$, 0.23, and 0.13 s. The probability distributions in both graphs are roughly exponential with the decay constants around $0.08\langle D\rangle$ and 2.1τ. Both graphs are based on the statistics of 2700 droplets in a 200 s movie. (c)-(d): Similar analysis above for the data 6. The probability distributions in both graphs are also roughly exponential with the decay constants around $0.04\langle D\rangle$ and 1.8τ. (e)-(f): Similar analysis above for the data 5. The probability distributions in both graphs are also roughly exponential with the decay constants around $0.06\langle D\rangle$ and 1.7τ.

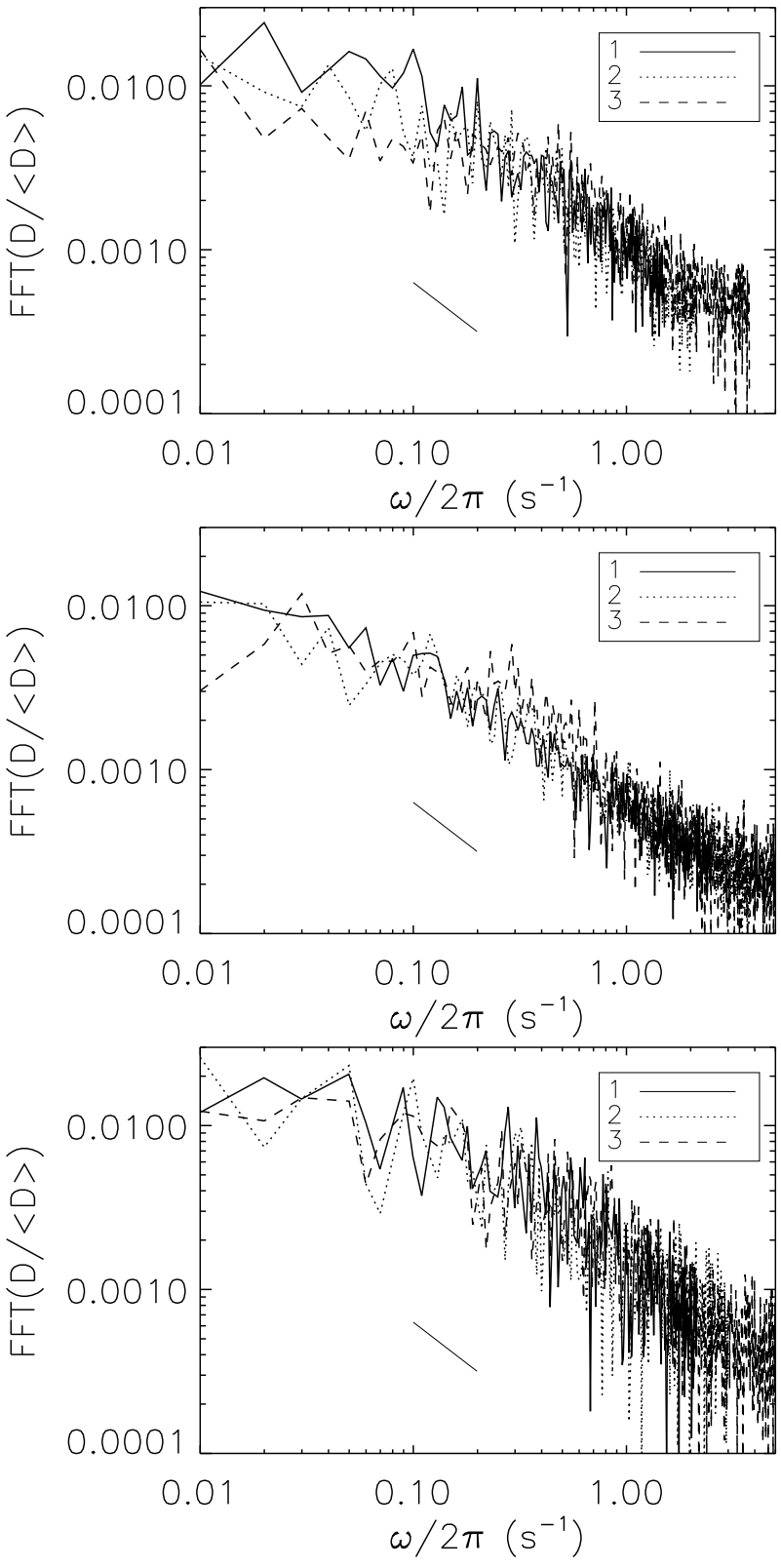

Figure 7.13: (a)-(c) Data 1, 6, and 5: The power spectrum for deformation fluctuation at the three regions as shown in Fig. 7.11(b). The straight line has a slope of -1.

tigate the relation between them. So we investigate both the temporal fluctuation of the deformation and the cumulative number of T1 events on the left side of the channel, as shown in Fig. 7.14 (a) and (b). It is found that during the period of large stress drops (4.3-6.3 s, and 12.9-14.2 s), T1 events happen more frequently. It suggests strong correlation between the stress fluctuations and the micro T1 rearrangements. To confirm the relation between large stress release and T1 frequency, we plot the Fig. 7.14(c), the averaged T1 frequency f_{T1} as a function of deformation drop D_{drop} normalized by the mean $\langle D_{drop} \rangle$. It confirms that during the large stress releases, T1 rearrangements tend to happen more frequently.

In addition, Fig. 7.15(a) shows the T1 particles during the time period 12.9-14.2 s in Fig. 7.14(b). It shows that those T1 events group together, forming a larger active region. This spatial correlation between T1s is confirmed in Fig. 7.15(b), the pair correlation function of T1 during short time scale $\tau = 2$ s when the flux only moves over one-droplet distance. The correlation peak at around one droplet diameter distance suggests that T1 events would trigger another T1 rearrangement among the neighbors in the next short period. And in this way, groups of T1s happen in the neighboring regions during short period. As shown in Fig. 7.15(c)-(d), this spatial correlation between T1 rearrangements can also found in other data with different flux rates.

For further investigation on the relation between deformation and T1 event, we take a look at one typical T1 event, and study how the deformation changes during the rearrangements. Fig. 7.16 shows the the deformation of the neighbor region around a T1 event before, in the middle, and after the rearrangement. During the rearrangement, the whole group of droplets only move over one-radius distance, but some neighbors have large deformation releases. It suggests that a micro T1 event could lead to stress relaxation in the neighbor region.

We do further statistics over 125 T1 events in the left region of the channel with the

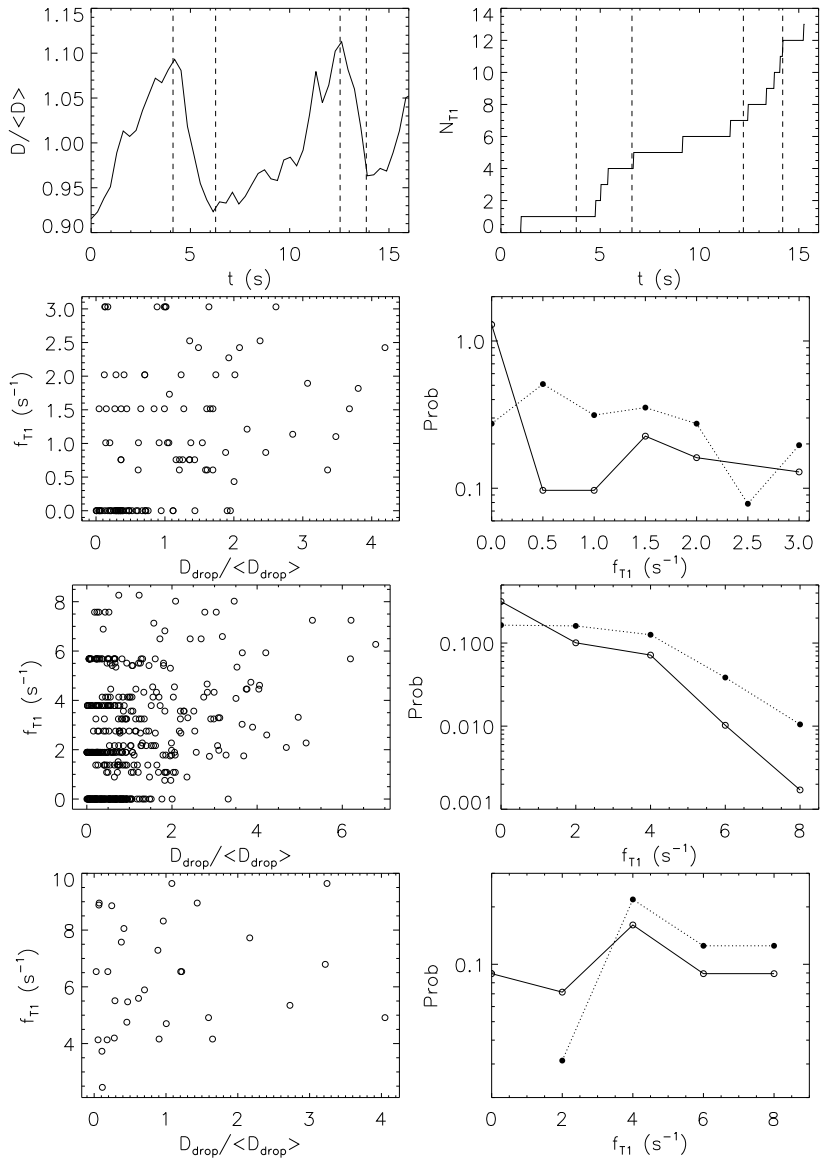

Figure 7.14: (a) Data 1: Deformation fluctuations of the left side of channel as shown in the inset. To reduce noise, the deformation averaged over a short time scale $\tau = 0.33$ s. The dash lines indicate two stress-release periods, during the time 4.3-6.3 s, and 12.9-14.2 s. (b) Data 1: Cumulative number of T1 events distributing over time in the same channel section and time period. The dash lines correspond to the same stress-release periods. (c) Data 1: T1 frequency f_{T1} vs. deformation drop D_{drop} for each drops. The linear correlation is 0.35. (d) Data 1: The probability distribution of f_{T1} for large drops $D > \langle D \rangle$ (dashed line) and for small drops $D < \langle D \rangle$ (solid line) (e)-(f) Data 6: similar analysis as in (c)-(d) for the data 1. The linear correlation between T1 frequency f_{T1} vs. deformation drop D_{drop} is 0.28. (g)-(h) Data 5: similar analysis as in (c)-(d) for the data 1. The linear correlation between T1 frequency f_{T1} vs. deformation drop D_{drop} is 0.27.

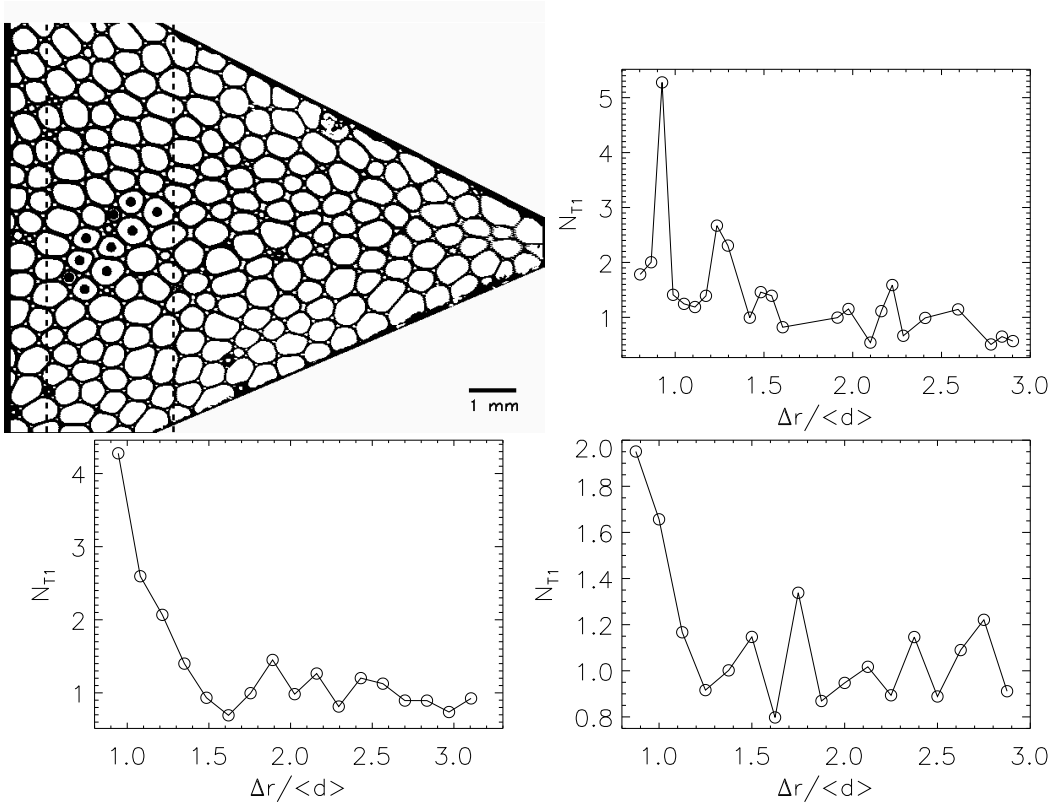

Figure 7.15: (a) T1 particles during the time period 12.5-13.9 s in Fig. 7.14(b). (b) Pair correlation of T1s during a short time interval $\tau = 2$ s in the region between the two dash lines. This function tells how many other T1s could be found at the distance of Δr from one T1 event. During such short time interval, the flux in this region only moves over one-droplet distance. The statistics is for 125 T1 events during a movie of 200 s. The x axis is the distance between T1s, normalized by mean droplet diameter $\langle d \rangle = 0.48$ mm. (c)-(d) The pair correlation functions of T1s for the 6 and 5.

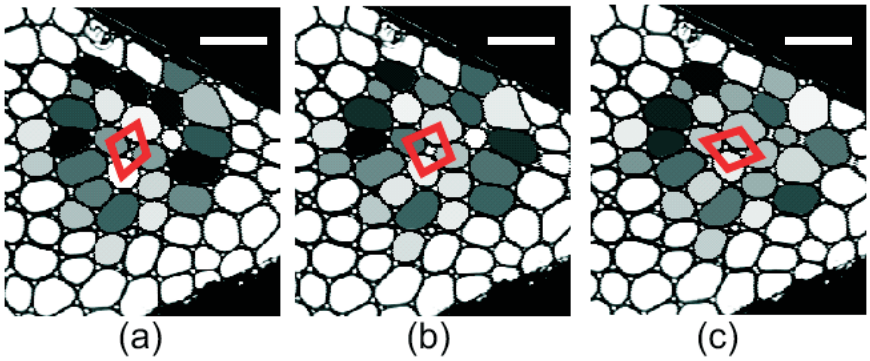

Figure 7.16: A typical example of deformation distribution before (a), in the middle (b), and after (c) a T1 rearrangement. The scale bar is 1 mm. The droplet deformation ranges from 0 to 0.18 with the filling color from white to black. The time period during this rearrangement is 0.4 s, where the droplet group only move over one-radius distance.

width of 20 droplet diameters. Fig. 7.17 is the 2D temporal and spatial distribution of deformation around T1 events. Deformation magnitude D close to the mean $\langle D \rangle$ is colored white. And larger than the mean is more red, the less than the mean is more blue. The x axis is the distance from T1 center to neighbor area, normalized by mean droplet diameter $\langle d \rangle = 0.48$ mm. The y axis is the lag time Δt from the T1 moment. The graph shows that when T1 rearrangement starts ($\Delta t = 0$), the stress is built up in a short time ($\sim$0.5 s) among the 4 T1 particles. But during the rearrangement, the stress is then quickly released with a large drop (from red to blue). The blue region range ~ 2 s in y (temporal) axis, and one droplet diameter in x (spatial) axis. It means that it takes a longer time for droplets to recover back to the average level, comparing to the time for the stress to built up. And this stress drop does not only happen between 4 T1 particles, but also affect their neighbors within 4 droplet radius distance. As shown in Fig. 7.17(b)-(c), this one-diameter spatial influence of T1 rearrangements can also found in other data with various flux rates. In addition, the flux rates of those data from (a), (b) to (c) are decreasing, which is $A_1 > A_5 > A_6$. But the blue or red area seem to extend longer along the y (time) axis. As mentioned in Fig. 7.14, the stress fluctuations can be scaled by longer time intervals under slower flow rates. And in the similar way, those T1 rearrangements appear longer at lower flux rates.

7.3 Discussion

By using 2D emulsion, we study both macroscopic stresses and microscopic dynamics in a dense flow passing through a hopper. Our first main observation is that under different flux rates, the flow profiles in a hopper are very similar. Our second main observation is that large temporal stress fluctuations in a large scale. We also find that at different locations of the same hopper, the stress fluctuations have similar

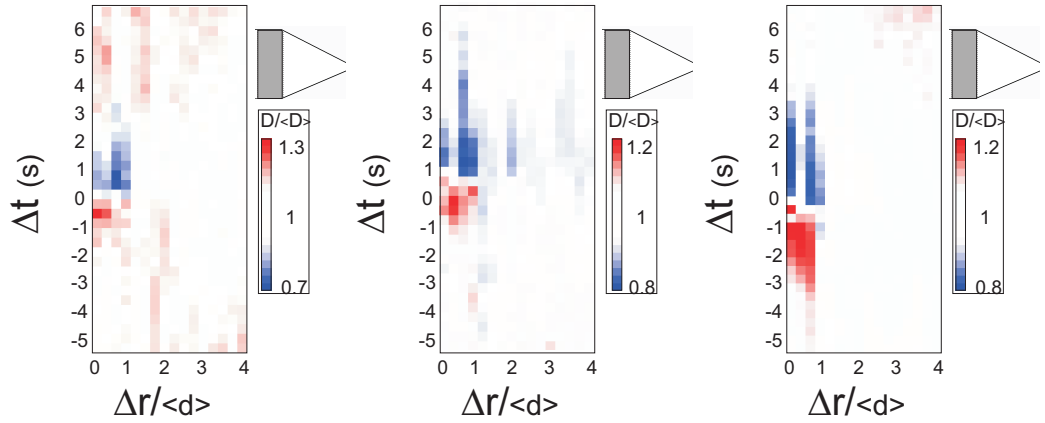

Figure 7.17: (a) Data 1: 2D temporal and spatial distribution of deform around T1 events happening in the left side of the channel with width of 20 droplet diameters ($w(x) \sim 20\langle d \rangle$). The map averages over 125 T1 events during a movie of 200 s. As shown in the color bar, deformation magnitude D close to the mean $\langle D \rangle$ is colored white. And larger than the mean is more red, the less than the mean is more blue. The x axis is the distance from T1 center to neighbor area, normalized by droplet mean droplet diameter $\langle d \rangle = 0.48$ mm. The y axis is the lag time Δt from the T1 moment. (b) Data 5: 2D temporal and spatial distribution of deform around T1 events, similar to (a) for the data 1. (c) Data 6: 2D temporal and spatial distribution of deform around T1 events, similar to (a) for the data 1.

probability distribution after scaling by the flow speed. Our third main observation is that local neighbor rearrangements ("T1 events") are related to macroscopic stress fluctuations. We find individual T1 events can lead to large local stress release among their neighbors within one diameter distance. And for the stress fluctuation in a large scale, T1 events tend to happen more frequently during large stress drops. Our analysis of this emulsion system shows a direct and local relationship between rearrangements and stress fluctuations. In addition, by comparing with granular shear experiments [22, 130, 131, 23, 133], we find some similar properties of stress fluctuations during the flow. It suggests to us that those could be the common characteristics of complex fluid under shear for both frictionless and frictional systems.

Chapter 8

Summary and outlook

8.1 Summary

My work in our lab is studying the shear induced transition of jammed materials from solid-like state to fluid-like state. The hallmark of the jammed materials is that they could resist applied stress or shear, but have an disordered structure like liquid. When the stress or shear is over a yielding point, the original structure could no longer hold, and the material starts to flow in a unjammed fluid state. This process involves two disparate features of the materials: force distribution on structure (force chain), and particles' moving in yielded flow (micro dynamics).

In Chapter 4 [43], I use 3D colloidal system to study micro dynamics of a jammed material under large shear strains. Motivated by the shear-transformation-zone theory ("STZ") [8], I quantify the plasticity through particle motions. I find the spatial distribution of the plastic rearrangements is heterogeneous, where active particles tend to group in local regions. In addition, although the shear is happening in a particular direction, I find those the local plastic regions do not have obvious directional bias in the disordered materials.

To probe another feature of jammed materials, the force distribution, I use 2D emulsion droplets in Chapter 7. This 2D system allows us study not only droplet in-

teractions but also their dynamics as well. Therefore, I focus on the inter-connection between the forces and the dynamics. I find the micro plastic dynamics("T1 event") is directly related to the macro stress releases (avalanches). An individual "T1" rearrangement can lead to large stress release in neighbors. And these plastic rearrangements tend to group together, leading to larger stress changes in a longer length scale. Therefore the large stress changes inside the jammed materials could eventually propagate onto the wall, which is detected as stress fluctuations or avalanches in the macro flow behavior.

By comparing the two projects, some methods of analysis are similar. For example, in both experiments, I study the "nonaffine motion", the deviation from the averaged flow profiles. The nonaffine rearrangements reflect structural changes in local area. And in both experiments, we find that those large nonaffine motions come from large shear strains. But I probe these micro-dynamics from slight different perspectives in the two experiments. In the emulsion experiment, I investigate the relation between macroscopic stresses and microscopic nonaffine motions, which are specified as "T1 events". While in the colloid experiment, I focus more on the extension of the micro-dynamic regions in the 3D space. By combining those two, I can have a better understanding of the physics behind the "plasticity": it distributes heterogeneously in space but with no directional bias; and it leads to large stress fluctuations in the macro scale.

8.2 Outlook

Basing on those results, one of the hypothesis I would like to propose for the future experiments is: when shearing "3D" emulsion droplets, we can see the isotropic plastic rearrangements, as well as the large stress fluctuations from those regions. This experiment combines my two experiments above, and provide new perspectives for

understanding "plasticity". If the active rearranging regions are not isotropic, we could argue that the situation for hard-sphere colloids and soft droplets are different. If we did not see the large fluctuations from the active regions, we could say the geometry changes, from 2D to 3D, may be important for plastic flow. In addition, this experiment could be conducted in the exact same shear cell as in the colloidal experiment. So in practice, the experimental setup should be easy and quick, although droplet tracking and stress calculation could be challenging.

There may be other interesting experiments by modifying the experimental setup a little bit. One is to develop the 2D emulsion systems with different geometries besides the hopper. With the help of the soft lithography, we could make different shapes of 2D channels, and we could compare the dynamic-stress relation between different geometries. Besides, rather than the flux rate, we could also control the pressure of flow by using the air regulator. We could see if there are any difference in the stress fluctuations or dynamics.

In addition, we can also slightly change the properties of samples. For example, the concentration or the polydispersity is important for jammed materials in the static state. And those properties could make a difference to the response to shearing. So it is interesting to repeat my experiments with the same setups but use the samples with different concentration or polydispersity. One concern for larger polydispersity is the tracking could be harder, since the inter-image distance should be less than the minimum size of particles. After all, all those experiments mentioned above could lead to a better understanding of "plasticity" in jammed materials.

Bibliography

[1] R. A. L. Jones. *Soft Condensed Matter* (Oxford University Press) (2002).

[2] A. J. Liu & S. R. Nagel. "Nonlinear dynamics: Jamming is not just cool any more." *Nature*, **396**, 21–22 (1998).

[3] K. To, P. Y. Lai, & H. K. Pak. "Jamming of granular flow in a two-dimensional hopper." *Phys. Rev. Lett.*, **86**, 71–74 (2001).

[4] J. Zhou, S. Long, Q. Wang, & A. D. Dinsmore. "Measurement of forces inside a three-dimensional pile of frictionless droplets." *Science*, **312**, 1631–1633 (2006).

[5] H. M. Jaeger, S. R. Nagel, & R. P. Behringer. "Granular solids, liquids, and gases." *Reviews of Modern Physics*, **68**, 1259–1273 (1996).

[6] I. K. Ono, C. S. O'Hern, D. J. Durian, S. A. Langer, A. J. Liu, & S. R. Nagel. "Effective temperatures of a driven system near jamming." *Phys. Rev. Lett.*, **89**, 095703 (2002).

[7] P. Hébraud, F. Lequeux, J. P. Munch, & D. J. Pine. "Yielding and rearrangements in disordered emulsions." *Phys. Rev. Lett.*, **78**, 4657–4660 (1997).

[8] M. L. Falk & J. S. Langer. "Dynamics of viscoplastic deformation in amorphous solids." *Phys. Rev. E*, **57**, 7192 (1998).

[9] P. Schall, D. A. Weitz, & F. Spaepen. "Structural rearrangements that govern flow in colloidal glasses." *Science*, **318**, 1895–1899 (2007).

[10] A. J. Liu & N. S. R. *Jamming and Rheology* (Taylor and Francis) (2001).

[11] G. Adam & J. H. Gibbs. "On the temperature dependence of cooperative relaxation properties in glass-forming liquids." *J. Chem. Phys.*, **43**, 139–146 (1965).

[12] C. Donati, J. F. Douglas, W. Kob, S. J. Plimpton, P. H. Poole, & S. C. Glotzer. "Stringlike cooperative motion in a supercooled liquid." *Phys. Rev. Lett.*, **80**, 2338 (1998).

[13] E. R. Weeks, J. C. Crocker, A. C. Levitt, A. Schofield, & D. A. Weitz. "Three-dimensional direct imaging of structural relaxation near the colloidal glass transition." *Science*, **287**, 627–631 (2000).

[14] W. K. Kegel & A. van Blaaderen. "Direct observation of dynamical heterogeneities in colloidal hard-sphere suspensions." *Science*, **287**, 290–293 (2000).

[15] M. D. Ediger. "Spatially heterogeneous dynamics in supercooled liquids." *Annu. Rev. Phys. Chem.*, **51**, 99–128 (2000).

[16] D. Weaire, J. D. Barry, & S. Hutzler. "The continuum theory of shear localization in two-dimensional foam." *J. Phys.: Cond. Matt.*, **22**, 193101 (2010).

[17] M. Dennin & C. M. Knobler. "Experimental studies of bubble dynamics in a slowly driven monolayer foam." *Phys. Rev. Lett.*, **78**, 2485–2488 (1997).

[18] A. M. Kraynik. "Foam flows." *Annual Review of Fluid Mechanics*, **20**, 325–357 (1988).

[19] T. S. Majmudar & R. P. Behringer. "Contact force measurements and stress-induced anisotropy in granular materials." *Nature*, **435**, 1079–1082 (2005).

[20] M. van Hecke. "Granular matter: A tale of tails." *Nature*, **435**, 1041–1042 (2005).

[21] D. M. Mueth, H. M. Jaeger, & S. R. Nagel. "Force distribution in a granular medium." *Phys. Rev. E*, **57**, 3164 (1998).

[22] D. Howell, R. P. Behringer, & C. Veje. "Stress fluctuations in a 2d granular couette experiment: A continuous transition." *Phys. Rev. Lett.*, **82**, 5241–5244 (1999).

[23] E. Longhi, N. Easwar, & N. Menon. "Large force fluctuations in a flowing granular medium." *Phys. Rev. Lett.*, **89**, 045501 (2002).

[24] C. S. O'Hern, L. E. Silbert, A. J. Liu, & S. R. Nagel. "Jamming at zero temperature and zero applied stress: The epitome of disorder." *Phys. Rev. E*, **68**, 011306 (2003).

[25] J. Bruji, S. Fedwards, I. Hopkinson, & H. Makse. "Measuring the distribution of interdroplet forces in a compressed emulsion system." *Physica A: Statistical Mechanics and its Applications*, **327**, 201–212 (2003).

[26] L. Antl, J. W. Goodwin, R. D. Hill, R. H. Ottewill, S. M. Owens, S. Papworth, & J. A. Waters. "The preparation of poly(methyl methacrylate) latices in non-aqueous media." *Colloids Surf.*, **17**, 67–78 (1986).

[27] G. Bosma. "Preparation of monodisperse, fluorescent pmma latex colloids by dispersion polymerization." *J. Colloid Interf. Sci.*, **245**, 292–300 (2002).

[28] R. P. A. Dullens, Claesson, D. Derks, A. van Blaaderen, & W. K. Kegel. "Monodisperse core shell poly(methyl methacrylate) latex colloids." *Langmuir*, **19**, 5963–5966 (2003).

[29] A. I. Campbell & P. Bartlett. "Fluorescent hard-sphere polymer colloids for confocal microscopy." *J. Colloid Interf. Sci.*, **256**, 325–330 (2002).

[30] P. N. Pusey & W. van Megen. "Phase behaviour of concentrated suspensions of nearly hard colloidal spheres." *Nature*, **320**, 340–342 (1986).

[31] V. Prasad, D. Semwogerere, & E. R. Weeks. "Confocal microscopy of colloids." *J. Phys.: Cond. Matt.*, **19**, 113102 (2007).

[32] W. van Megen & P. N. Pusey. "Dynamic light-scattering study of the glass transition in a colloidal suspension." *Phys. Rev. A*, **43**, 5429 (1991).

[33] R. J. Speedy. "The hard sphere glass transition." *Mol. Phys.*, **95**, 169–178 (1998).

[34] G. Brambilla, D. E. Masri, M. Pierno, L. Berthier, L. Cipelletti, G. Petekidis, & A. B. Schofield. "Probing the equilibrium dynamics of colloidal hard spheres above the mode-coupling glass transition." *Phys. Rev. Lett.*, **102**, 085703 (2009).

[35] J. D. Bernal. "The bakerian lecture, 1962. the structure of liquids." *Proc. Roy. Soc. London. Series A*, **280**, 299–322 (1964).

[36] S. Torquato, T. M. Truskett, & P. G. Debenedetti. "Is random close packing of spheres well defined?" *Phys. Rev. Lett.*, **84**, 2064–2067 (2000).

[37] A. Donev, S. Torquato, F. H. Stillinger, & R. Connelly. "Comment on ıjamming at zero temperature and zero applied stress: The epitome of disorderȷ." *Phys. Rev. E*, **70**, 043301 (2004).

[38] C. S. O'Hern, L. E. Silbert, A. J. Liu, & S. R. Nagel. "Reply to "comment on 'jamming at zero temperature and zero applied stress: The epitome of disorder' "." *Phys. Rev. E*, **70**, 043302 (2004).

[39] A. D. Dinsmore, E. R. Weeks, V. Prasad, A. C. Levitt, & D. A. Weitz. "Three-dimensional confocal microscopy of colloids." *Appl. Opt.*, **40**, 4152–4159 (2001).

[40] J. C. Crocker & D. G. Grier. "Methods of digital video microscopy for colloidal studies." *J. Colloid Interf. Sci.*, **179**, 298–310 (1996).

[41] S. Topp, V. Prasad, G. C. Cianci, E. R. Weeks, & J. P. Gallivan. "A genetic toolbox for creating reversible Ca^{2+}-sensitive materials." *Journal of the American Chemical Society*, **128**, 13994–13995 (2006).

[42] R. Besseling, L. Isa, E. Weeks, & W. Poon. "Quantitative imaging of colloidal flows." *Adv. Colloid Interface Sci.*, **146**, 1–17 (2009).

[43] D. Chen, D. Semwogerere, J. Sato, V. Breedveld, & E. R. Weeks. "Microscopic structural relaxation in a sheared supercooled colloidal liquid." *Phys. Rev. E*, **81**, 011403 (2010).

[44] C. A. Angell, K. L. Ngai, G. B. McKenna, P. F. McMillan, & S. W. Martin. "Relaxation in glassforming liquids and amorphous solids." *J. App. Phys.*, **88**, 3113–3157 (2000).

[45] P. Coussot & F. Gaulard. "Gravity flow instability of viscoplastic materials: The ketchup drip." *Phys. Rev. E*, **72**, 031409 (2005).

[46] J. Ubbink, A. Burbidge, & R. Mezzenga. "Food structure and functionality: a soft matter perspective." *Soft Matter*, **4**, 1569–1581 (2008).

[47] R. Mezzenga, P. Schurtenberger, A. Burbidge, & M. Michel. "Understanding foods as soft materials." *Nature Mater.*, **4**, 729–740 (2005).

[48] P. Coussot, J. S. Raynaud, F. Bertrand, P. Moucheront, J. P. Guilbaud, H. T. Huynh, S. Jarny, & D. Lesueur. "Coexistence of liquid and solid phases in flowing soft-glassy materials." *Phys. Rev. Lett.*, **88**, 218301 (2002).

[49] N. Huang, G. Ovarlez, F. Bertrand, S. Rodts, P. Coussot, & D. Bonn. "Flow of wet granular materials." *Phys. Rev. Lett.*, **94**, 028301 (2005).

[50] F. S. Merkt, R. D. Deegan, D. I. Goldman, E. C. Rericha, & H. L. Swinney. "Persistent holes in a fluid." *Phys. Rev. Lett.*, **92**, 184501 (2004).

[51] F. Spaepen. "A microscopic mechanism for steady state inhomogeneous flow in metallic glasses." *Acta Metallurgica*, **25**, 407–415 (1977).

[52] H. W. Sheng, H. Z. Liu, Y. Q. Cheng, J. Wen, P. L. Lee, W. K. Luo, S. D. Shastri, & E. Ma. "Polyamorphism in a metallic glass." *Nat Mater*, **6**, 192–197 (2007).

[53] C. A. Schuh, T. C. Hufnagel, & U. Ramamurty. "Mechanical behavior of amorphous alloys." *Acta Materialia*, **55**, 4067–4109 (2007).

[54] M. D. Haw. "Colloidal suspensions, brownian motion, molecular reality: a short history." *J. Phys.: Cond. Matt.*, **14**, 7769–7779 (2002).

[55] S. Suresh. "Crystal deformation: Colloid model for atoms." *Nat Mater*, **5**, 253–254 (2006).

[56] P. Habdas & E. Weeks. "Video microscopy of colloidal suspensions and colloidal crystals." *Curr. Opin. in Colloid & Interface Science*, **7**, 196–203 (2002).

[57] M. S. Elliot & W. C. K. Poon. "Conventional optical microscopy of colloidal suspensions." *Adv. in Colloid Interface Sci.*, **92**, 133–194 (2001).

[58] A. van Blaaderen & P. Wiltzius. "Real-space structure of colloidal hard-sphere glasses." *Science*, **270**, 1177–1179 (1995).

[59] W. van Megen & S. M. Underwood. "Dynamic-light-scattering study of glasses of hard colloidal spheres." *Phys. Rev. E*, **47**, 248–261 (1993).

[60] W. van Megen & S. M. Underwood. "Glass transition in colloidal hard spheres: Measurement and mode-coupling-theory analysis of the coherent intermediate scattering function." *Phys. Rev. E*, **49**, 4206–4220 (1994).

[61] I. Snook, W. van Megen, & P. Pusey. "Structure of colloidal glasses calculated by the molecular-dynamics method and measured by light scattering." *Phys. Rev. A*, **43**, 6900–6907 (1991).

[62] E. Bartsch, V. Frenz, S. Moller, & H. Sillescu. "Colloidal polystyrene micronetwork spheres a new mesoscopic model of the glass transition in simple liquids." *Physica A*, **201**, 363–371 (1993).

[63] E. Bartsch. "Scattering experiments for the microscopic understanding of the glass transition." *J. Non-Cryst. Solids*, **192-193**, 384–392 (1995).

[64] T. G. Mason & D. A. Weitz. "Linear viscoelasticity of colloidal hard sphere suspensions near the glass transition." *Phys. Rev. Lett.*, **75**, 2770–2773 (1995).

[65] J. Goyon, A. Colin, G. Ovarlez, A. Ajdari, & L. Bocquet. "Spatial cooperativity in soft glassy flows." *Nature*, **454**, 84–87 (2008).

[66] L. Bocquet, A. Colin, & A. Ajdari. "Kinetic theory of plastic flow in soft glassy materials." *Phys. Rev. Lett.*, **103**, 036001 (2009).

[67] R. Yamamoto & A. Onuki. "Nonlinear rheology of a highly supercooled liquid." *Europhys. Lett.*, **40**, 61–66 (1997).

[68] K. Miyazaki, D. R. Reichman, & R. Yamamoto. "Supercooled liquids under shear: Theory and simulation." *Phys. Rev. E*, **70**, 011501 (2004).

[69] R. Besseling, E. R. Weeks, A. B. Schofield, & W. C. K. Poon. "Three-dimensional imaging of colloidal glasses under steady shear." *Phys. Rev. Lett.*, **99**, 028301 (2007).

[70] K. Maeda & S. Takeuchi. "Atomistic process of plastic deformation in a model amorphous metal." *Phil. Mag. A*, **44**, 643–656 (1981).

[71] Y. Shi & M. L. Falk. "Strain localization and percolation of stable structure in amorphous solids." *Phys. Rev. Lett.*, **95**, 095502 (2005).

[72] Z. Cheng, J. Zhu, P. M. Chaikin, S.-E. Phan, & W. B. Russel. "Nature of the divergence in low shear viscosity of colloidal hard-sphere dispersions." *Phys. Rev. E*, **65**, 041405 (2002).

[73] Y. Wang, K. Krishan, & M. Dennin. "Bubble kinematics in a sheared foam." *Phys. Rev. E*, **74**, 041405 (2006).

[74] B. Utter & R. P. Behringer. "Experimental measures of affine and nonaffine deformation in granular shear." *Phys. Rev. Lett.*, **100**, 208302 (2008).

[75] G. Petekidis, A. Moussaïd, & P. N. Pusey. "Rearrangements in hard-sphere glasses under oscillatory shear strain." *Phys. Rev. E*, **66**, 051402 (2002).

[76] M. D. Haw, W. C. K. Poon, & P. N. Pusey. "Direct observation of oscillatory-shear-induced order in colloidal suspensions." *Phys. Rev. E*, **57**, 6859 (1998).

[77] N. Duff & D. J. Lacks. "Shear-induced crystallization in jammed systems." *Phys. Rev. E*, **75**, 031501 (2007).

[78] U. Gasser, E. R. Weeks, A. Schofield, P. N. Pusey, & D. A. Weitz. "Real-space imaging of nucleation and growth in colloidal crystallization." *Science*, **292**, 258–262 (2001).

[79] J. Hernández-Guzmán & E. R. Weeks. "The equilibrium intrinsic crystal liquid interface of colloids." *Proc. Natl. Acad. Sci.*, **106**, 15198–15202 (2009).

[80] R. P. A. Dullens, D. G. A. L. Aarts, & W. K. Kegel. "Dynamic broadening of the crystal-fluid interface of colloidal hard spheres." *Phys. Rev. Lett.*, **97**, 228301 (2006).

[81] P. R. ten Wolde, M. J. Ruiz-Montero, & D. Frenkel. "Numerical calculation of the rate of crystal nucleation in a Lennard-Jones system at moderate undercooling." *J. Chem. Phys.*, **104**, 9932–9947 (1996).

[82] P. J. Steinhardt, D. R. Nelson, & M. Ronchetti. "Bond-orientational order in liquids and glasses." *Phys. Rev. B*, **28**, 784–805 (1983).

[83] A. Van Blaaderen, A. Imhof, W. Hage, & A. Vrij. "Three-dimensional imaging of submicrometer colloidal particles in concentrated suspensions using confocal scanning laser microscopy." *Langmuir*, **8**, 1514–1517 (1992).

[84] L. T. Shereda, R. G. Larson, & M. J. Solomon. "Local stress control of spatiotemporal ordering of colloidal crystals in complex flows." *Phys. Rev. Lett.*, **101**, 038301 (2008).

[85] C.-L. Chan, W.-Y. Woon, & Lin. "Shear banding in mesoscopic dusty plasma liquids." *Phys. Rev. Lett.*, **93**, 220602 (2004).

[86] J. Lauridsen, G. Chanan, & M. Dennin. "Velocity profiles in slowly sheared bubble rafts." *Phys. Rev. Lett.*, **93**, 018303 (2004).

[87] I. Cohen, B. Davidovitch, A. B. Schofield, M. P. Brenner, & D. A. Weitz. "Slip, yield, and bands in colloidal crystals under oscillatory shear." *Phys. Rev. Lett.*, **97**, 215502 (2006).

[88] A. Lemaître & C. Caroli. "Plastic response of a two-dimensional amorphous solid to quasistatic shear: Transverse particle diffusion and phenomenology of dissipative events." *Phys. Rev. E*, **76**, 036104 (2007).

[89] C. E. Maloney & M. O. Robbins. "Evolution of displacements and strains in sheared amorphous solids." *J. Phys.: Cond. Matt.*, **20**, 244128 (2008).

[90] E. R. Weeks & D. A. Weitz. "Properties of cage rearrangements observed near the colloidal glass transition." *Phys. Rev. Lett.*, **89**, 095704 (2002).

[91] F. Delogu. "Atomic mobility and strain localization in amorphous metals." *Phys. Rev. Lett.*, **100**, 075901 (2008).

[92] D. J. Pine, J. P. Gollub, J. F. Brady, & A. M. Leshansky. "Chaos and threshold for irreversibility in sheared suspensions." *Nature*, **438**, 997–1000 (2005).

[93] C. Eisenmann, C. Kim, J. Mattsson, & D. A. Weitz. "Shear melting of a colloidal glass." *Phys. Rev. Lett.*, **104**, 035502 (2010).

[94] A. Tanguy, F. Leonforte, & J. Barrat. "Plastic response of a 2d Lennard-Jones amorphous solid: Detailed analysis of the local rearrangements at very slow strain rate." *Eur. Phys. J. E*, **20**, 355–364 (2006).

[95] E. R. Weeks, J. C. Crocker, & D. A. Weitz. "Short and long-range correlated motion observed in colloidal glasses and liquids." *J. Phys.: Cond. Matt.*, **19**, 205131 (2007).

[96] J. C. Crocker, M. T. Valentine, E. R. Weeks, T. Gisler, P. D. Kaplan, A. G. Yodh, & D. A. Weitz. "Two-point microrheology of inhomogeneous soft materials." *Phys. Rev. Lett.*, **85**, 888 (2000).

[97] B. Doliwa & A. Heuer. "Cooperativity and spatial correlations near the glass transition: Computer simulation results for hard spheres and disks." *Phys. Rev. E*, **61**, 6898–6908 (2000).

[98] M. D. Ediger, C. A. Angell, & S. R. Nagel. "Supercooled liquids and glasses." *J. Phys. Chem.*, **100**, 13200–13212 (1996).

[99] A. Mehta, G. C. Barker, & J. M. Luck. "Heterogeneities in granular dynamics." *Proc. Nat. Acad. Sci.*, **105**, 8244–8249 (2008).

[100] D. I. Goldman & H. L. Swinney. "Signatures of glass formation in a fluidized bed of hard spheres." *Phys. Rev. Lett.*, **96**, 145702 (2006).

[101] L. D. Landau & L. E. M. *Theory of Elasticity, Course of Theoretical Physics*, volume 7 (Butterworth-Heinemann), 3rd edition (1986).

[102] R. Yamamoto & A. Onuki. "Heterogeneous diffusion in highly supercooled liquids." *Phys. Rev. Lett.*, **81**, 4915 (1998).

[103] L. Berthier. "Time and length scales in supercooled liquids." *Phys. Rev. E*, **69** (2004).

[104] R. E. Courtland & E. R. Weeks. "Direct visualization of ageing in colloidal glasses." *J. Phys.: Cond. Matt.*, **15**, 359–365 (2003).

[105] V. K. Lee, W. Kob, K. Binder, & A. Zippelius. "Dynamical heterogeneities below the glass transition." *J. Chem. Phys.*, **116**, 5158–5166 (2002).

[106] J. D. Stevenson, J. Schmalian, & P. G. Wolynes. "The shapes of cooperatively rearranging regions in glass-forming liquids." *Nat. Phys.*, **2**, 268–274 (2006).

[107] T. Kawasaki, T. Araki, & H. Tanaka. "Correlation between dynamic heterogeneity and medium-range order in two-dimensional glass-forming liquids." *Phys. Rev. Lett.*, **99** (2007).

[108] J. C. Conrad, P. P. Dhillon, E. R. Weeks, D. R. Reichman, & D. A. Weitz. "Contribution of slow clusters to the bulk elasticity near the colloidal glass transition." *Phys. Rev. Lett.*, **97**, 265701 (2006).

[109] A. Furukawa, K. Kim, S. Saito, & H. Tanaka. "Anisotropic cooperative structural rearrangements in sheared supercooled liquids." *Phys. Rev. Lett.*, **102**, 016001 (2009).

[110] B. J. Ackerson & P. N. Pusey. "Shear-induced order in suspensions of hard spheres." *Phys. Rev. Lett.*, **61**, 1033–1036 (1988).

[111] B. J. Ackerson. "Shear induced order of hard sphere suspensions." *J. Phys.: Cond. Matt.*, **2**, 389–392 (1990).

[112] M. D. Haw, W. C. K. Poon, P. N. Pusey, P. Hebraud, & F. Lequeux. "Colloidal glasses under shear strain." *Phys. Rev. E*, **58**, 4673–4682 (1998).

[113] R. Shah, H. Shum, A. Rowat, D. Lee, J. Agresti, A. Utada, L. Chu, J. Kim, A. Fernandeznieves, & C. Martinez. "Designer emulsions using microfluidics." *Materials Today*, **11**, 18–27 (2008).

[114] D. R. Link, S. L. Anna, D. A. Weitz, & H. A. Stone. "Geometrically mediated breakup of drops in microfluidic devices." *Phys. Rev. Lett.*, **92**, 054503 (2004).

[115] H. A. Stone, A. D. Stroock, & A. Ajdari. "Engineering flows in small devices." *Annu. Rev. Fluid Mech.*, **36**, 381–411 (2004).

[116] Y. Xia & G. M. Whitesides. "Soft lithography." *Annual Review of Materials Science*, **28**, 153–184 (1998).

[117] M. L. Yarmush & K. R. King. "Living-cell microarrays." *Annual Review of Biomedical Engineering*, **11**, 235–257 (2009).

[118] A. Gervois, L. Oger, P. Richard, & J. Troadec. "Voronoi and radical tessellations of packings of spheres." In "Computational Science â ICCS 2002," volume 2331, pages 95–104 (Springer Berlin / Heidelberg, Berlin, Heidelberg) (2002).

[119] H. Telley, T. M. Liebling, & A. Mocellin. "The Laguerre model of grain growth in two dimensions i. cellular structures viewed as dynamical Laguerre tessellations." *Phil. Mag. Part B*, **73**, 395–408 (1996).

[120] B. Gellatly. "Characterisation of models of multicomponent amorphous metals: The radical alternative to the voronoi polyhedron." *J. Non-Cryst. Solids*, **50**, 313–329 (1982).

[121] C. H. Liu & S. R. Nagel. "Sound in sand." *Phys. Rev. Lett.*, **68**, 2301–2304 (1992).

[122] C. H. Liu & S. R. Nagel. "Sound in a granular material: Disorder and nonlinearity." *Phys. Rev. B*, **48**, 15646–15650 (1993).

[123] C. H. Liu. "Spatial patterns of sound propagation in sand." *Phys. Rev. B*, **50**, 782–794 (1994).

[124] A. Ngadi & J. Rajchenbach. "Intermittencies in the compression process of a model granular medium." *Phys. Rev. Lett.*, **80**, 273–276 (1998).

[125] E. Pratt & M. Dennin. "Nonlinear stress and fluctuation dynamics of sheared disordered wet foam." *Phys. Rev. E*, **67**, 051402 (2003).

[126] A. Abd el Kader & J. C. Earnshaw. "Shear-induced changes in two-dimensional foam." *Phys. Rev. Lett.*, **82**, 2610 (1999).

[127] G. Debrégeas, H. Tabuteau, & J. M. di Meglio. "Deformation and flow of a two-dimensional foam under continuous shear." *Phys. Rev. Lett.*, **87**, 178305 (2001).

[128] M. Dennin. "Statistics of bubble rearrangements in a slowly sheared two-dimensional foam." *Phys. Rev. E*, **70**, 041406 (2004).

[129] L. Isa, R. Besseling, A. N. Morozov, & W. C. K. Poon. "Velocity oscillations in microfluidic flows of concentrated colloidal suspensions." *Phys. Rev. Lett.*, **102**, 058302 (2009).

[130] B. Miller, C. O'Hern, & R. P. Behringer. "Stress fluctuations for continuously sheared granular materials." *Phys. Rev. Lett.*, **77**, 3110–3113 (1996).

[131] R. R. Hartley & R. P. Behringer. "Logarithmic rate dependence of force networks in sheared granular materials." *Nature*, **421**, 928–931 (2003).

[132] J. Lauridsen, M. Twardos, & M. Dennin. "Shear-induced stress relaxation in a two-dimensional wet foam." *Phys. Rev. Lett.*, **89**, 098303 (2002).

[133] E. Gardel, E. Sitaridou, K. Facto, E. Keene, K. Hattam, N. Easwar, & N. Menon. "Dynamical fluctuations in dense granular flows." *Physical and Engineering Sciences*, **367**, 5109–5121 (2009).

[134] D. Weaire & S. Hutzel. *The Physics of Foams* (Oxford University Press) (1999).

[135] A. Kabla & G. Debregeas. "Local stress relaxation and shear banding in a dry foam under shear." *Phys. Rev. Lett.*, **90**, 258303 (2003).

[136] H. Princen. "Rheology of foams and highly concentrated emulsions i. elastic properties and yield stress of a cylindrical model system." *J. Colloid Interf. Sci.*, **91**, 160–175 (1983).

[137] M. E. Cates, J. P. Wittmer, J. P. Bouchaud, & P. Claudin. "Jamming, force chains, and fragile matter." *Phys. Rev. Lett.*, **81**, 1841–1844 (1998).

[138] D. W. Howell, R. P. Behringer, & C. T. Veje. "Fluctuations in granular media." *Chaos: An Interdisciplinary Journal of Nonlinear Science*, **9**, 559–572 (1999).